UNIVERSIDAD AUTÓNOMA DE SAN LUIS POTOSÍ

CENTRO DE INVESTIGACIÓN Y ESTUDIOS DE POSGRADO

FACULTAD DE INGENIERÍA

ENERGY MANAGEMENT SYSTEM IN AN AC MICROGRID BASED ON PHOTOVOLTAIC INVERTERS

T H E S I S

SUBMITTED FOR THE DEGREE OF
Doctor in Electrical Engineering

MAJOR: POWER ELECTRONICS FOR ALTERNATIVE ENERGY SOURCES

P R E S E N T S:

M.ENG. AGUSTÍN TOBÍAS GONZÁLEZ

A D V I S O R:

DR. VÍCTOR MANUEL CÁRDENAS GALINDO

San Luis Potosí, S.L.P. Oct 2023

UASLP
Universidad Autónoma de San Luis Potosí

FACULTAD DE INGENIERÍA

18 de mayo de 2023

M.I. AGUSTÍN TOBÍAS GONZÁLEZ
P R E S E N T E.

En atención a su solicitud de Temario, presentada por el **Dr. Víctor Manuel Cárdenas Galindo,** Asesor de la Tesis que desarrollará Usted con el objeto de obtener el Grado de **Doctor en Ingeniería Eléctrica**, me es grato comunicarle que en la sesión del H. Consejo Técnico Consultivo celebrada el día 18 de mayo del presente año, fue aprobado el Temario propuesto:

TEMARIO:

"Sistema de Gestión de Energía en una Microrred de CA basada en Inversores Fotovoltaicos"

Introducción.
1. Modelado del sistema de una microrred de CA
2. Estrategias de control para inversores fotovoltaicos en una microrred y su implementación
3. Análisis y síntesis de la operación óptima de la microrred
4. Resultados de simulación para el sistema de microrred

Conclusiones
Apéndices
Referencias

"MODOS ET CUNCTARUM RERUM MENSURAS AUDEBO"

A T E N T A M E N T E

DR. EMILIO JORGE GONZÁLEZ GALVÁN
DIRECTOR

UNIVERSIDAD AUTÓNOMA DE SAN LUIS POTOSI
FACULTAD DE INGENIERIA
DIRECCION

Copia. Archivo.
*etn.

Agradecimientos

A mi madre Teresa, por su apoyo, amor y paciencia durante esta importante y larga etapa, también por siempre ser ejemplo de trabajo y perseverancia.

A mi hermana Lucero, por su apoyo y cariño incondicional.

A mi asesor, el Dr. Víctor Manuel Cárdenas Galindo, por haberme dado la oportunidad y confianza de trabajar con él en esta investigación, así como en otros proyectos muy enriquecedores para mi formación, por siempre compartir su tiempo y gran conocimiento, siendo un excelene guía en este camino del saber.

A la LEI. Ana Cecilia Rivera R., gracias por su disposición y amistad durante toda mi estancia en el laboratorio, así también en el desarrollo de esta investigación.

A mis revisores y tambien profesores de posgrado, el Dr. Ricardo Álvares, el Dr. Mario González y el Dr. Homero Miranda, por dar seguimiento a esta investigación y por su disponibilidad para resolver dudas y compratir su conocimiento.

Al Dr. Carlos Daniel García B., por el seguimiento y apoyo como revisor externo y la obtención de resultados en esta investigación.

A los profesores Josep M. Guerrero y Juan C. Vasquez, por su apoyo y atenciones durante mi estancia en la Facultad de Ingeniería y Ciencia en Aalborg, Dinamarca.

A mis amigos, Daniel, Fernando, Juan e Israel, gracias por su amistad, por compartir su conocimiento y brindar apoyo durante las distintas actividades de convivencia y como equipo de trabajo.

A mi amigo y compañero Manuel A. Barrios, por su amistad y apoyo en distintos proyectos del laboratorio, así como sus atenciones para la relización de mi estancia de investigación.

A mis amigos y compañeros del laboratorio, San José, Uriel, Ángel, Samuel, Yuniel, Rosa e Isaac, por hacer de la estancia en el laboratorio una experiencia agradable.

Al coordinador, el Dr. Miguel Lastras M., a los Doctores miembros del comité del PIE, equipo administrativo y personal del CIEP, así como de la Facultad de Ingeniería de la UASLP, por su amable atención en distintas etapas del desarrollo de esta investigación.

Al Consejo Nacional de Ciencia y Tecnología (CONACYT) por el apoyo económico brindado para desarrollar mis estudios de doctorado con la beca CVU-554496.

CONTENIDO

Apéndices

CONTENTS

List of Tables

List of Figures

List of Acronyms and Abbreviations

Acronym	Meaning in english	Meaning in spanish
AC	Alternating Current	Corriente alterna
AWG	American Wire Gauge	Calibre de Alambre Americano
ADSC	Asymptotic Distributed Secondary Control	Control Secundario Distribuido Asintótico
BTB	Back-to-Back converter structure	Estructura bidireccional de convertidor de electrónica de potencia
CAN-BUS	Controller Area Network Bus	Bus Controlados de Área
CCM	Current Control Method	Método de Control por Corriente
CMD	Sliding Mode Control	Control por modos deslizantes
CMV	Common-Mode Voltage	Tensión en modo común
CCPM	Circulating Current Phasor Model	Modelo Fasorial para Corrientes Circulantes
CCPPM	Circulating Current Power Phasor Model	Modelo fasorial para Potencia por Corrientes Circulantes
CDC	Conventional Droop Control	Estrategia *Droop control* convencional
CFE	Federal commission electricity	Comisión Federal de Electricidad
CKL	Current Kirchhoff Law	Ley de corrientes de Kirchhoff
DC	Direct Current	Corriente directa
DC/AC	Direct Current to Alternating Current.	Corriente Directa a Corriente Alterna.
DC/DC	Direct Current to Direct Current.	Corriente Directa a Corriente Directa.
LC	Linear Control	Control Lineal

Acronym	Meaning in english	Meaning in spanish
NLC	Non-Linear Control	Control No Lineal
DAISC	Distributed Average Integral Secondary Control	Control secundario distribuido integral promedio
DCG	Generalized Droop Control	Droop control generalizado
DG	Distributed Generation	Generación distribuida
DGU	Distributed Generation Unit	Unidad de generación distribuida
DLPF	Distributed Low-Pass Filter	Filtro Pasa Bajas Distribuido
ESS	Energy Storage System	Sistema de almacenamiento de energía
FB	Full Bridge	Puente completo
FCS-MPC	Finite Control Set Model Predictive Control.	Control predictivo basado en modelo finito
FLC	Fuzzy Logic Control	Control de Lógica Difusa
GM	Gradient Method	Método de gradiente
GSV	Virtual synchronous generator	Generador Síncrono Virtual
GWFBC	Generalized Washout filter based control	Control basado en filtro Washout Generalizado
IEA	International Energy Agency	Agencia internacional de energía
LBC	Low Bandwidth Communication Channel	Canal de comunicación de bajo ancho de banda
LCL	Inductive-capacitive-inductive filter	Filtro inductivo-capacitivo-inductivo
LP	Linear Programming	Programación lineal
M-Droop	Modified Droop Control	Estrategia *Droop control* modificada
MG	Microgrid	Microrred
MPP	Maximum Power Point	Punto de máxima potencia
MPPT	Maximum Power Point Tracking	Seguimiento de punto de máxima potencia
NE	Non Specified	No Especificado
NEC	National Electric Code	Código nacional eléctrico
NP	Non Specified	No especificado
OPS	Optimal Power Sharing	Distribución de potencia óptima
PCC	Point of Common Coupling	Punto de acoplamiento común
PDSC	Proposed Distributed Control	Control secundario distribuido propuesto
PF	Power factor	Factor de potencia

Acronym	Meaning in english	Meaning in spanish
PG&E	Pacific Gas and Electric Company	Compañía de gas y electricidad del Pacífico
PO_{max}	Maximum Overshoot Percentage	Sobrepaso máximo
PR	Proportional Resonant Controller	Controlador proporcional resonante
PSh	Power Sharing	Distribución de potencia
PSO	Particle Swarm Optimization	Optimización por enjambre de partículas
PV	Photovoltaic	Sistema fotovoltaico
PVPS	Photovoltaic Power System Program	Programa de integración de sistemas fotovoltaicos
RGISEN	General Rules of Interconnection to the National Electric System	Reglas Generales de Interconexión al Sistema Eléc trico Nacional
RE	Renewable Energy	Energía renovable
RES	Renewable Energy Systems	Sistemas de energía renovable
RVI	Resistive Virtual Impedance	Impedancia virtual resistiva
SCE	Southern California Edison	Compañía Edison del sur de California
SDG&E	San Diego Gas & Electric	Compañía San Diego gas y electricidad
SEPFC	Stability Enhanced P-f droop control	Control por Droop P-F mejorado
SG	Smart Grid	Red Inteligente
SPFB	Single-phase Full-bridge	Puente completo monofásico
SRF-PLL	synchronous reference frame phase-locked loop	Control de amarre de fase en marco síncrono
THD	Total Harmonic Distortion	Distorsión armónica total
VA	Volt-ampere	Volt-amper
VAr	Reactive Volt-ampere	Volt-ampers reactivos
VCM	Voltage control method	Control en modo tensión
VKL	Voltage Kirchhoff Law	Ley de tensiones de Kirchhoff
VM-DPC	Voltage Modulated Direct Power Control	Control directo de potencia por modulación de voltaje
VSC	Voltage Source Converter	Convertidor fuente de tensión
VSIPS	Voltage Source Inverter Parallel Operation System	Inversor fuente de tensión operando en paralelo
WFBC	Washout Filter Based Control	Control basado en filtro Washout

List of Variables and Symbols

Symbol	Meaning
$c_{1,2}$	Cognitive factors of the PSO method
C_{DC}	DC Filter capacitance
C_f	LCL Filter capacitance
C_p	Cost per unit generated energy
D_B	Duty cycle of the boost converter
Δf	Frequency Absolute Error
ΔP	Active power absolute error
ΔQ	Reactive power absolute error
ΔV	Voltage absolute error
f_{sw}	Switching frequency
F_i	Cost rate function
g	Electrical shunt conductance of distributed parameters
G_{best}	Global best value in the PSO method
γ	Propagation constant of the electrical line mathematical model
h_i	height of the line conductor
$h(P)$	Operating cost function
$i^{d,q}$	Electrical current signal in dq components
$i_{1,2}$	Instantaneous electrical currents of the LCL filter
i_B	Instantaneous electrical current of boost converter
i_{DC}	Instantaneous electrical current of DC bus
i_f	Instantaneous electrical current of the filter capacitor
i_g	Instantaneous electrical current
i_{inv}	Instantaneous electrical input current of the inverter
i_{LB}	Instantaneous electrical current of the boost inductance
i_{pv}	Instantaneous electrical currents of photovoltaic panel
$\mathbf{J}$	Interconnection elements matrix
K	Capital cost constant
k_p	Proportional gain of the PI controller
k_i	Integral gain of the PI controller
l	Power line length
L	Electrical inductance

Symbol	Meaning
L_B	Electrical line inductance of the boost structure
L_l	Electrical line inductance
$L_{1,2}$	Electrical inductance
λ	Lagrange multiplier
Λ	Penalty factor of the fitness function in the PSO method
m_B	Switching function of the boost converter
m_{inv}	Switching function of the photovoltaic inverter
μ_0	Conductor permeability
$\mathbf{M}$	Energy storage elements matrix
p_o	Instantaneous electrical grid power
P_i	Electrical active power of the *i-th* DGU
P_L	Electrical active power of the connected load
P_{max}	Maximum electrical active power limit
P_{min}	Minimum Electrical active power limit
p_{best}	Historical best value in the PSO method
Q_i	Electrical reactive power of the *i-th* DGU
$\mathbf{R}$	Damping elements matrix
r_i	Geometric mean radius
$r_{1,2}$	Social factors of the PSO method
R_{DC}	Low-frequency electrical resistance
R_f	Electrical parasitic resistance of the capacitor
R_l	Electrical line resistance
$R_{1,2}$	Electrical LCL filter resistances
S	Electrical apparent power
S_B	Power electronics switch of the boost converter
S_x	Power electronics switch of the inverters
S_{ix}	Slope for the piecewise approximation of the non-linear function
σ_c	Conductor conductivity
$\mathbf{T}$	$\alpha\beta$ to dq Transformation matrix
t_d	Time delay
T_{ss}	Settling time
θ_g	Phase angle of the AC mains voltage
$\theta_{\mu g}$	Phase angle of the microgrid voltage
$u^{d,q}$	Modulations functions in dq components
U_x	Output signal of the PI controllers
v_{DC}	Direct current voltage
$V_j(i)$	Particle velocity in the PSO method
$\mathbf{V_{dq}}$	Synchronous reference frame voltage vector in dq variables
$\mathbf{V_{RI}}$	Vector of the real and imaginary AC voltage components
v_{cf}	Instantaneous electrical voltage of the filter capacitor
v_g	Instantaneous electrical grid voltage

Symbol	Meaning
v_{pv}	Instantaneous electrical voltage of photovoltaic panel
v_{pwm}	Pulse-width modulation signal voltage
$v_{\mu g}$	Instantaneous electrical voltage of the microgrid
ω	Electrical angular frequency
$X_j(i)$	Particle location vector in the PSO method
y	Electrical shunt admittance of distributed parameters
z	Electrical series impedance of distributed parameters
Z_C	Electrical line characteristic impedance
Z_{HF}	High-frequency electrical impedance
Z_l	Electrical line impedance
Z_g	Electrical grid impedance

Abstract

Recently, Photovoltaic energy-based systems installed have been increasing along with the operation of microgrids. This makes distributed generation, due to weather changes, an intermittent way of supplying power to connected loads. Previously, technological advances and applications always considered the use of all available photovoltaic power, which allowed a large amount of electricity to be generated for injection into the AC mains. Hence, there was a lot of investment in this type of system to reduce the cost of purchasing electricity from the AC mains. However, this caused some problems to appear due to an excess of injected power compared to the demanded load, at a certain time of the day, in addition to the lack of control over the energy supplied to the system. Such problems involve frequency and voltage oscillations and deviations that lead to erroneous operations and blackout scenarios. In this sense, solutions to the main problems that must be taken into account to maintain the microgrid parameters within adequate values are achieved through control strategies that provide intelligent characteristics to the distributed generation units, and allow the system to compensate for voltage and frequency deviations, as well as to reduce power losses through adequate power sharing methods. To add the necessary power to distributed generation units, it is important to select a suitable power electronics structure that provides active and reactive power generation and control capabilities, allowing to perform different management tasks while taking into account other fundamental parameters such as high efficiency and adequate THD performance; unlike traditional power electronics inverters focused on photovoltaic generation, where the main features are to avoid reactive power circulation with the AC mains and to limit leakage currents.

As the microgrid systems are mainly clusters of distributed generation units operating in a determined array, an energy management system provides the microgrid with the capability to determine the amount and conditions of the power injected from the distributed generation units to the connected load as well as the exchanged power with the AC mains, while takes into account the proper constraints of each established scenario and objectives in the system operation. Due to the variability of energy in the photovoltaic systems, the optimal operation of the microgrid is essential to enhance the system's performance. In this sense a suitable energy management system can be designed in a hierarchical control structure to provide such capabilities to the microgrid. It can be in a centralized or a decentralized array according to the objectives and priorities of the system, considering the advantages and drawbacks of each one, where to obtain a global optimal solution, centralized arrays are a best choice. In addition, these systems must deal with unexpected sudden conditions as blackout scenarios, which forces the system to start-up with certain considerations if the power stage and the control strategy is capable to handle this problem. From the above a suitable black-start sequence must be defined to allow the system to return to the initial steady-state conditions.

In this thesis some optimization methods are analyzed and employed with the local controllers in a Hierarchical Control Structure to optimally distribute the power delivered by distributed generation units based on photovoltaic systems, which allows obtaining the minimal cost production together with the control strategies developed and experimentally implemented at the primary level, and the black-start procedure for microgrid performance in simulation is obtained. As part of the validation methods, the models used in the simulation results consider the entire system dynamics to show the detailed response with the operation scenarios.

Based on the above, the content of this document includes an Introduction chapter, which describes the state of the art of the main considerations of photovoltaic-based microgrid systems facing high penetration levels, as well as the relevant standards related to the integration and operation of photovoltaic systems. Chapter 1 contains the system definition and its mathematical modeling considerations and validations to design appropriate control strategies. Chapter 2 depicts the design and implementation of the control strategies at the primary control level, where the active and reactive power capabilities to the grid-feedings and voltage regulation to the grid-forming are proven. Chapter 3 analyzes optimization methods for the third control level, allowing the optimal power sharing scenario focused on economic operation. Chapter 4 contains the simulation results for the entire microgrid system, where the optimal operation in different scenarios is tested, also considering reactive power compensation capabilities, after that dynamical performance and black-start sequence are validated. Finally, the conclusions and contributions of this work are drawn as well as the considered future work for this research.

Introduction

There is a great motivation due to the use of Renewable Energy Sources (RES) for electric energy generation, because of several advantages over fossil fuels, mainly related to environmental aspects. It is estimated in 2021, 25 % of the total greenhouse gas emissions came from electricity production in the US [1]. The use of Distributed Generation Systems (DGS) based on Photovoltaic systems (PV) has increased in a relatively short time due to its competitive operation and maintenance cost compared with others RES in the electricity generation market. According to the International Renewable Energy Agency (IRENA), in 2022 the global installed PV capacity reached 1,046,614 MW, where the annual installed capacity in 2022 was 192 GW. Also the electricity production of wind and solar PV are on course to displace an estimated 230 terawatt-hours (TWh) of fossil fuel generation over the 2021-2023 period [2, 3].

The exponential growth observed in the installed PV capacity entails considerable challenges regarding energy management issues, due to the high penetration levels given by the interconnection of large amounts of DG systems and the AC mains. The main characteristic of installed PV systems is its variable size and scalability can be in order of hundreds of watts until hundreds of MW, when they are connected to low and medium voltage systems in comparison with another RES such as wind turbines [4]. The interests currently focused on the uneven distribution, have had these systems in low voltage levels, as much as for the utilities as for the final consumers that have adopted residential PV systems along the low voltage power system. The final consumers also have started contributing an important amount of distributed energy in small electrical generation systems. In general terms, the interconnected small scale PV systems do not include grid supporting functions, which comes to complex control issues due to each subsystems contributing all available energy to AC mains. The modification of politics and standards in regions where there is a large amount of generated energy by this kind of systems have become imperative, and in some cases, it has been overtaken. From the aforementioned situation, it must be considered that the main solutions to energy management and distribution are carried out by DG systems throughout the control systems in the power electronics converters that allow the AC mains interconnection, hence there are always challenges to make it possible with the inclusion of new features in terms of interoperability among these systems.

A decisive factor in PV usage, in addition to the well studied environmental issues, it is also the economic impact for the use and long-term return on investment associated with technical factors (reliability, useful life and efficiency), technological factors (semiconductors, control systems and communications) and economic factors (market competition, costs reduction and scalability), which makes important to consider its evolution along the time.

Global Solar perspective

According to International Renewable Energy Agency data, as for installed capacity of renewable energies, at the end of 2022 is 3,372 GW, where 1,053 GW comes from installed capacity in PV, as it is shown in Figure 1. In addition, in 2022 the power capacity in renewables increased by 295 GW (+9.6%), where solar power capacity have increased 192 GW (+22%), followed by wind energy with 75 GW (+9%), as it is illustrated in Fig. 2 [3].

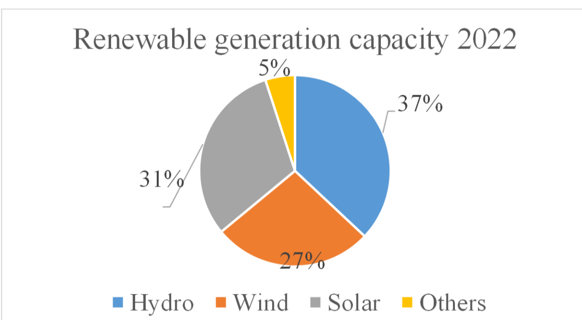

Figure 1. Installed capacity.

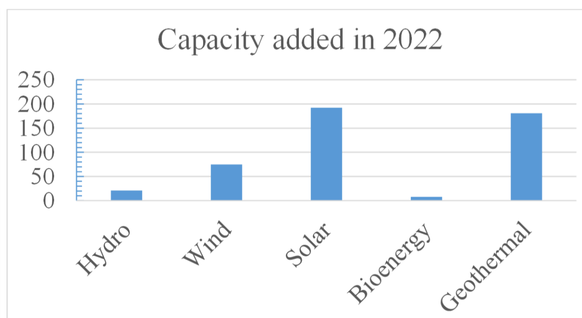

Figure 2. Renewable power capacity growth (GW).

Therefore, according to the 2022 Renewable Energy Statistics Report of IRENA, in 2020 renewable electricity generation reached 7,468 TWh, where 844 TWh correspond to solar energy with the main contribution made by Asia, with an increase of 236 TWh (42%), followed by Europa (19%), north America (18%), South America (11%), Eurasia (5%), Africa (2%), Oceania (1%). It is also important to point out the increase in renewable electricity generation observed from 2019 to 2020 was 22% and 12% for solar and wind generation respectively [3, 5].

Regarding the regional panorama, Mexico has a daily average solar irradiation stands at

5.5 kWh/m^2 [6]. The installed capacity in renewable energies was 31.683 GW in Mexico in 2022, where the installed capacity in PV was 9.009 GW. The installed capacity PV evolution from 2019 to 2022 is shown in Fig. 3 where it has been increased by 4.284 GW in this period [6].

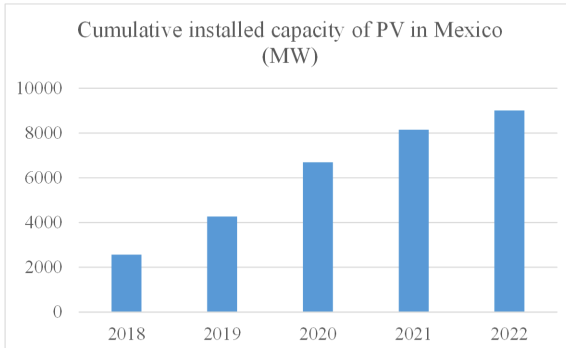

Figure 3. PV installed capacity from 2019 to 2022 in Mexico.

It is important to mention that the solar resource forecast indicates these type of systems will grow and work interconnected to AC mains, and depending on the region it could lead to high penetration scenario.

1. Standards and regulations related to photovoltaic energy systems

The increase in the use of interconnected PV systems brings with it technical issues, voltage profiles variation, over-generation cases, harmonic contamination and so on, as a result of the high penetration levels emerged in the last decades. Due to the aforementioned situation, it is necessary to consider a reliable operation for the end user and the equipment and devices connected; it is achieved through standards and regulation regarding to the regulated operation of interconnected PV systems. These standards must be one step ahead in terms of the great evolution of these technologies and they are studied and modified by teams and groups of experts in photovoltaic sector.

The most representative standards concerning the installation of photovoltaic systems interconnected to the AC mains are mentioned below.

IEEE 1547- 2018 - Standard for Interconnection and Interoperability of Distributed Energy Resources with Associated Electric Power Systems Interfaces

The IEEE std 1547-2018's is focused on interoperability aspects [7]. Among other topics it can be remarked the following:

- Contains the definition of technical specifications to be applied throughout the world by several facilities and institutions.
- Is focused on the technical requirements for the interconnection of Distributed Energy Resources (DER) technologies.
- It ranges from 10 MVA and larger Distributed Energy Sources.

IEEE 929-2000 - Recommended Practice for Utility Interface of Photovoltaic Systems

This document contains guidance related to equipment and functions, and contemplates the operation of Photovoltaic systems (PV) in parallel operation with AC mains [8].

- This includes personnel safety, protection for the equipment, AC mains operation and power quality.
- Address issues such as islanded operation of PV systems, as well as anti-islanding procedures.
- Comprises generation units under 10 kVA.

IEEE 519-2022 - Standard for Harmonic Control in Electric Power Systems

This standard address AC mains operation including linear and non-linear loads. Establish the harmonic contents limits of current and voltage of the system [9].

- It specifies the common sources of harmonics in power systems, they can be power electronics converters, as well as, power inverters in distributed generation.
- It applies at the PCC between the DER and the AC mains.

UL 1741 Standard

This standard applies to power inverters, converters, controllers and interconnection equipment to be used as DG sources [10].

- It contemplates the aspects covered by IEEE 1547 STD and IEEE 1547.1 STD.
- This standard also covers security aspects, and it is more specific regarding building and operation ranges.
- The IEEE 929 standard contemplates to cover the tests considered in UL 1741 standard.

Rule 21 Interconnection

The Electric Rule 21 is a tariff approved by Public Utilities Commission in the State of California (CPUC). This mainly describes details such as interconnection, operation and metering requirements for generation facilities to be connected to the AC mains utilities such as Pacific Gas and Electric Company, San Diego Gas & Electric and Southern California Edison (PG&E, SDG&E y SCE), where CPUC has jurisdiction [11].

NFPA 70, National Electrical Code

The National Electrical Code (NEC), known as NFPA 70, establishes the rules of electrical design contemplating safety issues regarding personnel, equipment and electrical failures, including those related to PV systems [12].

Standards in Mexico

There are some agreements regarding to DG systems and their interconnection with AC mains in Mexico:

- Agreement issuing the Interconnection Manual for Generation Plants with a Capacity under 0.5 MW. This agreement is an interconnection standard issued by SENER in 2016. This cover overcurrent protection aspects, voltage and frequency disturbances, anti-islanding operation, reverse active power and out-of-synchronism.
- There is no interoperability standard and the certified procedures and tests are detailed in normative documents such as [13]:

- Specification for the Interconnection to the Low Voltage Electric Network of PV systems with capacity up to 30 kW (CFE G0100-04-2008).
- General Rules of Interconnection to the National Electric System 2012 (RGISEN by its acronym in Spanish).
- Tests on Low Voltage Inverters with Capacity up to 30 kW for Interconnected Photovoltaic Systems (CFE U0000-30-2015).

Taking into account that there are modifications in the standards, rules and normative due to the necessity of adapting the increase of DG and PV systems interconnected to AC mains, the final user must apply the rules and restrictions established, where new advanced functionalities can be added to the power electronics converters to accomplish the required tasks, and solving the problems associated with high penetration of PV systems in AC mains.

1.1. Grid-connected PV Inverters topologies

The most common PV inverters topologies mainly used by its good performance regarding to high efficiency, lower cost, size and weight, are the transformerless structures. These type of PV inverters have some problems such as leakage currents due to parasitic capacitance, electromagnetic emissions and in some cases high-switching losses due to the number of power electronics switches, as well as the considerations needed to operate without galvanic isolation [14]. Considering the corresponding standards regarding to interconnected PV-inverters, it is necessary to make a review about which topologies are capable to accomplish the pertaining operation requirements in an Smart Grid (SG). According to [15], a SG can be defined as an end-to-end cyber-enabled electric power system from fuel source to generation, transmission, distribution, and end use, that enables RES integration, allow two-way power and information flows, enables effective demand management and customer choice, self-healing facing disturbances as well as resilient operation against physical and cyber-attacks. In this regard, smart microgrids are also a solution to take advantage of RES in smart cities, where the large-scale utilization of these local energy networks is deployed to increase the reliability of the electrical system [16]. Therefore, the PV inverters seen from the point of view of the microgrid, must provide ancillary services and grid support features, where theses considerations were previously only intended for conventional generation plants. One of these features is the Low-Voltage Ride-Through Capability (LVRT) [17]. There are some most commonly used transformerless topologies in single-phase PV inverters; they have certain advantages and disadvantages and their scheme is shown in Figure 4 [18, 19].

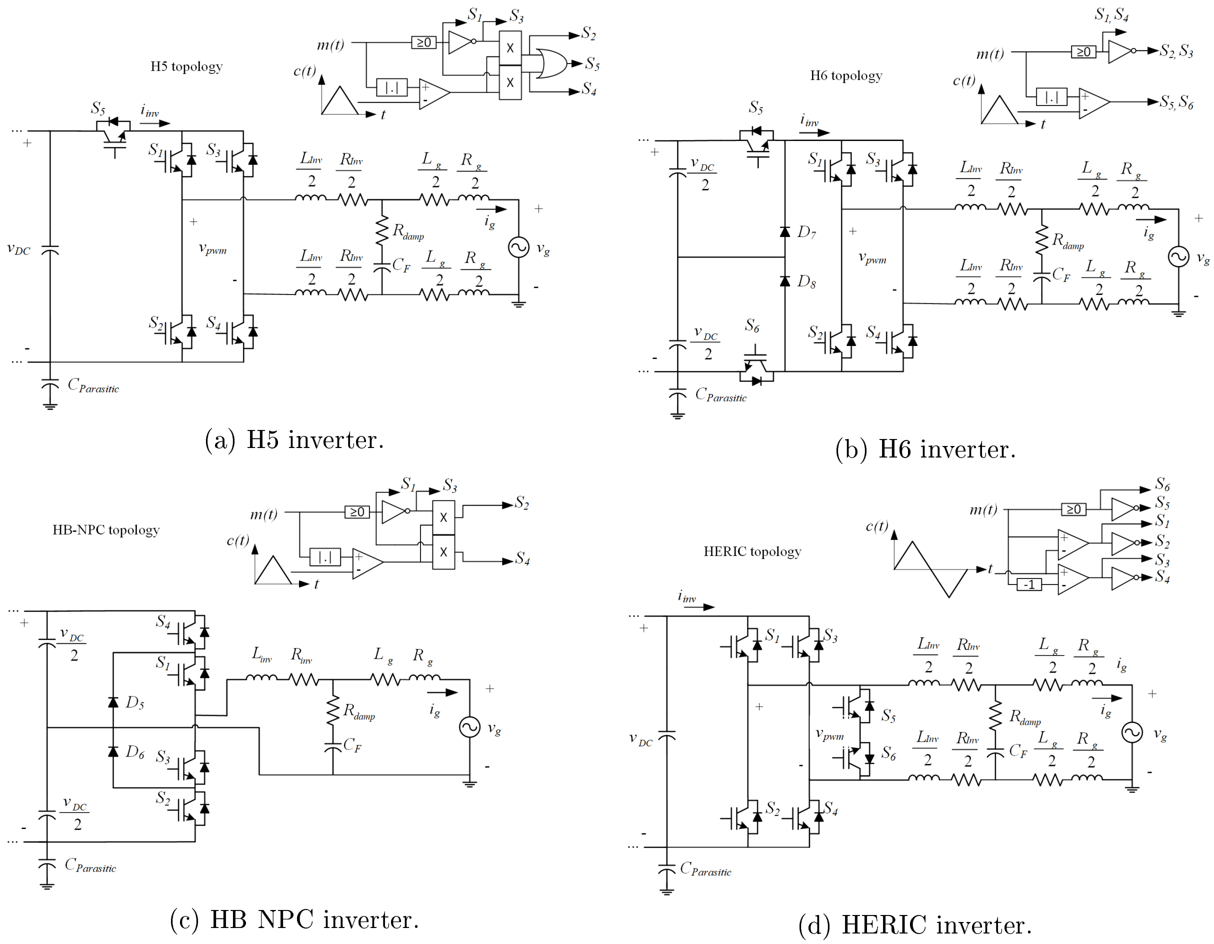

(a) H5 inverter.

(b) H6 inverter.

(c) HB NPC inverter.

(d) HERIC inverter.

Figure 4. Transformerless DC/AC PV converters topologies.

H5 inverter

This type of inverter was patented by SMA in 2005 and its shown in Fig. 4 (a). Among its main features it stands out that S_5 and S_4 (S_2) are switched at high frequency, while S_1 (S_3) are switched at grid frequency; there are two possible zero voltage states, with $S_5 = OFF$ and S_1 (S_3) $= ON$. Another feature is that S_5 prevents reactive power exchange between L_{inv} and the input capacitor leading to efficiency up to 98% [19].

H6 inverter

The Fig.4 (b) shows the H6 inverter structure. The main features of this converter are its two DC bypass switches S_5 and S_6 and this was developed by *Ingeteam*. It is possible to observe that this converter is made from a common H-bridge and two extra switches in the DC-link and two extra clamp diodes, where the zero voltage state is grounded.

HB-NPC inverter

The half-bridge neutral point clamped converter is shown in Fig. 4 (c); this topology is not full-bridge based, and its main feature is the zero voltage state when the medium point is grounded, where S_1 and (S_4) are high-frequency switched and S_2 and (S_3) are grid-frequency switched.

HERIC inverter

The Highly Efficient and Reliable Inverter Concept (HERIC) is patented by *Sunways* and it is derived from H-bridge topologies as shown in Fig.4 (d). This topology has a bypass leg in the AC side and it is composed of two switches in back-to-back mode which allow to decouple the AC side during free-wheeling states. Also it allows to have two zero voltage states with $S_5 = ON$ and $S_6 = ON$.

H8 inverter

The H8 topology is another type of non-isolated interconnected PV inverter; this consists of an H-bridge with four additional switches at the DC input and it is shown in Fig. 5, [17, 20].

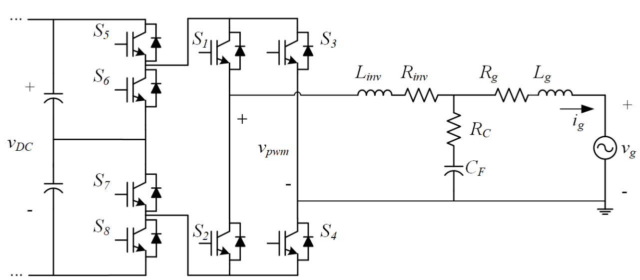

Figure 5. H8 inverter.

According to the necessity to improve the features that allow to give support from the PV inverters to AC mains, as well as the restrictions imposed by the standards mentioned before, it is necessary to consider the topologies that are capable to accomplish the requirements for the PV systems when they are working in an interconnected or an islanded system as a microgrid. Table 3 shows the performance comparison among these topologies, where it is possible to observe there are topologies focused in avoiding or decreasing leakage current through the parasitic capacitance by using modulation strategies, and it is also related with a constant and varying Common-Mode Voltage (CMV) and the number of levels. Nevertheless, some topologies do not allow the reactive power exchange and with this, they are not capable to accomplish with LVRT functions to give support to AC mains [17].

Table 3. Performance comparison among transformerless PV inverter topologies.

PV inverter	H-bipolar	H-unipolar	H5	H6	HERIC	H8
Constant CMV	2 lev.	-	2 lev.	2 & 3 lev.	2 & 3 lev.	3 lev.
Varying CMV	-	3 lev.	3 lev.	3 & 5 lev.	-	5
Switches/ diodes	4/0	4/0	5/0	6/2	6/0	8/0
LVRT	✓	✓	X	X	X	✓
THD_{Vpwm} (PF=1)	120.89 %	64.24 %	57.24 %	33.52 % (5 lev.)	57.55%	25.35 % (5 lev.)
THD_{Vpwm} (PF<1)	120.88 %	64.24 %	58.74 %	38.32 % (5 lev.)	59.3 %	25.35% (5 lev.)

1.2. Autonomous functions of advanced PV inverters and technical aspects

The interconnection of PV-based Distributed Generation Units (DGU) with AC mains leads to local scenarios where the active power supplied by the PV systems exceeds the power demanded by the load connected, hence it provides a backup to the power system, as a result there is a low amount of power supplied from conventional sources. As a matter of fact, there are some regions in the world where the use of RES assists with the problems of this zone, as it can be observed according to [12], although distribution losses are relatively neglected (around 5.7%), in the south of California these losses exceeded 10% during peak hours, hence when there are DGU near to the local loads, the transmission losses are reduced. As it is mentioned in the global perspective, the large amount of interconnected PV systems has a positive forecast; however, this increase represents a problem attempting to be regulated through international codes and defined standards, due to the variable characteristic of the RES. In particular for PV systems, there is a high generation level during daylight hours and there is also a lower active power demanded by the connected load; on the other hand, there is a low capability to contribute with the energy demanded after sunset. This above situation is illustrated in the demand curve of the independent system of California State (Fig.6), where zone a) represents the first hours of the day, zone b) are the mid-day hours and there is lower predictability of generation from renewable energy based DGUs, in particular PV systems, which causes reduction in conventional generation plants and this lead to overgeneration risk. Finally zone c) indicates the last hours of solar irradiation, where the conventional generation plants experience large slopes of power generated due to the reduction of PV generation and the increase of load demanded; this is known as *Duck-curve* [21, 22].

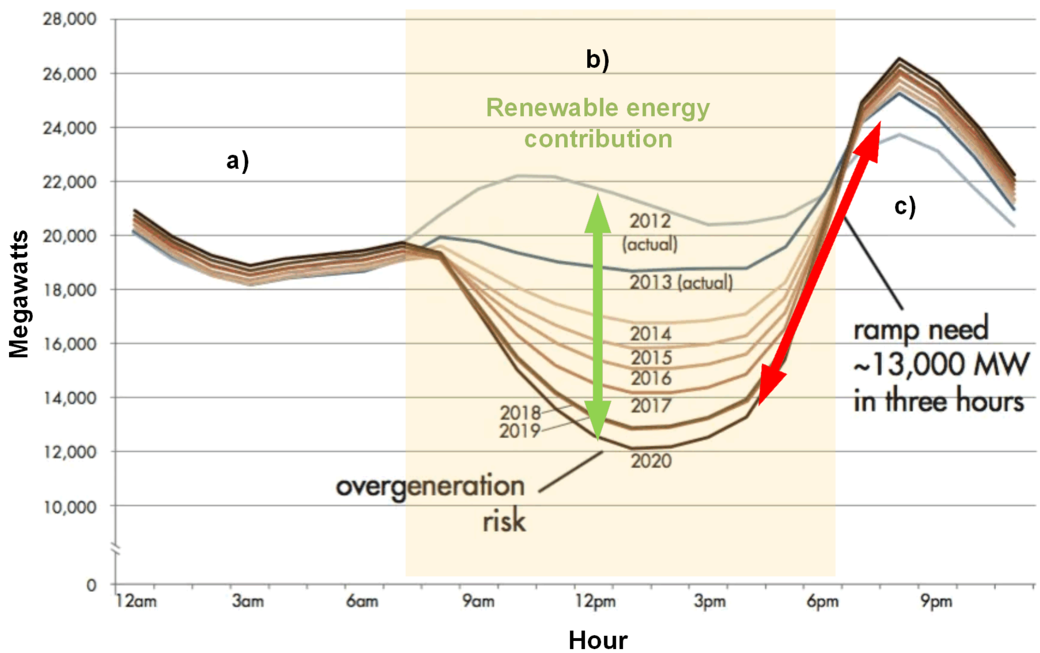

Figure 6. Demand curve in the State of California *Duck-curve*.

Derived from the above, it is necessary to consider some technical issues that are mentioned below.

Frequency oscillations

The frequency in the electrical system depends on the active power balance between the source and the load connected. There is very sensitive electrical equipment to the frequency variations, therefore the regulations regarding electrical generation allow to operate in a limited variation range of frequency, which in the conventional manner is regulated by the inertia of the AC mains. Also, it is possible to provide to the PV systems with Maximum Power Point Tracking Algorithms (MPPT) and take advantage of the whole energy that comes from solar irradiation, but in high penetration levels scenarios this operation does not allow well performed frequency regulation tasks [23].

Overvoltage at PCC

There are overvoltage risk in scenarios where there is reverse power flow caused by high penetration levels of PV systems and low power demanded by the load. Conventionally, this issue is solved throughout capacitor banks and tap changers transformers but also these solutions have slow dynamics, hence they are not able to compensate the transitory produced by photovoltaic systems [24, 25].

Harmonic contamination

The harmonic contamination is another issue related to high penetration levels, which has been mitigated through the restrictions imposed by the standards and also the well selected topologies and control strategies in the power electronics based DGUs [26].

1.3. Autonomous functions in advanced PV inverters

The varying characteristics of RES like PV systems makes the interoperability one of the most important aspects to consider in high penetration levels scenarios [12, 22, 27]. Therefore the power electronics converters working with PV systems are not only thought to obtain the whole active power available from solar irradiation but also they must accomplish regulation tasks considering the restrictions [23, 28]. Hence the inverter must perform focused tasks to provide support to AC mains [4, 29–31]. The advanced functions performed by PV systems leading to a reliable interoperability among DGUs, are focused to provide voltage and frequency support to AC mains, as well as protection against disturbances and faults. The most representative aspects are:

- Voltage regulation
  This is achieved through the control strategy of the PV inverters, in order to maintain the AC voltage levels between allowable limits, and also to compensate reactive power necessities and power factor correction [32–34].

- Frequency regulation
  The frequency ranges in which electrical systems are allowed to operate are commonly very limited, hence frequency regulation is an important feature to consider among the advanced functionalities in PV inverters. This function is taken into account through *frequency-watt* control used in overfrequency scenarios [28].

2. AC microgrids structure and control strategies

PV systems working as DGUs, together with one or more loads connected can lead to work as a separated electrical grid, independently whether it is connected or not with AC mains. Considering the rules and standards regarding grid-connected DGUs, the concept of Microgrid (MG) is defined as a set of DGUs, loads and energy storage systems that can work connected or in island mode with AC mains [35, 36]. The MG can be classified according to many criteria, one of them is considering if they work in DC called Direct Current Microgrid (DCMG), if they work in AC can be called Alternating Current Microgrid (ACMG) and hybrid called ACDCMG [37]. In general terms, the basic architecture includes the distribution system, DGUs, Energy Storage Systems (ESS) and the control system with or without communications [38]; ACMG also can be classified by the type of bus that DGUs share among them, they can be radial bus or ring bus MG [39]. Fig. 7 illustrates an ACMG in radial array, where typically this MG may contain different DGUs like wind turbine and PV systems, AC and DC loads, as well as electric vehicles and ESS.

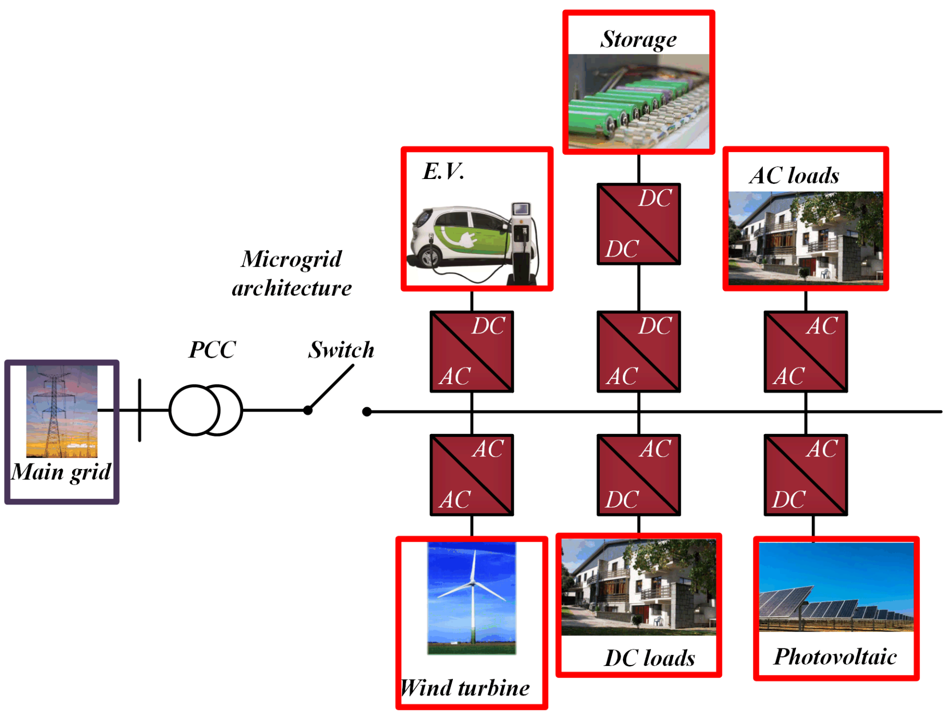

Figure 7. AC Microgrid architecture.

From the above it is necessary to consider the control task the DGUs must accomplish to make the MG work within the restrictions imposed. Therefore depending on these control tasks and according to the currently scenario, the power electronics converters in the PV systems can operate as grid-feeding, grid supporting and grid-forming converters, what makes possible to maintain the MG working and giving support to provide ancillary services to the whole system, this leads to a more reliable, controllable and well performed MG [40].

2.1. Control strategies in ACMG

A well selected control strategy is essential to operate the DGUs in a MG, due to the stochastic behavior of the renewable energies. This makes possible supply the active power needed, as well as minimizing the power consumption, cost of energy and giving the capability to make a smooth transition during the interconnection of the DGUs and AC mains even though sudden disconnections [37, 41].

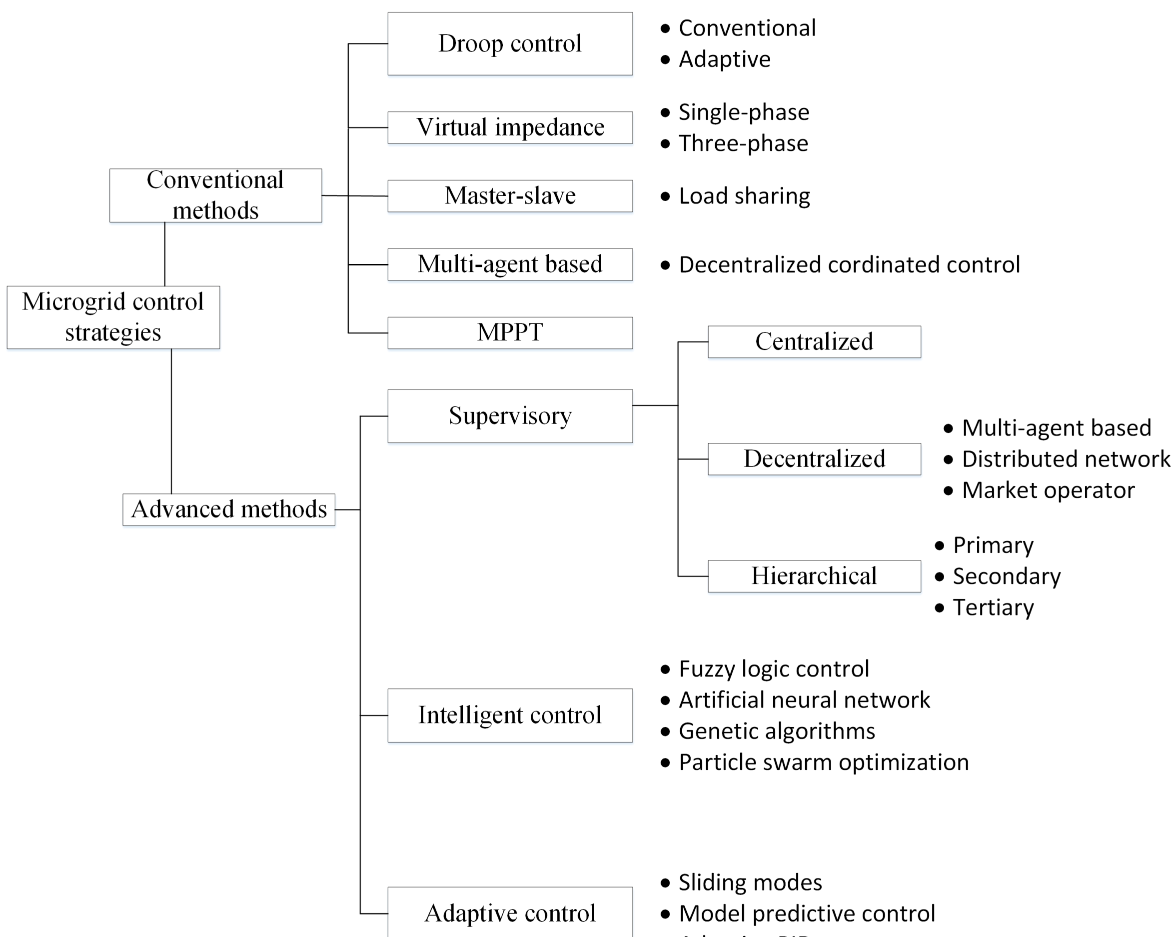

Figure 8. Classification of the MG control strategies.

From the classification above, it can be pointed out that the whole system operation needs a mixed of the control strategies to assign different tasks depending on the control stage and the role of the DGUs within the MG. Also, it is important to consider the performance evolution the MG have had to delimit the open problems.

3. Microgrid performance achievements

There are many aspects and parameters involved when a whole MG system is working to maintain features like the flexibility, reliability and accessibility, therefore various MG structures have been well studied as well as the control strategies used in high penetration levels of PV systems scenarios [42]. The research regarding MG applications and the technological evolution has been increasing to satisfy the necessities of the end user of the electricity as long as the restrictions and considerations imposed by the standards are accomplished, hence this bibliographical revision considers the improvement of the performance and capabilities of the existent solutions by proposing a PV-based system working with a hierarchical control structure to assess the mains issues in MG applications taking into account the MG structure, energy available from DGUs and connected loads. The tables 4 to 9 contain the details found in the reviewed references according to the simulation and experimental results that they present, where the performance parameters and the type of control strategies used in PV inverters are reported; this review is taken from 2012 to 2022. The references analyzed show different variants and combinations of performance parameters in the results. From the above, it is possible to observe graphically the trend in improving these results according to the control strategies, as it can be observed in the radar chart of the Fig. 9, where this contains the parameters of the corresponding steady state operation of the MG system considered in each research work; in this case it is not desirable a high value in such deviations, where ΔV is the voltage deviation, ΔP is the active power deviation, ΔQ is the reactive power deviation, PF is the power factor, THD_V is the total harmonic distortion of the voltage and THD_I total harmonic distortion of the current. As a consequence, the corresponding polygon of each reference has better performance features if its values are close to the origin of the graph, in exception of the power factor. It can be pointed out owing to the references report null value for some parameters, they have a zero value in the graph to form a closed polygon, hence it is not taken into account in the assessment to be compared.

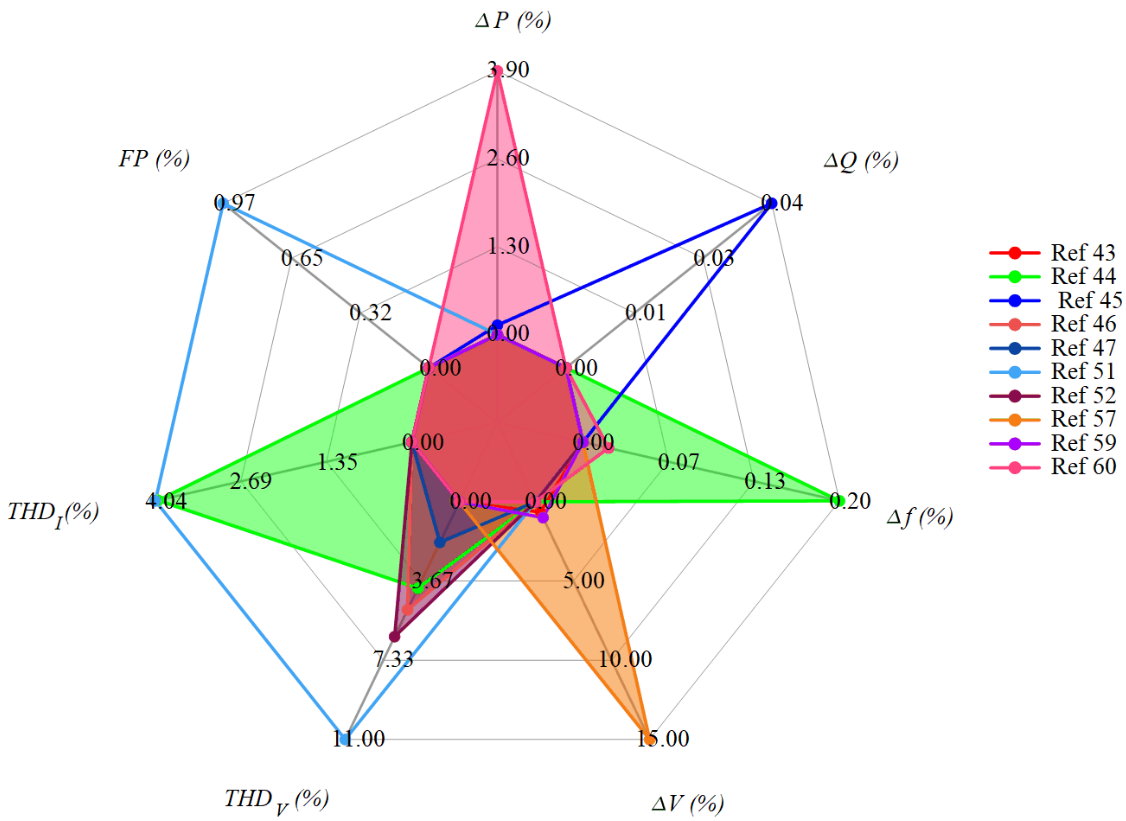

Figure 9. Performance parameters in steady state conditions.

From the above, the references with better performance in steady state conditions are [43], [44], [45], and [46] and their values can be corroborated in the corresponding Tables. It can be pointed out that it is not always possible to improve all the analyzed parameters at the same scenario and there is a compromise when the work is focused in one of them in the performance for the entire system operation.

The radar chart of the Figure 10 contains the performance parameters of the transient response for the results reported in each reference, they are the overshoot percentage $PO(\%)$ and settling time T_{ss} for each one of the variables associated. The references [43] and [47] have their results closer to the origin, it indicates the best results in performance.

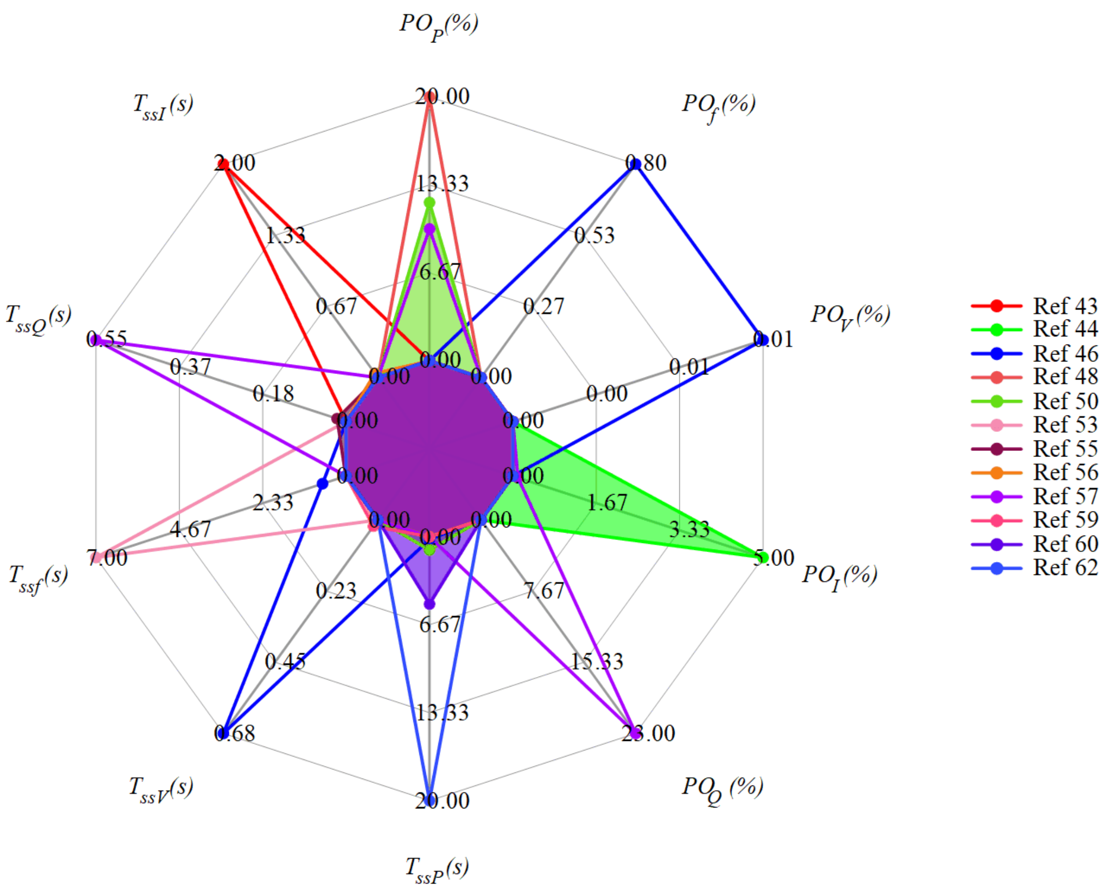

Figure 10. Performance parameters in transient state conditions.

The radar chart of the Figure 11 contains the MG design parameters considered in each research work. It can be observed in this case the parameters of the polygon with points closer to the origin have more outstanding features, they can be the number of DGUs, the power capacity and the switching frequency used. The parameter COM indicates the use of communications where the value of 1 implies there is no communication used in the system and 0 implies there is a communication system considered. In this case the references with more outstanding parameters are [43], [48] and [49].

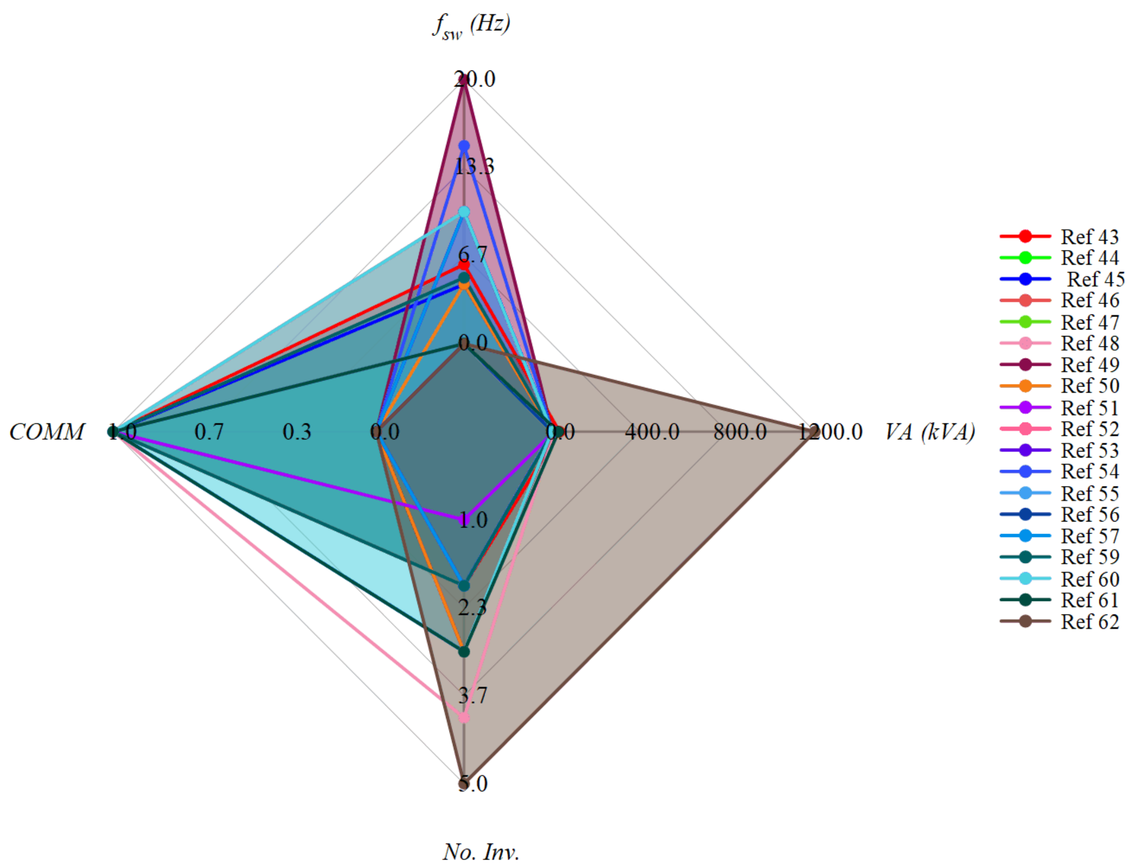

Figure 11. Design parameters of the MG.

Considering the above, the results obtained consider an MG in operation with a hierarchical control structure, highlighting the obtained performance in the parameters, considering the advantages of using certain control strategies and improving parameters where they have a disadvantage, as well as considering the restrictions that must be accomplished imposed by the standards.

Table 4. Bibliographical analysis.

Ref.	Year	Cit.	Journal	VA experimental	VA simulation	Φ	η	f_g/f_{sw}	Topology	Control strategy	Linear control /Non-linear c.
[50]	2012	266	IEEE TPE	3X0.3 kVA	3X1.2 KVA	3X208 VLL/ 3X104 VLL EXP.	NS	60 Hz / 4.5 kHz	FB	Hier. 2 Lev.	Linear control
[51]	2012	79	IEEE TPE	10 kVA	Not included	3X230 V	NS	50 Hz / NS	FB	1 Lev.	Lin. Control
[43]	2012	64	IEEE TPE	2X 35 kVA	Not included	3X380 V	NS	50 Hz / 6kHz	FB	Hier. 3 Lev.	Lin. Control
[52]	2013	281	IEEE TPE	GD1=60 W + 80 VAR, GD2=60 W + 80 VAR	NS	1X60 Vrms	NS	60 Hz / 12 kHz	FB	Hier. 2 Lev.	Lin. Control
[53]	2014	512	IEEE TPE	2X2.2 kW	Not included	3X311 VLL	NS	50 Hz / 10 kHz	FB	Hier. 2 Lev.	Lin. Control
[47]	2018	10	IEEE TSG	2X1 kw	1° 2x2.1 kw, 2° 3x750 VAR	3X110 V;3X80 V	NS	60 Hz / NS	FB	Hier. 2 Lev.	Lin. Control
[44]	2018	8	Applied Energy	0.6 y 0.4 kW	10 kW(6 y 4) MR	3x230 V/3X110 exp	NS	50 Hz / NS	FB	Coord.	Non-linear
[54]	2018	8	IEEE TSG	2X2 kW	3X1500 W	3X110; 3X110 V	NS	60 Hz / 15 kHz	FB	Hier. 2 Lev.	Lin. Control
[45]	2018	8	Electrical Power and Energy Systems	DG1-3=1.8 kw; 1.2 kVAR	DG1-3=6 kVA, DG4=3 kVA	3X120 V	NS	50 Hz / 4.5 kHz	FB	Hier. 2 Lev.	Lin. Control

Table 5. Bibliographical analysis.

Ref	Year	Citat.	Journal	VA experimental	VA simulation	Φ	η	f_g/f_{sw}	Topology	control Strategy	Linear control /Non-linear c.
[55]	2018	8	IEEE-APEC	2X18 kW Semikron(0.9 kW-0.8 kVAr c/u)	NI	3X140 V	NS	50 Hz / NS	FB	Hier. 2 Lev.	MPC
[46]	2018	6	IEEE TSG	Vdc=15 V (P=NS)	3X17 kW	3X325 V	NS	50 Hz / 10 kHz	FB	Hier.2 Lev.	Lin. Control
[49]	2018	5	IEEE TPE	3X3 kVA	2X3 kVA VSI	1X110 V	NS	50 Hz /20 kHz	FB	Hier.2 Lev.	Lin. Control
[56]	2018	4	IEEE TPE	2X2.5 kW	2X5 kW	3X230 VLL	NS	50 Hz / NS	3N-NPC	Hier.2 Lev.	Lin. Control
[57]	2018	4	IEEE TSG	2X3 kVA	2X3 kVA	3X110 V\ 450 V_{DC}	NS	50 Hz / 10 kHz	FB	Hier.2 Lev.	Lin. Control
[58]	2019	7	IEEE TSG	HIL	3X10 kW	3X380 V_{LL}	NS	50 Hz /	FB	Hier.2 Lev.	Lin. Control
[59]	2019	4	IEEE TPE	2X5 kW	2X3 kW 0.4 kVAR	3x110 V	NS	50 Hz / 5 kHz	FB	Hier.2 Lev.	Lin. Control
[60]	2019	3	IEEE TIE	3X910 W	NI	3X110 V	NS	60Hz / 10 kHz	F.B.	Hier. 2 Lev.	Lin. Control
[48]	2019	4	IEEE TPE	DGU1-4= 10 kW	10 kW	3X200 V	NS	50 Hz/ 10 kHz	FB	Hier.2 Lev.	Lin. Control
[61]	2021	4	IEEE Access	NS	3X30 kW	1X110 V	NS	60 Hz/NS	FB	Hier. 3 Lev.	NS
[62]	2022	7	IEEE JESTPE	NS	4X200 & 1X400 kVA	3-ph	NS	60 Hz/NS	FB	Hier. 2 Lev.	Lin. Control

Table 6. Bibliographical analysis.

Ref	Cont. Strategy	MG Struc.	Red model	VA Experimental/Simulation	Perform. Parameters	COMM	Connected/Non Connected	CPLTF
[50]	1° CDC switched with a compensation loop in Q	Rad.	Z_l	0.54 kW, 0.28 kVAR / 3.52 kW, 1.4 kVAR	SIM & EXP T_ssP = 1 s after compensation . PO_P = 12%. There are no PO% in current.	LBW COMM	Islanded	DSP
[51]	Adaptive strategy	Rad.	RL in one inverter	i=24 A; THD_v=11% & 20 % of unbalance	Stable PLL with Δf = 10%, THDv=11%, de 20% of unbalance. THD_iimproved from 7% to 0.8 %, FP from 0.9 to 0.98, THD_{ig} from 8.47 % to 4.04 %, FP 0.88 to 0.97.	without COMM	grid-connected	DSP
[43]	1°-DQ+ Droop 2°-Voltage compensation 3°-Synchronization	Rad.	Z_l	37 kW linear, 15 kVA NL	lower inrush current, Tss=2 s . ΔV= 2.5 V	without COMM	island mode/ modular characteristics	DSP
[52]	1° modified Alpha-Beta + Virtual Imp. 2°Centralized	Rad.	Z_g and Zh for harmonics.	PQ1 = 60 W + 40 VAR, PQ2 = 60 W + 40 VAR and rectifier diode.	P y Q distribution, THD_{Vpcc} = 6.24 % NL Load	LBW COMM	island mode	NS
[53]	1° DQ 2° C. Sec. Distributed	Rad.	Z_l	RLC+ Diode: NL	System capable to power sharing P & Q. $Tssf$=7 s. It has robustness with t_d and data losing	LBW COMM	Island mode	dSpace
[47]	1° DQ 2°Droop-mod	Rad.	RL in Z_l	100 VAR NL/1.8 kVAR NL	THD_v=2.88 to 1.88%/well performed with different Z_{alim}. h_5 and h_7 are reduced. Method effectiveness with load changes	LBW COMM to obtain V_{hpcc}	island mode	dSpace

Table 7. Bibliographical analysis.

Ref	Cont. Strategy	MG Struc.	Red model	VA Experimental/Simulation	Perform. Parameters	COM	Connected/Non Connected	CPLTF
[44]	Passivity+ PR	Rad.	RL	0.7 kW/10 kW Lin.	VM-DPC better plug&play performance vs DQ strat. SP_I << (vs. 60% with conventional), T_{ssI}=1 cycle(4 cycles with DQ);Δf=+- 0.1 Hz; THD_v y THD_i<5%	without COMM	island mode	dSpace
[54]	1° DQ "Flatness strategy" 2° Phase angle control/decentralized	Radial	RL with Z_l in D-Q	Lin % NL/ Lin & NL	suitable power sharing P & Q; THD< with NL load	PMU-GPS; LBW bus	island mode	dSpace
[45]	1° Droop control switched with correction method	Radial	RL with Z_l	Linear 2 kW 0.9 kVAR	ΔP_max=0.14 % (0.17%), ΔQ_max=0.04% (13.74%) sim;	without COMM	Island mode	NS
[55]	1°FCS-MPC/DQ + CDC 2° RVI Centr.	Rad.	RL con Z_l	1.8 kW,1.6 kVAR, Lin.	400 times faster recovery in V y f improved dynamical and steady state performance	NS	Island mode	dSpace
[46]	1° DQ 2°WFBC	Rad.	Small signal full model & Z_l	3X720mH/3X5 Ohm	Smaller ΔV & Δf, higher dynamical stability. T_{ssf} ≈ 0.68 s SP_f=0.8% SP_V=0.012%; With Plug & play converters SP_f=0.5 % and SP_V=0.015 %, THD_V<5%.	without COMM	Island mode	dsp
[49]	1°DQ 2°Droop-Mod.	Rad.	RL accurate model of CCPM	Sim Z=4Ω Exp. 8.7 kVA/4.8 kVA	Reactive P. sharing vs CDC, Q_{circ} «, P_{circ}«, smaller current distortion	CAN-Bus	Island mode	DSP

Table 8. Bibliographical analysis.

Ref	Cont. Strategy	MG Struc.	Red model	VA Experimental/Simulation	Perform. Parameters	COM	Connected/Non Connected	CPLTF
[56]	1°CDC & virtual impedance 2°Distributed	Rad.	Z_l y Z_{virt}	sim 4.5 kW; Exp. R, L & C	sim suitable dynamic performance. Power sharing accurate/ Exp: T_{ssI} = 2cycles to reconnect	CAN-COM	Island mode	NS
[57]	1°CDC DQ, (DG1 VCM y DG2 CCM) 2° Droop	Rad	RL/small signal	RL RL	Sim. interconnected T_{ssQ} = 0.3 s (vs 1s), SP_{maxP} = 10% (vs 25%), SP_{maxQ} = 23% (vs 40%), $V_pcc = 0.85\ pu$ connected to island mode/ Exp. connected T_{ssQ} = 0.55 (vs 1.35s); smooth transition	Sim. ZOH cwith t_d = 5 ms/ Exp. NS	Both	NS
[58]	1° LC DQ., droop control, limited current, SEPFC 2° PI	Ring	RL with Z_l	Sag voltage; 35 kW on MG	SEPFC is robust in large transient; f recovery in t= 10 s.	NS	island mode	DSP
[59]	1° DQ,P-U/Q-f droop control, complex virtual impedance	Rad.	RL con Z_l	Sim. 1 kW, 0.5 kVAR	Sim. ΔV=1%, T_{ssV} = 0.02 s, control parameters sensitivity/ Exp. suitable power sharing P & Q unlike the other strategies	without COMM	island mode	NS
[60]	1°Droop C. 2° DLPF based control	Rad.	RL with Z_l, Dynamic phasor model	Exp: 3X910 W	$\Delta P_{max} = 3.9\%$(vs 5.9%) Δf_{max} = 9.3 mHz full load (vs 120 mHz), $T_{ssP} = 5.1$s (vs 15.2 s);	without COMM	Island mode	DSP
[48]	1° DQ, Droop C. 2°modified P loop	Rad.	small signal model & Z_i	PQ_1=13.5 kVA, PQ_2= 0-15 kW+5kVAR	DCG has am identical performance; tracks P without oscillations, $T_s sP$=1 s; it is capable to work with 0.5 rad/s_2, gibing inertia & $PO_{maxP} = 20\%$	without COMM	Both	dsp

Table 9. Bibliographical analysis.

Ref	Cont. Strategy	MG Struc.	Red model	VA Experimental/Simulation	Perform. Parameters	COM	Connected/Non Connected	CPLTF
[61]	Hierar.& optimization	Radial	Z_l NS	–/3X30 kW	Optimal convergence	without COMM	Connected	Python
[62]	Proportional DG power sharing& distributed controllers	Distributed MGs	with Z_l	-/4X200 1X400 kVA	t_{ss} = 20 s in apparent power	LBW bus	islanded	Opal-RT

• Abbreviations for Tables 4-9:

Non-specified (NS); Not included (NI); Full-bridge (FB); Low-band-width (LBW); Linear control (LC); Non-linear Control (NLC);Control platform (CPLTF).

• Abbreviations for journals:

Transactions on power electronics (TPE); Transactions on smart grids (TSG); Applied power electronics conference and exposition (APEC); Transactions on industrial electronics (TIE); Journal of emerging and selected topics in power electronics (JESTPE).

4. Research motivation

The main topics focused on the research of advanced functions in interconnected PV inverters in high penetration levels of low voltage systems are an open issue due to its continuous evolution together with the technological challenges to manage the energy supplied to the loads in a MG; this leads to the modification of the restrictions imposed by the standards to allow the overall operation of a MG interconnected to the AC mains. Therefore some of these challenges to consider are mentioned bellow:

- In general terms, the solutions to the AC mains problems are addressed separately in the literature; as a consequence a fundamental issue is the whole control strategy operation where the inverter is capable to carry out smart functions to mitigate the system operation problems.
- Mainly, the equipment in the market currently depends mostly on the information obtained from the system environment, through distance communication to be capable of operating efficiently, it has certain advantages owing to the DGUs working in centralized control structures achieves more accurate optimal operation.
- The existing studies in the literature address the energy management problem through forecasting solutions where the time scale use to be hourly throughout the day, hence another opportunity area to improve is the dynamic performance of the entire system operation by considering the transient response parameters at smaller time scales, owing to the control levels in a hierarchical control structure must accomplish the required tasks.
- The solutions regarding the energy management in PV inverters currently have an opportunity to consider solving the problem through optimal solutions to improve the system performance as long as the high penetration issues are addressed.
- The control strategies used to solve optimal scenarios have been validated only via simulation in the literature. This is also a challenge to validate its performance with experimental tests.
- According to the continuous changes and modifications on the restrictions considered in the standards, there is an open issue to accomplish these requirements, mainly related to issues as voltage and frequency deviations, reactive power compensation as well as harmonic content in the current waveform, assessing the PV systems are capable of operating under these considerations.

- Due to the aforementioned situation there is another motivation in the research, which is the appropriate selection of the topology and the control strategies that best meet the characteristics imposed to design an intelligent converter.

5. Hypothesis

Optimal operation of an AC microgrid can be achieved by the proper selection and design of a supervisory control system at the tertiary level of a hierarchical control structure that operates as an energy management system, where it is not necessary to include the details of system modeling at the tertiary level, but only at the primary and secondary levels of this strategy. Similarly, it is possible to consider inverter structures with appropriate characteristics to operate a purely PV-based microgrid system without energy storage, connected to the AC mains and working with grid-forming and grid-feeding converters. In this way, advanced functionalities such as voltage and frequency regulation, non-unity power factor operation, and restoration capabilities can be provided to distributed generation units to cope with high PV penetration problems such as voltage and frequency deviations, reverse active power, and black-start scenarios.

6. Research justification

As it is mentioned above, high penetration issues related to the use of RES as DGU in interconnected MG continue being an open problem owing to the necessity of supplying power closer to the connected loads as well as applying more suitable solutions to improve the energy management through the electric power system, where optimal solutions take place in a variety of scenarios according to the end user and the focus and interests of each system. Hence the proposed energy management system in this thesis is designed to solve the MG requirements through grid-feeding and grid forming structures, and to accomplish the standards exigencies regarding to extended functions of PV inverters facing voltage and frequency deviations, reverse active power scenario, optimal power sharing and black-start operation.

7. Objectives

7.1. Overall objective

To design and validate the suitable control strategies in the corresponding levels of a hierarchical control structure, as well as the optimization strategy in the energy management system, to operate the AC microgrid working with grid-feeding and grid forming converters in an optimal power sharing scenario. In this way, high penetration problems, such as voltage and frequency deviations, reverse active power and black-start scenarios, can be solved through PV systems operating together autonomously, providing extended functionalities and power system supporting functions, such as voltage and frequency regulation, non-unity power factor operation, and restoration capabilities.

7.2. Particular objectives

- To select a suitable MG structure to allow using energy management strategies and providing extended functionalities to the PV inverters.
- To obtain the mathematical model of the system components to allow establishing a suitable control strategy with energy management purposes through a hierarchical structure in the MG connected to AC mains.
- To design the selected control strategy in the primary and secondary levels and validate through simulation results, allowing further experimental tests.
- To define power electronics prototypes to allow validating the control strategy operation experimentally.
- To evaluate different optimization algorithms suitable to solve the economic dispatch problem in an optimal power sharing scenario.
- To validate in simulation the optimal power sharing scenario through the hierarchical control structure working with the entire MG system, as well as the optimization and voltage deviation scenarios.
- To assess the performance of the MG system facing a black-start scenario.

8. Methodology

The development of this research work implies particular activities to carry out in order to complete the thesis document. Each activity is described bellow:

1. The first stage is oriented to develop a bibliographical review, as well as the state of the art that allow placing the work in the context of what have been made before and to define the achievement of this research work.
2. To design and implement the control strategies selected to operate at the first level of the hierarchical control structure.
3. To test and compare optimization algorithms applied to solve economic dispatch scenario for the AC microgrid system.
4. To validate the optimization algorithm suitable for operating in the tertiary level of the hierarchical control, and sending the optimal references to the secondary and primary level.
5. To include the system dynamics in the solution of the selected optimization algorithm, and assess its accuracy.
6. To assess the algorithm and grid-feedings performance in a power sharing scenario and compensating voltage deviations.
7. To develop a start-up procedure to assess the microgrid system performance facing a black-start scenario.
8. To carry out a complementary research stay in Aalborg University (AAU) to participate as PhD Guest and get involved in different activities of the Center for Research on Microgrids (CROM), with the purpose of extending the knowledge related to power systems and microgrids topics in which AAU has extensive experience.
9. To present the research results, demonstrating the validity or limitation of the hypothesis.
10. To report the results and the conclusions obtained by writing of the thesis document as well as publishing the journal paper.

9. Thesis scheduling

This thesis work includes an Introduction with the state of the art of the main considerations of the photovoltaic-based microgrid systems facing high penetration levels as well as the relevant standards regarding photovoltaic systems integration and operation. Chapter 1 contains the system definition and its mathematical modeling considerations and validations to design appropriate control strategies. Chapter 2 depicts the design and implementation of the control strategies at the primary control level, where the active and reactive power capabilities to the grid-feedings and voltage regulation to the grid-forming are proven. Chapter 3 analyzes optimization methods for the third control level, allowing the optimal power sharing scenario focused in economical operation. Chapter 4 contains the simulation results for the entire microgrid system, where the optimal operation in different scenarios is tested, also considering reactive power compensation capabilities, and dynamical performance and black-start sequence are validated. Finally the conclusions and contributions of this work are drawn as well as the considered future work for the research work.

CHAPTER 1

AC MICROGRID SYSTEM MODELING

Nowadays, the PV-based distributed generation units (DGU) working in a MG are considered among the solutions to address the high penetration issues in low voltage systems; they can be voltage and frequency variations, non-suitable active and reactive power distribution, connected and island mode operation, as well as the challenges imposed by the standards that must be met in terms of power quality according to the region that they are installed. In this sense the control strategies play an important role, where the power electronics converters are able to perform the necessary control tasks and depending on the specific objective they can work in different time scales [7, 15, 63]. In this chapter the Alternating Current Microgrid (ACMG) system considered in this research work is established, as well as the power electronics converter working together with the PV system in each DGU. After that the control strategy is defined, it is designed through using a mathematical model suitable to accomplish the control tasks required.

1.1. AC microgrid system problem formulation

The MG as an active entity working together with the power system must deal with the technical challenges brought with the growing addition of DGU in low voltage distribution network. Hence, the structure must consider a suitable configuration that allows its operation and also solving the problems in the main possible scenarios. As it is mentioned in the Introduction, the main characteristics of the MG Renewable Energy-based structure to be considered can be listed as follows [12, 64, 65]:

- Renewable Energy-based Distributed Generation Units (RE-based DGU).

- Small Energy Storage Systems (ESS).
- Critical and noncritical loads.
- Islanded and connected modes capabilities.

From the above, the considered system consists in a radial architecture with three PV-based grid-feeding and one grid-forming converter connected to AC mains through the Point of Common Coupling (PCC), as it can be seen in Fig. 1.1. The green side is the MG and the red side corresponds to the AC mains [66, 67], to provide to the MG a reference voltage and allow the system active and reactive power exchange, as well as a smooth connection with AC mains, a Back-to-Back (BTB) converter is used, where others advantages of using this type of converter structure in MG have been proven; they can be as below [68–70].

- Providing total frequency isolation between AC mains and the MG.
- Sharing a desired amount of active and reactive power between AC mains and the MG.
- The variations in voltage and frequency in AC mains can be avoided in MG side.
- Allowing disconnection and connection properly sequenced after a blackout scenario [62, 71].

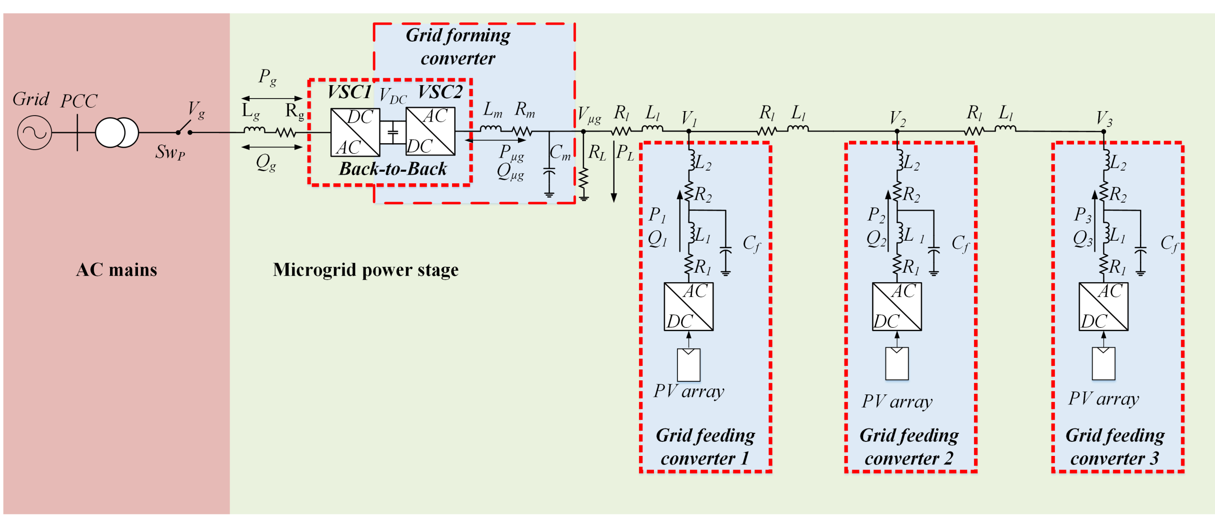

Figure 1.1. AC MG with three PV energy-based grid-feeding converters in radia array.

The VSC_2 in the BTB converter acts as grid-forming, where the control objectives are to regulate the amplitude and frequency of the AC voltage in the MG, through voltage and frequency references in an abc reference frame control strategy, or v_d and v_q references in a $dq0$ reference frame control strategy. [40,72,73]. It makes possible the PV-based grid-feedings are capable of supplying the required active and reactive power demanded by the load connected and the MG. Furthermore this system does not consider an ESS according to the necessity of operation cost reduction [74,75], as well as to explode the PV systems capabilities without energy storage in a MG [36,76]. In this sense, the BTB always must provide a backup of energy from the AC mains, in case it is needed, consequently the island mode is not considered for this purpose. The line impedance between converters is also considered, owing to the influence in the LCL filters, and the whole MG performance [77]. It is defined by Eq.(1.1). The impedance:

$$\mathbf{Z}_l = R_l + j\omega_\mu L_l, \tag{1.1}$$

where ω_μ is the angular frequency of the MG voltage.

Once the MG system to study is defined, in order to design and validate an appropriate control strategy, a suitable mathematical model has to be developed, where the level of detail takes an important role to obtain the dynamic response suitable to depict the whole interaction among the main components of the MG that can lead to instability [78,79]. According to the previous review of PV inverters topologies in the Introduction, a Single-phase Full-bridge (SPFB) converter structure is considered, where this type of topology allows to supply active and reactive power with its PCC to accomplish the standard restrictions and load requirements, as well as ancillary services when is needed. The corresponding schematic of a PV energy-based single-phase grid-feeding converter with its main components is shown in Fig. 1.2, [40].

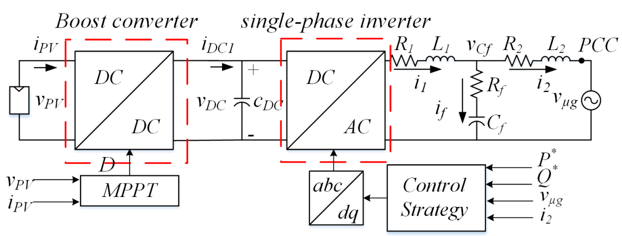

Figure 1.2. Schematic diagram of the PV Energy-based grid-feeding converter.

The boost converter regulates the DC Bus voltage V_{DC} commonly through the use of an MPPT algorithm to send all the power available at certain time of the day; this power is sent with the grid-feeding converter and its control system which is capable to regulate the active and reactive power supplied to the PCC [80]. This system also considers an output LCL filter with higher harmonic attenuation than an L filter, and includes benefits such as size, cost and lower weight [81]. $R_{1,2}$ are the parasitic resistance of the inductors (Ω), $L_{1,2}$ are the inductances (H), R_f is the parasitic resistance of the capacitor and C_f is the capacitance (F). C_{DC} is the capacitance of the DC bus (F), i_{PV} is the PV current (A), i_{dc} is the DC current demanded by the grid-feeding converter (A), V_{dc} is the DC bus voltage (V), and $v_{\mu g}$ is the MG voltage (V).

1.2. Modeling of the photovoltaic panel

The output power of the whole grid-feeding system depends on the power available at certain daily hours and solar irradiation, hence to depict properly the non-linear features of voltage and current electric variables in the PV panel, the mathematical model taken into account is a 3D-look up table-based PV model that collects temperature, irradiation and output voltage, which also contains a two-dimensional data collection represented by Eq.(1.3), where the rows are the solutions of the typical i-v curve given by Eq.(1.2) for each given voltage value at constant temperature, and each column is the solution for each irradiation value G_i (kW/m^2) for the same value of temperature [82–84]. Hence, the current is computed for the set of voltage values $V_i = \{0, V_1, V_2, ..., V_k\}$ and solar irradiation values $G_j = \{G_1, G_2, ..., G_l\}$, where there is an associated 2D-look up table with the form of Equation (1.3) for a constant temperature value, and the results are depicted in the surface of Figure 1.3.

$$i = I_{ph}(G,T) - I_o(T)\left(e^{\frac{v+R_s i}{nN_sV_{th}(T)}} - 1\right) - \frac{v + R_s i}{R_p}, \tag{1.2}$$

$$\begin{pmatrix} i\,(V_1, G_1) & i\,(V_1, G_2) & \cdots & i\,(V_1, G_l) \\ i\,(V_2, G_1) & i\,(V_2, G_2) & \cdots & i\,(V_2, G_l) \\ \vdots & \vdots & \ddots & \vdots \\ i\,(V_k, G_1) & i\,(V_k, G_2) & \cdots & i\,(V_k, G_l) \end{pmatrix}. \tag{1.3}$$

Table 1.1 contains the parameter of the PV panel model ERDM 250 P/6 [85] and its non-linear characteristics are illustrated in the Fig. 1.3.

Table 1.1. PV model parameters ERDM 250 P/6.

Parameter	Value	Parameter	Value
V_{mp}	29.97 V	I_{mp}	8.34 A
P_{max}	250 W	T	25 °C
V_{oc}	37.08 V	I_{sc}	8.86 A

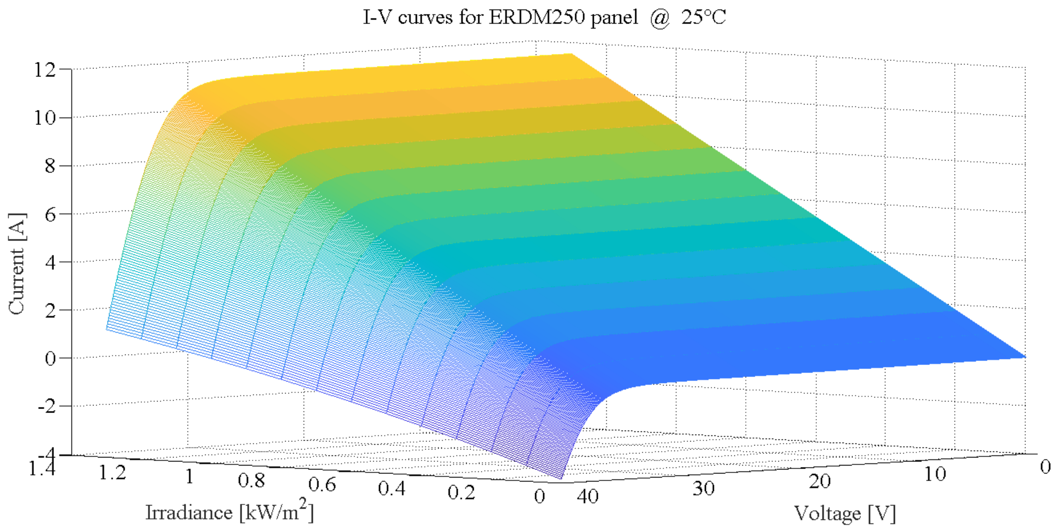

Figure 1.3. Surface of the PV model for ERDM 250 P/6 panel and $T = 25°C$.

Consequently to include the PV model in simulation, each solution is stored in a 3D-look up table for different temperature values $T_i = \{T_1, T_2, ..., T_m\}$. Figure 1.4 illustrates the corresponding surfaces for temperatures from $T = 25°C$ to $T = 65°C$.

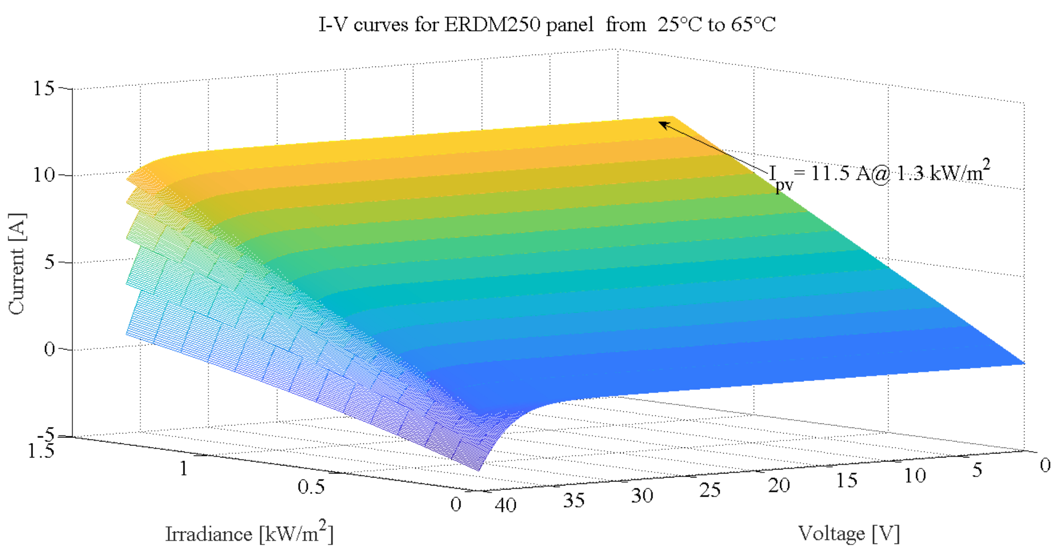

Figure 1.4. Surfaces PV model for ERDM 250 P/6 panel from $T = 25°C$ to $T = 65°C$.

1.2.1. Maximum power point operation

The Maximum Power Point (MPP) is an important parameter to take advantage of the full power available given by the PV panel in determined daily hour, hence a Maximum Power Point Tracking (MPPT) algorithm is considered to keep the PV panel parameters updated in the control system during the entire system operation. In this regard an Incremental Conductance (IC) algorithm is implemented because its suitable performance facing input parameters variations in comparison with the Perturbation and Observation algorithm [86,87]. The Fig. 1.5 illustrates the corresponding flowchart of the IC algorithm, where the output is the voltage reference V_{DC}^{*}.

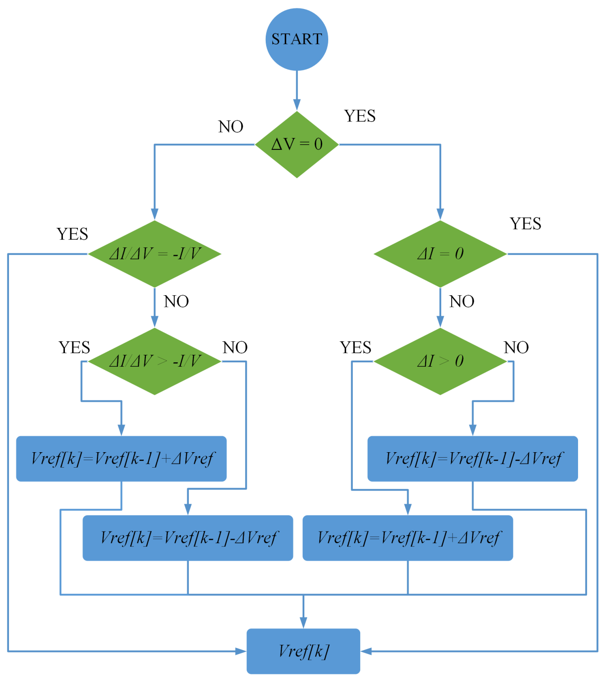

Figure 1.5. Flowchart of the IC-MPPT algorithm.

1.3. AC microgrid power converters configurations

To guarantee the entire system operation and a well designed control strategy, it is important the mathematical model is capable to perform the dynamics of the system with an adequate representation, to solve the control objectives previously established, such as voltage regulation, and active and reactive power regulation.

1.3.1. Modeling of the grid-feeding converter

The Figure 1.6 shows the schematic diagram of the MG system highlighting the grid-feeding structure to study in this work; as it can be seen the model considers a Boost converter to maintain regulated the DC bus at the output and supply power to the SPFB converters which has the control tasks of regulate the active and reactive power injected to the MG.

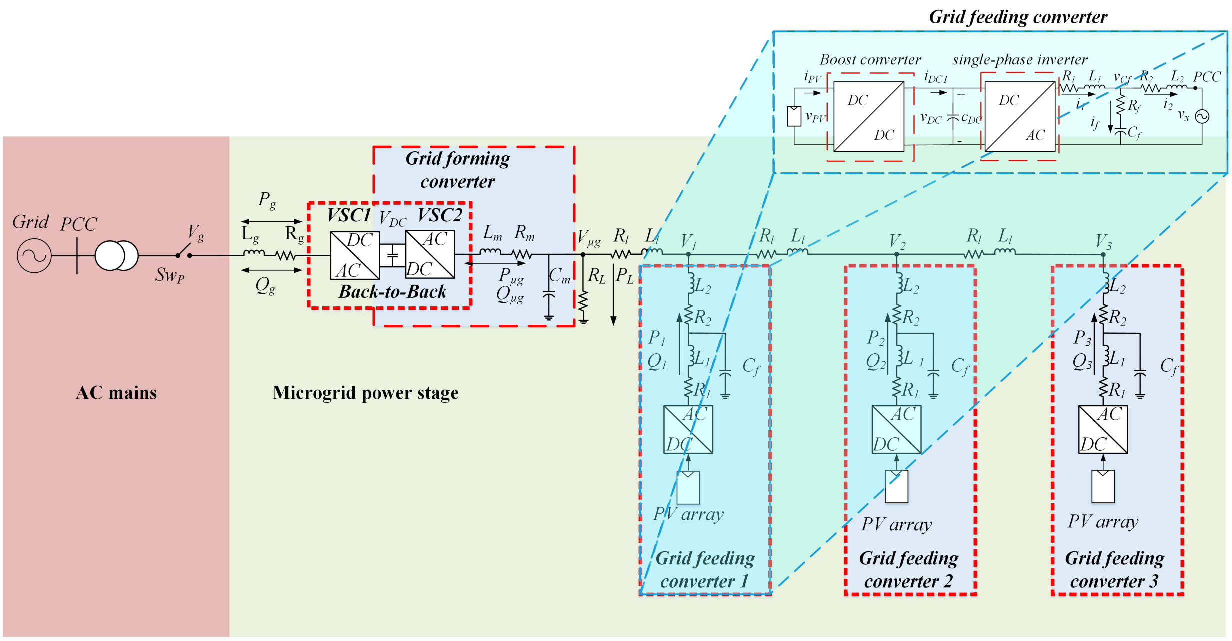

Figure 1.6. AC MG system with PV energy-based SPFB grid-feeding converters in radial array.

The full-bridge PV inverters connected to the MG in the Fig. 1.6 are modeled under the following considerations, taking as reference the Fig. 1.7 [72, 88]:

- The power switches are considered in the ideal case with parasitic elements neglected.
- $S_x = 1$ means the switch is closed and $S_x = 0$ the switch is open.
- The switches in a branch are complementary, i.e. $S_1 = \overline{S_3}$, $S_2 = \overline{S_4}$.
- The capacitance of C_{DC} is large enough to decouple Boost converter and Full-bridge converter.

The Table 1.2 contains the switching values for the Boost converter, where the Eq. (1.4) and (1.5) are obtained with $m_B = (1 - S_B)$ as the switching function of the Boost converter and $m_B \, \epsilon \{0, 1\}$.

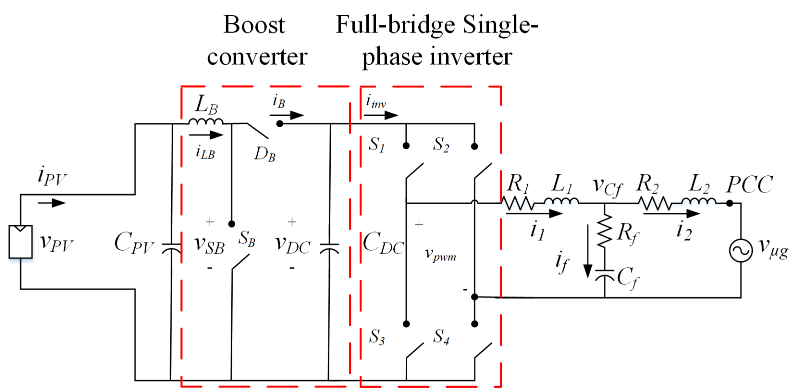

Figure 1.7. PV Energy-based grid-feeding converter.

Table 1.2. Switching states for the Boost converter.

S_1	D_B	v_{SB}	i_B
0	1	V_{DC}	i_{LB}
1	0	0	0

$$v_{SB} = (1 - S_B)v_{DC}, \tag{1.4}$$

$$i_B = (1 - S_B)i_{LB}. \tag{1.5}$$

The mathematical model for the SPFB inverter is obtained also taking the switching states contained in the Table 1.3.

Table 1.3. Switching states for the SPFB inverter.

S_1	S_2	v_{pwm}	i_{inv}
0	0	0	0
0	1	$-v_{DC}$	$-i_1$
1	0	v_{DC}	i_1
1	1	0	0

Eq. (1.6) and (1.7) are derived from the Table 1.3, and the switching function is defined as $m_{inv} = S_1 - S_2$ and is considered with a Sinusoidal Pulse Width Modulation strategy (SPWM) [89].

$$v_{pwm} = (S_1 - S_2)v_{DC}, \tag{1.6}$$

$$i_B = (S_1 - S_2)i_1. \tag{1.7}$$

The dynamical model for this converter is obtained by applying Voltage Kirchhoff Laws (VKL) to the LCL filter in the schematic of the Fig.1.7, deriving the following equation for the MG side of the converter:

$$R_2 i_2 + L_2 \frac{di_2}{dt} + v_{\mu g} - v_{cf} - Rf(i_1 - i_2) = 0, \tag{1.8}$$

and taking Current Kirchhoff Law (CKL) in the capacitor node:

$$i_1 = i_{Cf} - i_2. \tag{1.9}$$

By applying VKL to the Full-bridge converter side in the LCL filter of the Fig.1.7, the Eq.1.8 is given by:

$$R_1 i_1 + L_1 \frac{di_1}{dt} + v_{Cf} + Rf(i_1 - i_2) - v_{pwm} = 0, \tag{1.10}$$

and the corresponding current equations in the node of the capacitor C_{DC} are given by:

$$i_B = i_{C_{DC}} - i_{inv}. \tag{1.11}$$

The equation derived with VKL at the electric circuit in the PV panel is:

$$L_B \frac{di_{LB}}{dt} + v_{SB} - v_{PV} = 0. \tag{1.12}$$

By replacing the switching functions m_B and m_{inv} in the equations (1.4)-(1.7), as well as by replacing the resulting expressions in the equations (1.8)-(1.12), the switched model for this converter is given by [80]:

$$\begin{aligned}
L_1\frac{di_1}{dt} &= -(R_1+R_f)i_1 - v_{Cf} + Rfi_2 + m_{inv}v_{DC},\\
L_2\frac{di_2}{dt} &= R_f i_1 - (R_2+R_f)i_2 + v_{Cf} - v_{\mu g},\\
L_B\frac{di_{LB}}{dt} &= -m_B v_{DC} + v_{PV},\\
C_f\frac{dv_{Cf}}{dt} &= i_1 - i_2,\\
C_{DC}\frac{dv_{DC}}{dt} &= m_B i_{LB} - m_{inv} i_1.
\end{aligned} \tag{1.13}$$

Averaged model of the grid-feeding converter

The assumptions to be considered to derive the averaged model from the switching model are the following:

- The switching frequencies f_{sw} are much higher than AC mains frequency ($f_{sw} >> f_g$).
- The switches are considered ideal elements in the electric circuit.

Taking the Fourier series representation for $m = m_{inv}$ given by the Eq.(1.14), with M as the amplitude and θ the phase angle of the fundamental harmonic and M_k and θ_k the amplitude and phase angle for the $k-th$ harmonic [90].

$$m = Msin(t+\theta) + \sum_{k=2}^{\infty} M_K sin(k\omega t + \theta_k). \tag{1.14}$$

Taking into account the switching frequency is much higher to consider the inductors as high impedance, the harmonic components in the current related to $f_s w$ can be neglected, hence the switching function with u as modulation signal, can be represented as:

$$m \approx u. \tag{1.15}$$

The modulation function for the Boost converter with d as the duty cycle is [88]:

$$m_B \approx (1-d). \tag{1.16}$$

Therefore the averaged model for the SPFB grid-feeding converter is given by:

$$
\begin{aligned}
L_1\frac{di_1}{dt} &= -(R_1+R_f)i_1 - v_{Cf} + Rfi_2 + uv_{DC},\\
L_2\frac{di_2}{dt} &= R_f i_1 - (R_2+R_f)i_2 + v_{Cf} - v_{\mu g},\\
L_B\frac{di_{LB}}{dt} &= -(1-d)v_{DC} + v_{PV},\\
C_f\frac{dv_{Cf}}{dt} &= i_1 - i_2,\\
C_{DC}\frac{dv_{DC}}{dt} &= (1-d)i_{LB} - m_{inv}i_1.
\end{aligned}
\tag{1.17}
$$

Averaged model of the grid-feeding converter in dq synchronous reference frame

The averaged mathematical model in the dq synchronous reference frame is considered to depict the dynamics of the system as DC variables, what makes possible to develop a dq-based control strategy to facilitate the control task of tracking variables to be handled as a regulation task of DC variables, as well as to express active and reactive power variables in terms of dq current and voltage variables [88, 91, 92].

The mathematical model in the dq reference frame of a single-phase electric system requires to apply a single-phase dq transformation technique [91], where the dq components are obtained from the AC current and voltage variables through the mapping transformation of the Eq. 1.18.

$$\mathbf{V_{dq}} = \mathbf{T}\mathbf{V_{RI}}, \tag{1.18}$$

where $\mathbf{V_{RI}}$ is the vector of the real and imaginary components in an orthogonal reference frame of the single-phase variables and T and its inverse matrix are defined by:

$$\mathbf{T} = \begin{bmatrix} sin\theta & -cos\theta \\ cos\theta & sin\theta \end{bmatrix}, \tag{1.19}$$

$$\mathbf{T^{-1}} = \begin{bmatrix} sin\theta & cos\theta \\ -cos\theta & sin\theta \end{bmatrix}, \tag{1.20}$$

where $\theta = \omega t$, and the averaged model for the grid-feeding converter considered in this work in dq components is defined by the following set of equations (1.21), [80]:

$$
\begin{aligned}
L_1\frac{di_1^d}{dt} &= -\left(R_1+R_f\right)i_1^d + R_f i_2^d - v_{C_f}^d + u^d v_{DC} + \omega L_1 i_1^q,\\
L_1\frac{di_1^q}{dt} &= -\left(R_1+R_f\right)i_1^q + R_f i_2^q - v_{C_f}^q + u^q v_{DC} - \omega L_1 i_1^d,\\
L_2\frac{di_2^d}{dt} &= R_f i_1^d - \left(R_2+R_f\right)i_2^d + v_{C_f}^d - v_{\mu g}^d + \omega L_2 i_2^q,\\
L_2\frac{di_2^q}{dt} &= R_f i_1^q - \left(R_2+R_f\right)i_2^q + v_{C_f}^q - v_{\mu g}^q - \omega L_2 i_2^d,\\
C_f\frac{dv_{C_f}^d}{dt} &= i_1^d - i_2^d + \omega C_f v_{C_f}^q,\\
C_f\frac{dv_{C_f}^q}{dt} &= i_1^q - i_2^q - \omega C_f v_{C_f}^d,\\
C_{DC}\frac{dv_{DC}}{dt} &= (1-d)i_{LB} - \frac{1}{2}\left(u^d i_1^d + u^q i_1^q,\right)
\end{aligned}
\tag{1.21}
$$

where

- $v_{\mu g}^d$, $v_{\mu g}^q$, v_{Cf}^d and v_{Cf}^q are the MG voltage dq components in the synchronous reference frame (V).
- i_1^d, i_1^q, i_2^d y i_2^q are the current dq components.
- R_1, L_1, R_2, L_2 , C_f y R_f are the passive elements of the LCL filter.
- ω is the AC angular frequency.
- v_{DC} is the voltage on the capacitor C_{DC}.
- u^d and u^q are modulation functions in dq components.

1.3.2. Modeling of the grid-forming converter

The Figure 1.8 shows the schematic diagram of the MG system highlighting the grid-forming structure; in this case the VSC_1 in the BTB converter must regulate the DC bus allowing the VSC_2 to regulate the AC bus in the MG side to provide a reference voltage to the grid-feeding structures.

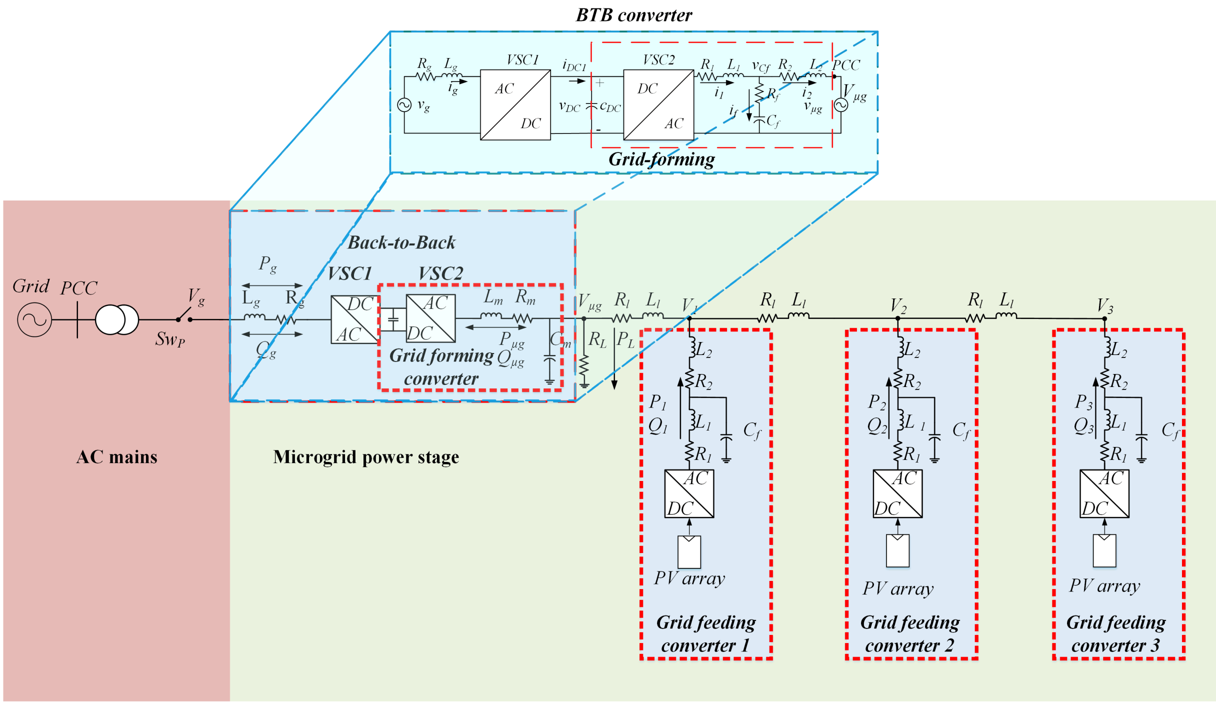

Figure 1.8. Back-to-Back converter working as grid-forming in the PV energy-based AC MG system.

The Figure 1.9 shows the BTB converter working as grid-forming in the MG, where it is considering a SPFB converter in $VSC_{1,2}$ of the BTB, and taking the assumptions made for the grid-feeding model, the mathematical model in dq reference frame of the grid-forming converter is given by the set of equations (1.22).

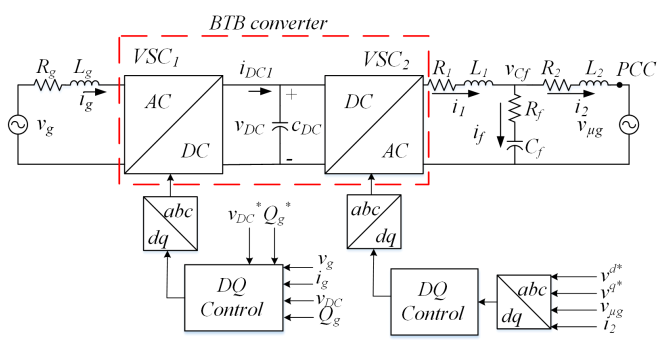

Figure 1.9. Schematic diagram of BTB converter working as grid-forming converter.

$$
\begin{aligned}
L_g \frac{di_g^d}{dt} &= -R_g i_g^d + v_g^d + \omega_g L_g i_g^q - u_g^d v_{DC}, \\
L_g \frac{di_g^q}{dt} &= -R_g i_g^d + v_g^q - \omega_g L_g i_g^d - u_g^q v_{DC}, \\
L_1 \frac{di_1^d}{dt} &= -\left(R_1 + R_f\right) i_1^d + R_f i_2^d - v_{C_f}^d + u^d v_{DC} + \omega_{\mu g} L_1 i_1^q, \\
L_1 \frac{di_1^q}{dt} &= -\left(R_1 + R_f\right) i_1^q + R_f i_2^q - v_{C_f}^q + u^q v_{DC} - \omega_{\mu g} L_1 i_1^d, \\
L_2 \frac{di_2^d}{dt} &= R_f i_1^d - \left(R_2 + R_f\right) i_2^d + v_{C_f}^d - v_{\mu g}^d + \omega_{\mu g} L_2 i_2^q, \\
L_2 \frac{di_2^q}{dt} &= R_f i_1^q - \left(R_2 + R_f\right) i_2^q + v_{C_f}^q - v_{\mu g}^q - \omega_{\mu g} L_2 i_2^d, \\
C_f \frac{dv_{C_f}^d}{dt} &= i_1^d - i_2^d + \omega_{\mu g} C_f v_{C_f}^q, \\
C_f \frac{dv_{C_f}^q}{dt} &= i_1^q - i_2^q - \omega_{\mu g} C_f v_{C_f}^d, \\
C_{DC} \frac{dv_{DC}}{dt} &= \frac{1}{2}\left(u_g^d i_g^d + u_g^q i_g^q + u^d i_1^d + u^q i_1^q\right),
\end{aligned}
\tag{1.22}
$$

where:

- v_g^d, v_g^q are the voltage dq components in the synchronous reference frame.
- R_1, L_1, R_2, L_2 , C_f y R_f are the passive elements of the LCL filter.
- ω_g and $\omega_{\mu g}$ are the AC angular frequency for AC mains and MG side of the BTB converter.
- u_g^d and u_g^q are modulation function in dq components for VSC_1.

1.3.3. Line impedance parameters in microgrids

The MG performance is directly affected by the impedance line parameters due to its behavior at different frequency values and harmonics interactions; hence as it is mentioned in the problem formulation, the line parameters are taken into account in order to include its dynamics in the mathematical model, and how it affects the performance of the entire system operation and in this sense avoid instability issues by means of a suitable design of the control strategy [77, 93].

The distribution line is considered in sinusoidal steady state [94]. Thus the series impedance and shunt admittance per meter are given by equations (1.23) and (1.24), where the lowercase letters indicate distributed parameters, and uppercase letters are used to describe lumped parameters.

$$z = r + j\omega L. \tag{1.23}$$

$$y = g + j\omega C. \tag{1.24}$$

Figure 1.10 shows a transmission line differential section of length dx [94]. Hence, the typical second order differential equations that describes a section of line length dx with series impedance zdx and shunt admittance ydx is given by equation (1.25).

$$\frac{d^2V}{dx^2} = yzV = \gamma^2 V \tag{1.25}$$

where $\gamma \triangleq \sqrt{yz}$ is the propagation constant, and it is expected imaginary solution for equation (1.25). The solution of the differential equation is given by equation (1.26).

$$V_1 = V_2 cosh(\gamma l) + Z_C I_2 sinh(\gamma x) \tag{1.26}$$

where the characteristic impedance of the line is defined by $Z_C = \sqrt{z/y}$ [94, 95]

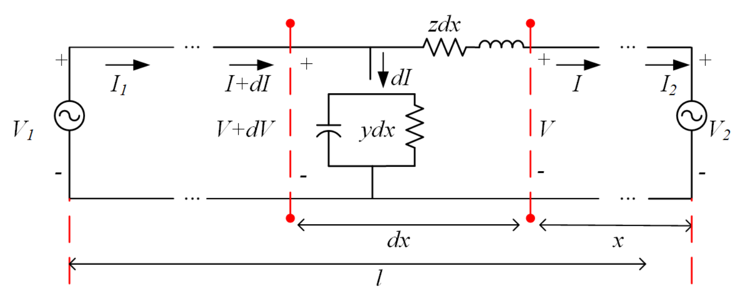

Figure 1.10. Transmission line differential section.

To obtain results closer to real cases related to line voltage deviations, the considered line impedance corresponds to a lumped parameters model of the Eq. (1.27), for a short line with sections of length l (m) with a determined cross sectional area AWG, where resistive and inductive parameters are computed for a single-phase circuit and the conductance is neglected [96, 97].

$$Z_l = R_l + j\omega_\mu L_l. \tag{1.27}$$

To compute R_l and L_l the characteristic impedance Z_C (Ω) is given by Eq.(1.28); it is a real number if losses are completely neglected [95].

$$Z_C \approx \sqrt{R_{DC}^2 + |Z_{HF}|^2}. \tag{1.28}$$

The high-frequency impedance Z_{HF} is defined by the Eq.(1.29), where γ is part of the imaginary component in Z_{HF}, σ_c is the conductor conductivity.

$$Z_{HF} = \frac{\gamma}{2\pi r \sigma_c} (\frac{\mu\Omega}{m}), \tag{1.29}$$

It is also needed to compute the self inductance per phase defined by Eq.(1.30).

$$L_{ii} = \frac{\mu_0}{2\pi} ln \frac{2h_i}{r_i} (\frac{\mu H}{m}), \tag{1.30}$$

where h_i is the height (m) and r_i the geometric mean radius.

The impedance Z_l is obtained by the following expression.

$$Z_l = Z_C + j\omega_\mu L_{ii}. \tag{1.31}$$

Table 1.4 contains the corresponding parameters for the conductor of the line. The computed values are contained in Table 1.5, and their corresponding computation are reported in Appendix A.

Table 1.4. Parameters of the conductor.

Parameter	Value	Parameter	Value
Direct current resistance R_{DC}	$1.27x10^{-3}$ Ω/m	Permittivity ϵ	$\frac{1x10^{-9}}{36\pi}$ $\frac{\mathrm{C}^2}{\mathrm{Nm}^2}$
Ground conductivity σ_t	$1/100$ S/m	Permeability μ	$4\pi x10^{-7}$ N/A^2
Conductor radius r	$4.11x10^{-3}$ m	Conductor conductivity σ_c	$\frac{1}{R_{DC}\pi r^2}$

Table 1.5. Parameters of the MG line impedance.

Parameter	**Value**	**Parameter**	**Value**
AWG	6	l	600 m
R_l	762 mΩ	X_L	372 mΩ
L_l	987 μH	Cross-sectional area	26818 cmil

1.4. Mathematical models validation

The validation of the mathematical models obtained is made carrying out a comparison between detailed switched models and mathematical models through simulation results in open loop; for this purpose the software *Matlab Simulink* in co-simulation with *PLECS* are used to implement the converters that work in the MG system proposed in Fig. 1.11, where the advantages of *Simulink* to solve the differential equations of the dynamic models are also taken into account to subsequently solve the control strategies while implementing the detailed models of the power stage in PLECS.

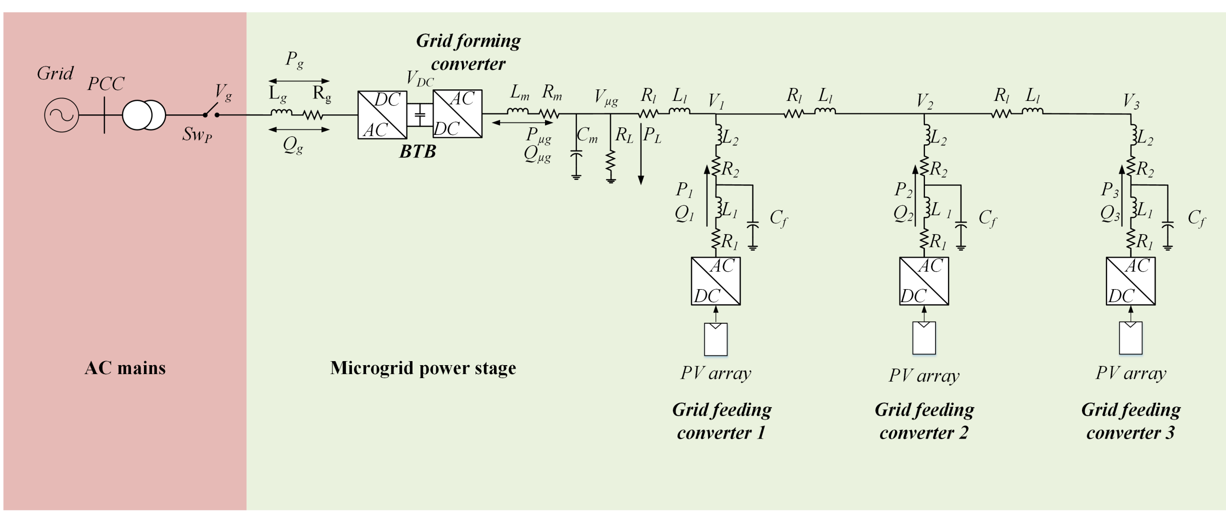

Figure 1.11. AC MG with three PV energy-based grid-feeding converters in radial array.

Table 1.6 contains the nominal parameters considered to validate de mathematical models.

Table 1.6. MG System Parameters.

Parameter	Value	Parameter	Value
V_{DC}	250 V	f	60 Hz
V_{AC}	127 V_{rms}	f_{sw}	12.5 kHz
P	400 W	R_1	142 mΩ
Q	$\pm$0 VAr	R_2	1.11 mΩ
C_m	7.55 μF	L_1	3.03 mH
R_m	267 mΩ	L_2	1.11 mH
R_g	142 mΩ	L_g	3.03 mH
C_f	6.88 μF	$\mathbf{Z}_l$	762 +j372 mΩ
L_m	3.38 mH	$V_{\mu g}$	127 V_{rms}
ma	0.7	θ	0 rad

The BTB structure performing as grid-forming considers both VSC_1 to regulate the DC bus V_{DC} and VSC_2 to regulate the MG voltage $V_{\mu g}$, consequently the corresponding equations to the grid-feeding converter are also considered as well as this structure has been well studied [80].

Fig.1.12 illustrates the validation of the averaged model; the voltage and current variables are depicted in an interval from $t = 0$ s to $t = 1.5$ s. The blue trace corresponds to the averaged model and the red trace to the detailed switched model indicated with the sub-indexes a and d respectively, and they are matched with those sub-indexes in Fig. 1.9. It also shows a zoom of $\Delta t = 0.05$ s, when the variables achieve steady state conditions. As it can be seen, the transient state has a similar behavior, the discrepancy is due to the harmonics neglected in the averaged model, generating small differences before steady state conditions.

Figure 1.13 illustrates the DC bus voltage V_{DC} and the MG voltage $V_{\mu g}$ measured in the same conditions that the currents. It is possible to observe the 120 Hz ripple reflected in the DC bus behavior produced by mapping the 60 Hz component to V_{DC}.

The validation of the averaged dq model is shown in Figure 1.14. In this case it is taken a period of time $\Delta t = 0.2\,s$ in order to observe the steady state conditions of the characteristic DC variables of the dq reference frame, where it can be observed the dq averaged model achieves the values of the dq variables of the detailed model in the simulation.

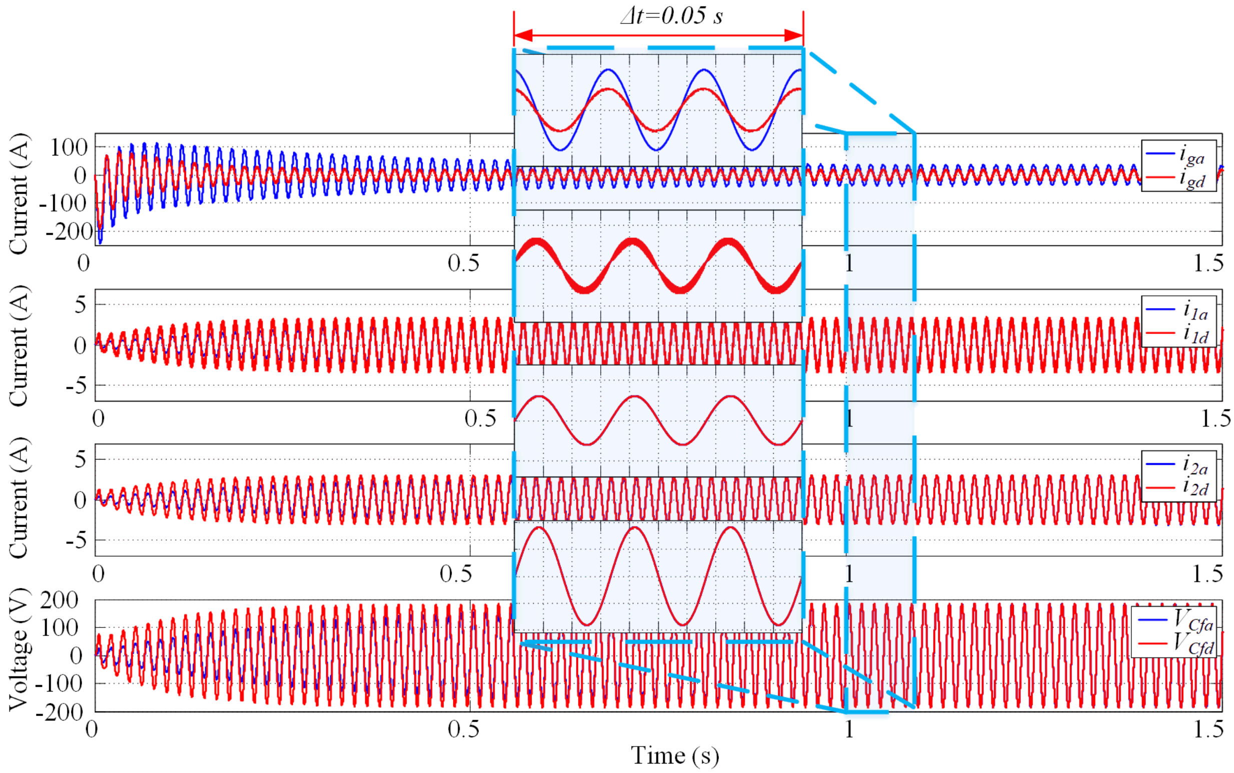

Figure 1.12. Comparison between the detailed and averaged models of grid-forming.

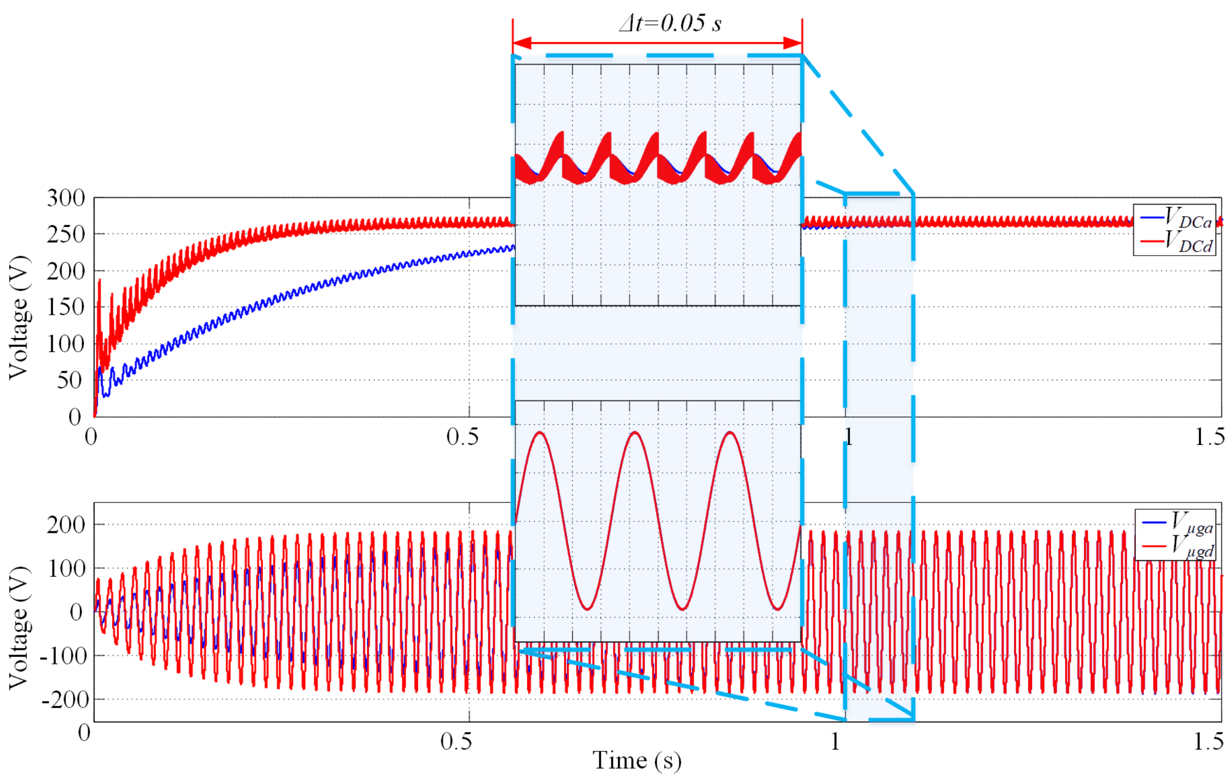

Figure 1.13. Comparison between the detailed and averaged models of grid-forming.

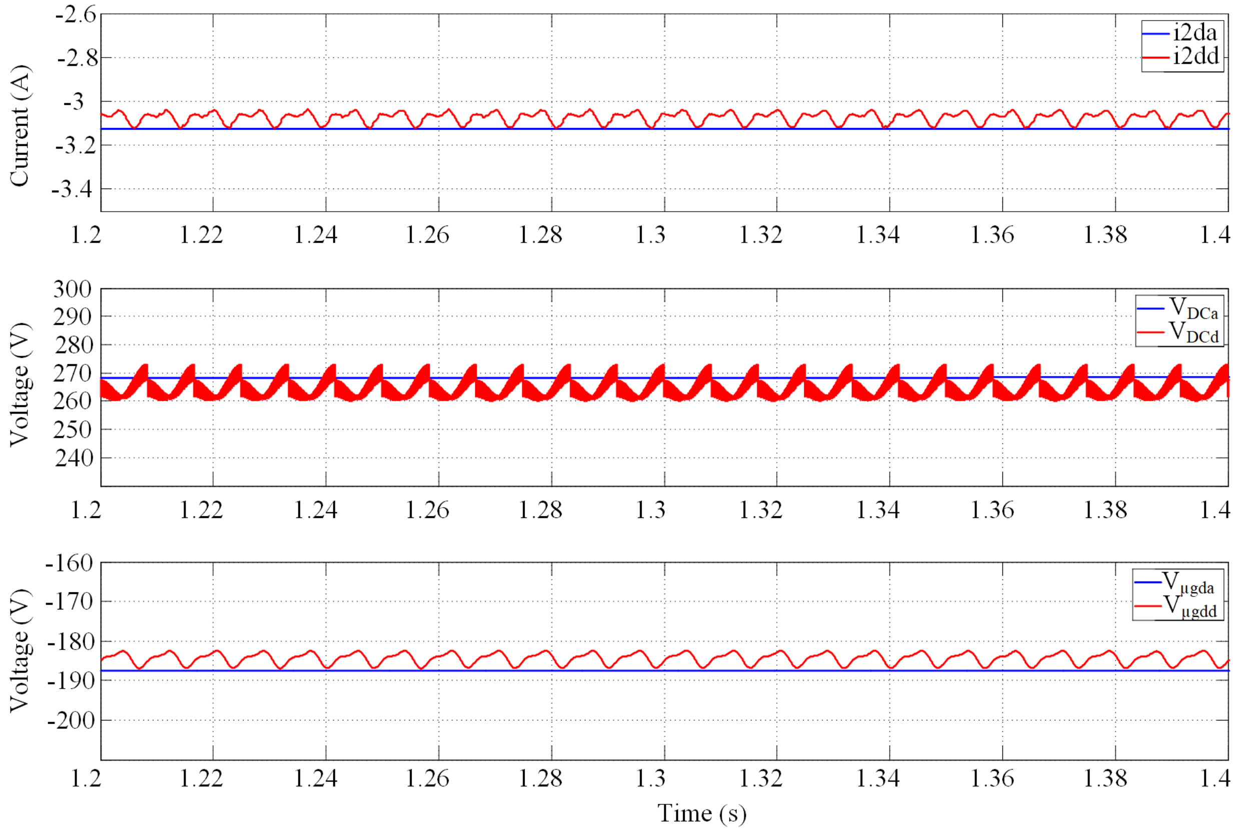

Figure 1.14. Comparison between the detailed and dq averaged models of grid-forming.

1.4.1. Discussion

As it can be observed, the averaged model and the averaged dq model have a discrepancy with the detailed switched model and the detailed model in dq variables because the harmonic content at the switching frequency is neglected, which is mainly reflected in the transient response, where the lack of harmonic content avoid the ripple in the averaged model while having a lower value before reaching the steady state condition. It is also possible to observe that the steady state condition of the dq model in Figure 1.14 is equal to the steady state response of the switched model on its lowest value due to the neglected harmonic components.

CHAPTER 2

Photovoltaic inverter control strategies in a microgrid and their implementation

To carry out the parallel operation of DGU in a MG, the control tasks that the PV inverters must accomplish have to be considered in order to maintain the system parameters between suitable values, improving the system stability and appropriate power sharing operation among the DGU [59]. In this Chapter the control strategy for the MG system is established. The main functions considered to perform by the DGU proposed are the grid-feeding and the grid-forming converter, where the grid-feeding mainly must supply active and reactive power to the energized electric system and the grid-forming is able to work independently in island mode giving the voltage reference for the grid-feedings [40].

One method to solve the main issues regarding MG operation is the Hierarchical Control Structure (HCS), due to the different tasks to be accomplished require being executed in significantly different time scales [63]. The most common HCS mainly consist of three levels [41, 98]:

- The first level performs regulation tasks through the PV inverter. They can be voltage and frequency regulation as well as active and reactive power regulation.
  In this level is possible to give the capabilities of grid-feeding-grid forming or grid-supporting converter, where different control strategies have been well proven and validated; they can be linear control-based [40,73] or non-linear control-based [80,99].

- The secondary level solves the damping and deviation issues of the primary level [53, 100, 101].

- The tertiary level makes sure the MG parameters imposed by the rules and standards are achieved, as well as optimal operation, energy trading, system disconnection and restoration, where the needed references sent to the first level are defined properly according to the established purpose of this level [63, 98].

The above is illustrated in Figure 2.1, where it is possible to observe the bandwidth decreases as the control level increases, hence the control strategies at higher levels operate with higher time scales.

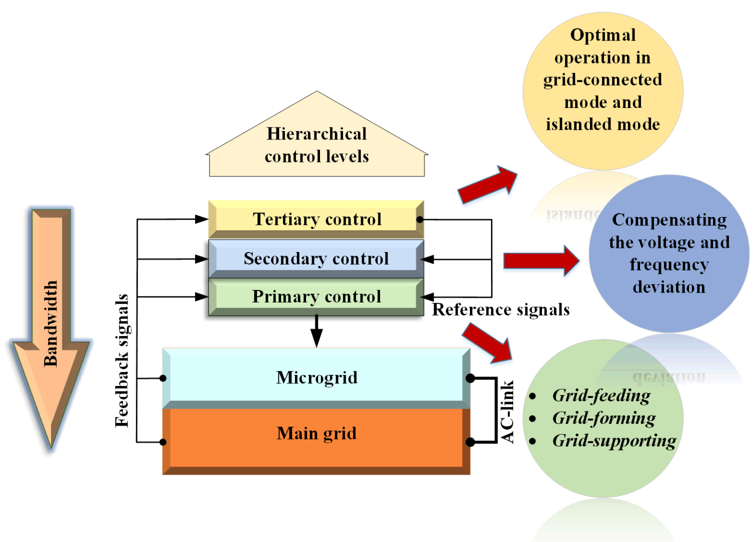

Figure 2.1. Hierarchical Control Structure.

To design and develop the control strategies in their corresponding control level of the HCS, the nominal parameters of the system considered in the Figure B.1 of the Appendix B are used, and they are contained in the Table B.1.

2.1. Primary and secondary control levels

The suitable dynamical performance obtained by the HCS depends on the control strategies selected and implemented in each control level, where primary level (also called *the local controller*) together with the secondary level have an important role to maintain the voltage and frequency levels between allowable boundaries [63]. The literature reports different control strategies, where linear controllers as Decoupled Current Control (DCC) has limited performance working outside its operation point where the plant has been linearized, as well as disturbances sensibility and parametric variations dependency [102]; those limitations can be solved with non-linear control techniques as the Passivity Based Controller (PBC) [103] and Sliding Modes Controller [104], among others control strategies that have been well studied with power electronics converters.

Its is important to highlight that the control strategies at each level can be validated separately, due to the bandwidth of lower levels have faster response, hence the fastest control strategies are capable of receiving the references from the upper levels as constant values or smooth variation variables [105].

2.1.1. Decoupled current control with cascade loops

The DCC strategy with cascade loops is commonly developed in the synchronous reference frame dq and implemented to control multiple power electronics converters and its applications [40, 72]; it presents robustness due to the PI controllers used in the inner and outer loops, where a suitable regulation of the variables is achieved.

2.1.1.1. DCC Design of grid-feeding converter

To design the DCC structure applied to the grid-feeding converter, the mathematical model in dq variables is considered, where the coupling terms in the state equations can be managed by the DCC. These terms can be seen in the set of Eqs. (1.21) of the mathematical model for the grid-feeding obtained in Chapter 1, where the capacitor current in LCL filter is neglected for control purposes, avoiding current sensors in the implementation, improving the system reliability; hence with $i_1 \approx i_2$ the equations are:

$$
\begin{aligned}
L_1 \frac{di_1^d}{dt} &= -R_1 i_1^d - v_{\mu g}^d + u^d v_{DC} + \omega_{\mu g} L_1 i_1^q, \\
L_1 \frac{di_1^q}{dt} &= -R_1 i_1^q - v_{\mu g}^q + u^q v_{DC} - \omega_{\mu g} L_1 i_1^d, \\
C_{DC} \frac{dv_{DC}}{dt} &= i_{DC} - \frac{1}{2} \left(u^d i_1^d + u^q i_1^q \right).
\end{aligned}
\tag{2.1}
$$

Figure 2.2 illustrates the grid-feeding structure, where the DCC strategy in dq variables is applied to the SPFB converter (*DC-AC* converter) and due to the necessity to accomplish certain restrictions by the standards, the Boost converter is not thought to work in MPP scenario, hence its duty cycle is such as the reference i^*_{DC1} is related with the power required by the SPFB converter according to the reference P^*. The control objectives for this converter are:

- To regulate the DC bus V_{DC} with the Boost converter through the reference i^*_{DC1}.
- To regulate the active and reactive power flow P and Q injected to the MG with the DC-AC converter.

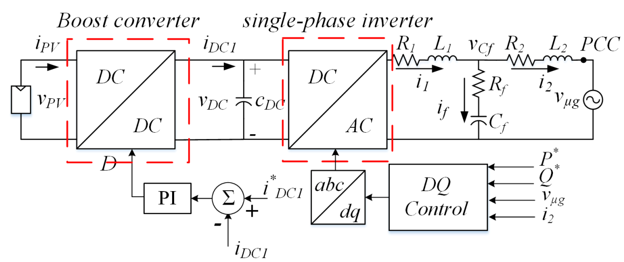

Figure 2.2. Schematic diagram of the PV Energy-based grid-feeding converter.

The DCC strategy makes the following considerations:

- The DC bus is regulated to its reference value injecting i_{DC1} to the inverter.
- The bandwidth of the inner loops operates at least one decade lower than the switching frequency of the PV inverter.
- The bandwidth of the outer loops operates at least one decade lower than the bandwidth of the inner loops.

From the Eqs.(2.1), given the dq modulation index u^d and u^q as the control variables, the following control law is proposed to decouple the equations of the mathematical model [72]:

$$\begin{aligned} u^d &= \frac{L_1}{V^*_{DC}}\left[\frac{R_1}{L_1}i^d_1 + L_1\omega_{\mu g}i^q_1 + \frac{v^d_{\mu g}}{L_1}\right] + U_1, \\ u^q &= \frac{L_1}{V^*_{DC}}\left[\frac{R_1}{L_1}i^q_1 - L_1\omega_{\mu g}i^d_1 + \frac{v^q_{\mu g}}{L_1}\right] + U_2, \end{aligned} \tag{2.2}$$

where V_{DC}^* is the reference value of DC bus voltage and U_x with $x \epsilon \{1, 2\}$ are the output of PI controllers to regulate its corresponding variable.

Figure 2.3 illustrates the block diagram of the DCC, where $\omega_{\mu g}$ is the MG frequency measured by a PLL structure and once u^d and u^q are obtained, the transform dq to $\alpha\beta$ is used to obtain the modulation index u_α, which is compared with the carrier signal in the SPWM technique.

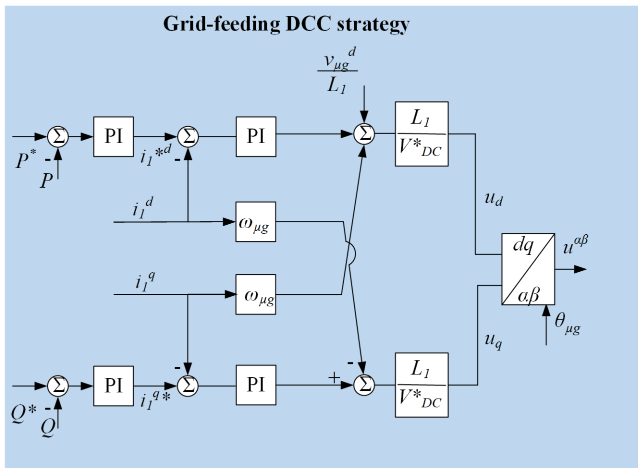

Figure 2.3. Control block diagram of the DCC strategy applied to the grid-feeding.

The PI controllers in the inner and outer loops are defined by:

$$U_1 = k_{p1}(i^{d*} - i^d) + k_{i1} \int (i^{d*} - i^d) dt, \tag{2.3}$$

$$U_2 = k_{p1}(i^{q*} - i^q) + k_{i1} \int (i^{q*} - i^q) dt, \tag{2.4}$$

where k_{p1} is the proportional gain, k_{i1} is the integral gain, i^{d*} and i^{q*} are desired value of the currents.

By replacing (2.3) and (2.4) in the set of Eqs. (2.2), it results in the linear mathematical model given by the Eqs. (2.5) and (2.6).

$$\frac{d}{dt} i_1^d = U_1, \tag{2.5}$$

$$\frac{d}{dt} i_1^q = U_2. \tag{2.6}$$

Therefore the corresponding transfer functions of each closed loop control given by Equations (2.5) and (2.6) are:

$$G_1(s) = \frac{i^d(s)}{i^{d*}(s)} = \frac{(k_{p1}s + k_{i1})}{s^2 + k_{p1}s + k_{i1}}, \tag{2.7}$$

and to obtain the transfer functions of the active and reactive power loops, it is used their definition in terms of the dq variables [72]:

$$\frac{P}{P^*} = \frac{k_{pp}v^d_{\mu g}s + k_{ip}v^d_{\mu g}}{\left(k_{pp}v^d_{\mu g} + 2\right)s + k_{ip}v^d_{\mu g}}, \tag{2.8}$$

$$\frac{Q}{Q^*} = \frac{k_{pq}v^d_{\mu g}s + k_{iq}v^d_{\mu g}}{\left(-k_{pq}v^d_{\mu g} + 2\right)s - k_{iq}v^d_{\mu g}}, \tag{2.9}$$

where k_{pp}, k_{ip} are the gains of the active power loop PI controller and k_{pq}, k_{iq} the gains of the reactive power loop PI controller. These closed-loop transfer functions avoid the zero effect due to the location of the pole is at the same frequency of the zero, which can be proven with the selected values.

Tuning of the PI controllers

The bandwidth decoupling criteria is used to give the dynamical features desired to the control loops [73,102]; this guarantees the inner loops dynamics being faster than the outer loops dynamics. Also by applying Routh-Hurwitz criteria to the transfer functions of the Eqs. (2.7)-(2.9), to guarantee system stability the poles of the system must lie within the left-half of the s-plane; this condition is achieved with the following considerations:

$$k_{p1} > 0, k_{i1} > 0, k_{pp} > 0, k_{ip} > 0, k_{pq} > 0, k_{iq} > 0, \tag{2.10}$$

where there are different methods to obtain maximum upper limits of the proportional and integral gains, which are not addressed in this work owing to its is beyond the established purposes.

To accomplish the necessary condition for bandwidth decoupling, the bandwidth of the inner loop is proposed $f_i < \frac{2f_{sw}}{10}$ kHz, one decade lower than switching frequency.

Table 2.1. Nominal MG System Parameters.

Parameter	**Value**	**Parameter**	**Value**
V_{DC}	250 V	f	60 Hz
$V_{\mu g}$	127 V_{rms}	f_{sw}	12.5 kHz
S	1000 VA	R_1	142 mΩ
L_1	3.03 mH	R_2	1.11 mΩ
C_f	6.88 μF	L_2	1.11 mH
R_g	142 mΩ	L_g	3.03 mH

The proposed proportional and integral gains of the inner and outer loops are contained in the Table 2.2; Table 2.1 lists the parameters considered for this purpose. Figure 2.4 represents the block diagram of the active power closed loop that generates the current reference i_1^{d*} to the inner loops of the DCC strategy, and the Figure 2.5 represents the block diagram of the reactive power closed loop that generates the current reference i_1^{q*}. Since the droop control schemes are designed to give grid-supporting capabilities, they are not considered for the grid-feeding structure [40, 48, 106].

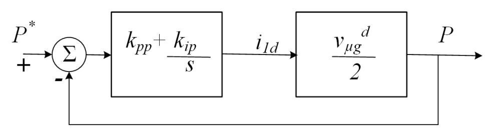

Figure 2.4. Block diagram of the active power closed loop.

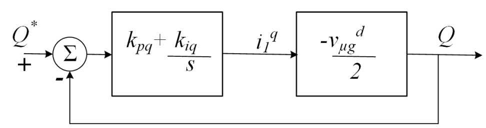

Figure 2.5. Block diagram of the reactive power closed loop.

Table 2.2. DCC Grid-feeding converter parameters.

DCC grid-feeding			
Parameter	**Value**	**Parameter**	**Value**
k_{p1}	550	k_{pp},k_{pq}	0.0065
k_{i1}	700	k_{ip},k_{iq}	0.0099

The Bode diagram of the Figure 2.6 depicts the frequency response of the inner and outer loops, highlighting the bandwidth decoupling at - 3 dB of magnitude; it is possible to observe the cutoff frequencies accomplish the necessary condition of bandwidth decoupling.

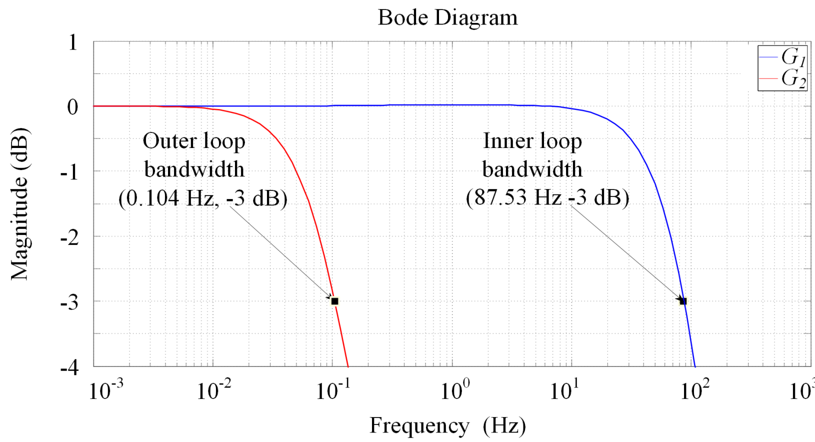

Figure 2.6. Bode diagram of the closed loop transfer functions.

2.1.1.2. DCC design of the grid-forming converter

The Figure 2.7 illustrates the BTB converter connected to AC mains, where both VSC_1 and VSC_2 have a SPFB structure in which DCC strategy is applied; the VSC_2 works as grid forming converter as it is previously described. The control objectives are listed bellow.

Control objectives for the VSC_1

- To regulate the DC bus V_{DC}.
- To regulate the reactive power flow Q between AC mains and the MG.

Control objectives for the VSC_2

- To give an AC voltage amplitude and frequency references with $V_{\mu g}$ to the grid-feeding converters in the MG by tracking of $v^{d,q}$ references.

The block diagram of the DCC strategy for the VSC_1 of the BTB converter is illustrated in Figure 2.8, where the corresponding outer loops regulate the DC bus v_{DC} and the reactive power Q_g measured at PCC with AC mains.

In this case, the transfer function for the inner loop is:

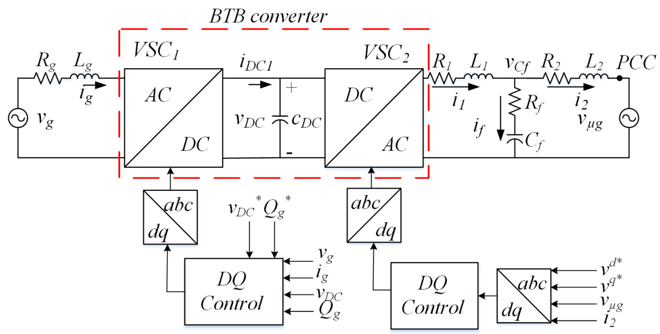

Figure 2.7. Schematic diagram of BTB converter working as grid-forming converter.

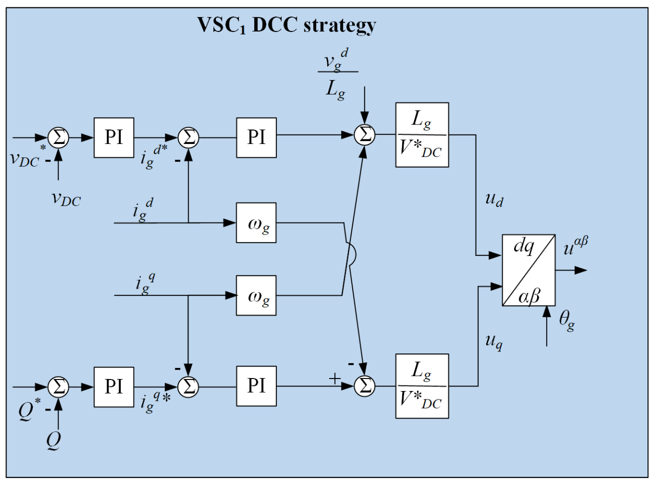

Figure 2.8. Control block diagram of the DCC strategy applied to the VSC_1 of the grid-forming.

$$G_g(s) = \frac{i_g^{d,q}(s)}{i_g^{d,q*}(s)} = \frac{(k_{pg}s + k_{ig})}{s^2 + k_{pg}s + k_{ig}}. \tag{2.11}$$

Figure 2.9 represents the block diagram of the v_{DC} closed loop that allows to send the current reference i_g^{d*} to the inner loop of the DCC strategy [72]. The transfer function is given by (2.12).

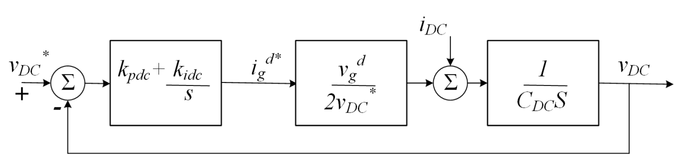

Figure 2.9. Block diagram of the v_{DC} closed loop.

$$\frac{v_{DC}}{v_{DC}^*} = \frac{k_{pdc}v_g^d s + k_{idc}v_g^d}{2C_{DC}v_{DC}^* s^2 + k_{pdc}v_g^d s + k_{idc}v_g^d}, \tag{2.12}$$

where k_{pdc}, k_{idc} are the proportional and integral gains.

Tuning of the PI controllers

The corresponding block diagram to regulate the reactive power exchanged with AC mains is similar to the reactive power control in the grid-feeding structure. In this case the proportional and integral gains for the reactive power control in the VSC_1 are k_{pqg} and k_{iqg}.

The proposed proportional and integral gains of the inner and outer loops are contained in the Table 2.3.

Table 2.3. DCC Grid-forming converter parameters.

DCC VSC_1 grid-forming			
Parameter	**Value**	**Parameter**	**Value**
k_{pg}	830	k_{ig}	10
k_{pdc}	0.25	k_{idc}	1.5
k_{pqg}	0.0095	k_{iqg}	1.4

The Bode diagram of the Figure 2.10 shows the resulting bandwidth of the inner loop for the i_g^d current and the outer loop for the v_{DC} voltage, accomplishing with the decoupled bandwidth criteria.

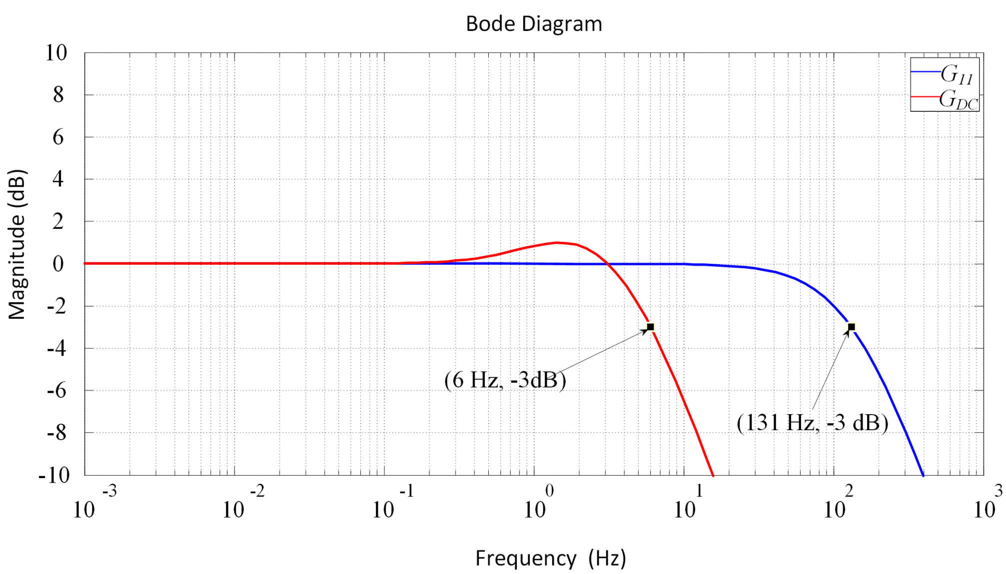

Figure 2.10. Bode diagram of the closed loop transfer functions of i_g^d and V_{DC}.

The Bode diagram of the Figure 2.11 shows the resulted bandwidth of the inner loop for i_g^q current and the outer loop to regulate reactive power $Q_{\mu g}$, where the lower bandwidth is due to the controllers must regulate constant variables in dq .

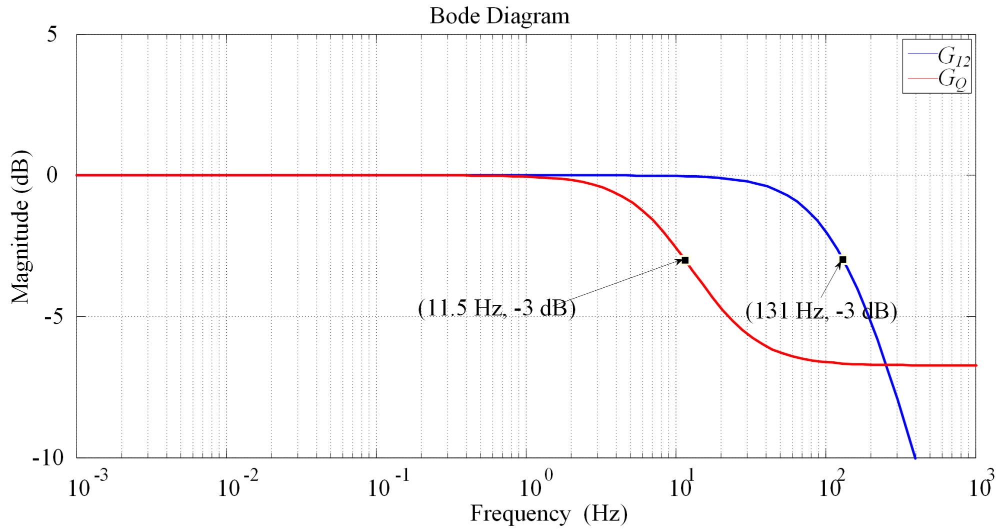

Figure 2.11. Bode diagram of the closed loop transfer functions of i_g^q and $Q_{\mu g}$.

The procedure of tuning the control loops to regulate dq voltages in the MG is done considering their corresponding outer loops as it can be seen in Figure 2.12, where the references $v_{\mu g}^{d*}$ and $v_{\mu g}^{q*}$ are taken from AC mains in dq variables.

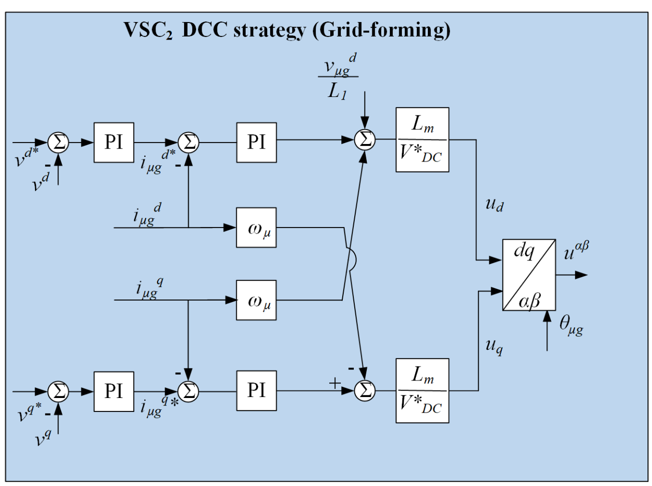

Figure 2.12. Control block diagram of the DCC strategy applied to the grid-forming.

The Figure 2.13 depicts the Bode diagram of the inner and outer loops transfer functions, accomplishing decoupled bandwidth criteria, by considering proportional and integral gains contained in Table 2.4.

Table 2.4. DCC VSC_2 Grid-forming converter parameters.

DCC VSC_2 grid-forming			
Parameter	**Value**	**Parameter**	**Value**
$k_{p\mu g}$	260	$k_{i\mu g}$	445
$k_{pVd,q}$	0.25	$k_{iVd,q}$	1.9

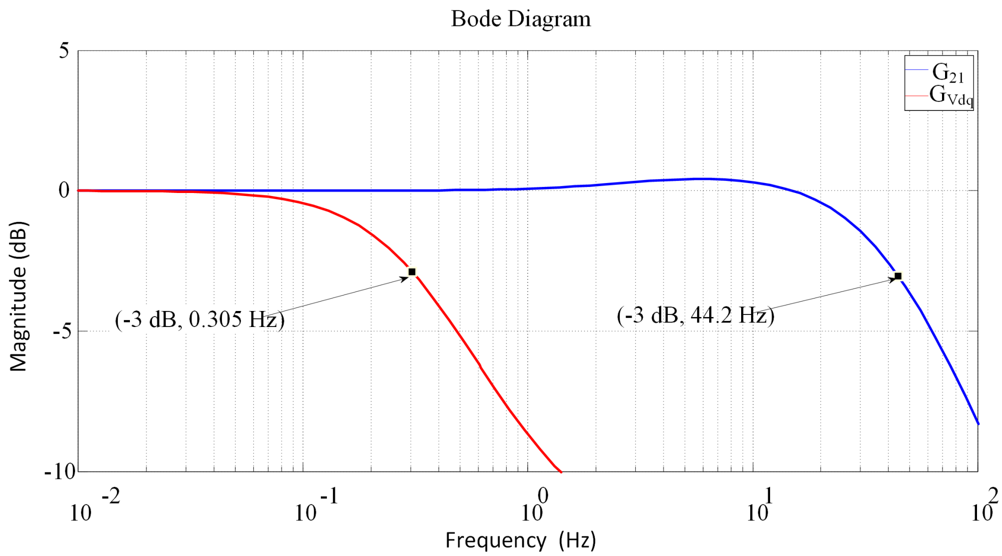

Figure 2.13. Bode diagram of the closed loop transfer functions for $v_{d,q}$ controllers.

2.1.2. Passivity based controllers for the grid-feeding converter

The Passivity Based Control (PBC) is a non-linear control strategy that looks for stabilize the system by energy balance using the properties of the systems that can be represented by Euler-Lagrange (EL) equations, where the main control objective is to achieve *stabilization by passivation* by using a storage function [44, 107].

To develop a well-designed PBC applied through the interconnection structure, it is important to make the assumptions such that the switching frequencies and sampling are sufficiently fast to approximate the average behavior by a smooth system [107], it is accomplished also in the system modeling considerations. From this mathematical model structure in the PBC, the model previously developed is considered in the following port-Hamiltonian form [73]:

$$\mathbf{M}\dot{x} + \mathbf{R}x + \mathbf{J}x = \varepsilon, \tag{2.13}$$

where $\mathbf{M}$ is the matrix with the energy storage elements with the restriction $\mathbf{M} > 0$, $\mathbf{R}$ is the damping matrix with the parasitic resistances and $\mathbf{R} = \mathbf{R}^T \geqslant 0$; $\mathbf{J}$ results in an skew-symmetric matrix with the interconnection structure with $\mathbf{J} = -\mathbf{J}^T$, and ε is the non controlled inputs vector [44].

By considering the mathematical model of the SPFB grid-feeding converter with LCL filter, the matrices in the interconnection structure are defined as follows:

$$\mathbf{M} = \begin{bmatrix} L_1 & 0 & 0 & 0 & 0 & 0 & 0 \\ 0 & L_1 & 0 & 0 & 0 & 0 & 0 \\ 0 & 0 & L_2 & 0 & 0 & 0 & 0 \\ 0 & 0 & 0 & L_2 & 0 & 0 & 0 \\ 0 & 0 & 0 & 0 & C_f & 0 & 0 \\ 0 & 0 & 0 & 0 & 0 & C_f & 0 \\ 0 & 0 & 0 & 0 & 0 & 0 & C_{DC} \end{bmatrix}, \tag{2.14}$$

$$\mathbf{R} = \begin{bmatrix} R_1 & 0 & 0 & 0 & 0 & 0 & 0 \\ 0 & R_1 & 0 & 0 & 0 & 0 & 0 \\ 0 & 0 & R_2 & 0 & 0 & 0 & 0 \\ 0 & 0 & 0 & R_2 & 0 & 0 & 0 \\ 0 & 0 & 0 & 0 & 0 & 0 & 0 \\ 0 & 0 & 0 & 0 & 0 & 0 & 0 \\ 0 & 0 & 0 & 0 & 0 & 0 & 0 \end{bmatrix}, \tag{2.15}$$

$$\mathbf{J} = \begin{bmatrix} 0 & -\omega L_1 & 0 & 0 & 1 & 0 & -u^d \\ \omega L_1 & 0 & 0 & 0 & 0 & 1 & -u^q \\ 0 & 0 & 0 & -\omega L_2 & -1 & 0 & 0 \\ 0 & 0 & \omega L_2 & 0 & 0 & -1 & 0 \\ -1 & 0 & 1 & 0 & 0 & -\omega C_f & 0 \\ 0 & -1 & 0 & 1 & \omega C_f & 0 & 0 \\ u^d & u^q & 0 & 0 & 0 & 0 & 0 \end{bmatrix}, \tag{2.16}$$

$$\varepsilon = \begin{bmatrix} 0 & 0 & V_{red} & V_{red} & 0 & 0 & i_B \end{bmatrix}^T, \tag{2.17}$$

$$x = \begin{bmatrix} i_1^d & i_1^q & i_2^d & i_2^q & v_{Cf}^d & v_{Cf}^q & V_{dc} \end{bmatrix}^T. \tag{2.18}$$

To derive the control strategy, a suitable steady state in the system of the Eq.(2.13) is given by any $x^* \epsilon \mathbb{R}^n$ that validates [108]:

$$\mathbf{M}\dot{X}^* + \mathbf{R}X^* + \mathbf{J}X^* + \mathbf{R_a}\mathbf{e} = \varepsilon, \tag{2.19}$$

where $\mathbf{X}^*$ is the vector with the reference variables, $\mathbf{R_a}$ is the selected damping, $\mathbf{e} = (x^* - x)$ is the error vector defined by $x^* = \begin{bmatrix} i_1^{d*} & i_1^{q*} & i_2^{d*} & i_2^{q*} & v_{Cf}^{d*} & v_{Cf}^{q*} & V_{dc}^* \end{bmatrix}^T$. This control strategy is given by the equations (2.20) and (2.21), and it is obtained from those Equations in the steady state system (2.19) which contains u^d and u^q, where k_1 and k_2 are the corresponding gains of the selected damping [103, 108].

$$u^d = \frac{1}{V_{dc}^*}\left[L_1 \dot{i}_1^{d*} + R_1 i_1^{d*} - \omega L_1 i_1^{q*} + v_{C_f}^{d*} + k_1\left(i_2^{d*} - i_2^d\right)\right], \tag{2.20}$$

$$u^q = \frac{1}{V_{dc}^*}\left[L_1 \dot{i}_1^{q*} + R_1 i_1^{q*} + \omega L_1 i_1^{d*} + v_{C_f}^{q*} + k_2\left(i_2^{q*} - i_2^q\right)\right]. \tag{2.21}$$

The Table 2.5 contains the values for k_1 and k_2 in the matrix damping.

Table 2.5. PBC Grid-feeding converter parameters.

PBC grid-feeding			
Parameter	**Value**	**Parameter**	**Value**
k_1	3	k_2	1.5

2.2. Simulation results

The simulation results and the validation of the control strategies applied to the inverters' detailed models are implemented via PSIM V9.1, in order to validate each control law in a C-code block, with the purpose of implement the same code in the control platform. The multiple scenarios are proposed to verify a suitable performance of the system in transient and steady state conditions; after that experimental results are obtained using a SPFB prototype. The grid-feeding and grid-forming converters are tested in multiple scenarios, where their rated capacity is assessed considering the following assumptions.

- The grid-feeding converters are supplied with an ideal DC source, as well as an ideal AC source with fixed value is considered with the purpose of assessing the performance of the control strategies avoiding any other system variation.
- It is considered a $2\,\Omega$ series resistor with the ideal DC source, to assess the performance of the control strategy with a non regulated voltage source neglecting harmonics content injected by the boost converter.
- The power is injected to AC through the PCC.

2.2.1. Performance of grid-feeding converter supplying active power to the PCC

Figure 2.14 and Table 2.6 contain the nominal parameters of the grid-feeding structure to validate the control strategies.

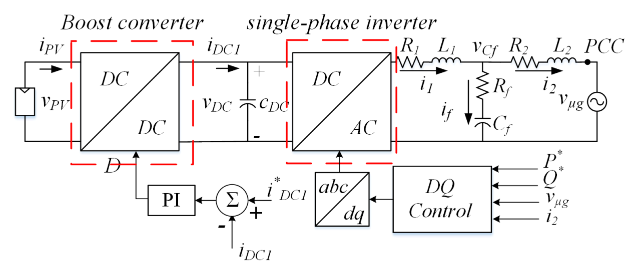

Figure 2.14. Schematic diagram of the PV Energy-based grid-feeding converter.

Table 2.6. Nominal MG System Parameters.

Parameter	Value	Parameter	Value
V_{DC}	250 V	f	60 Hz
$V_{\mu g}$	127 V_{rms}	f_{sw}	12.5 kHz
S	1000 VA	R_1	142 mΩ
L_1	3.03 mH	R_2	1.11 mΩ
C_f	6.88 μF	L_2	1.11 mH
R_g	142 mΩ	L_g	3.03 mH

To assess the active power supply capability of the grid-feeding converter at unity power factor, it is asked to inject the active power reference $P^* = 700$ W and reactive power reference of $Q^* = 0$ VAr with DCC and PBC strategies in the local control level. The grid-feeding power is injected to $v_{\mu g}$ taking into account this source has smooth variations leading to a fixed value of the MG voltage, to decouple de grid-feeding dynamics during the individual assessment of each control strategy.

Figure 2.15 depicts the transient response when at the time $t = 0.05\,s$ the grid-feeding starts to receive the active power reference $P^* = 700$ W, where the measured signals are the output current i_2 in Fig. 2.15 a), the output current in synchronous reference frame $i_{d,q}$ in Fig. 2.15 b) and the absolute error of the active and reactive power err_P and err_Q as corresponds.

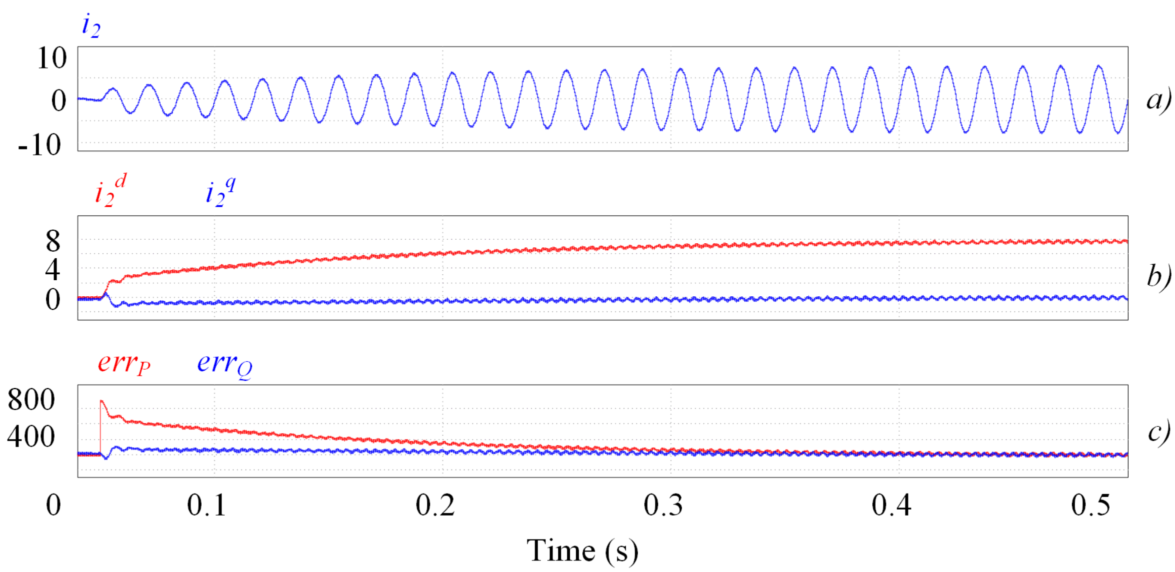

Figure 2.15. Transient response of the grid-feeding injecting 700 W to the grid with DCC strategy.

The Figure 2.16 depicts the transient response and the steady state conditions when the grid-feeding injects 700 W to AC mains with PBC strategy. It is possible to observe the PBC strategy is faster than the DCC to achieve the reference in steady state in these conditions, but PBC maintains an steady state error as it can be seen in Fig. 2.16 c) due to the DCC is capable to avoid this error taking advantage of the tracking capabilities of the PI structure. The Table 2.7 contains the settling time values for both control strategies, where the error signals in PBC in this scenario are due to v_{DC} is not regulated.

Table 2.7. Settling time for the grid-feeding injecting active power.

Parameter	Value	Parameter	Value
t_{ssDCC}	330 ms	t_{ssPBC}	22 ms

It is important to mention that the settling times shown in the different scenarios can be improved with the selection of the proportional and integral gains of the DCC strategy, but there is a compromise when the frequency response during tuning procedure has resonances at certain frequency values of its Bode plot, which it is not suitable for experimental purposes.

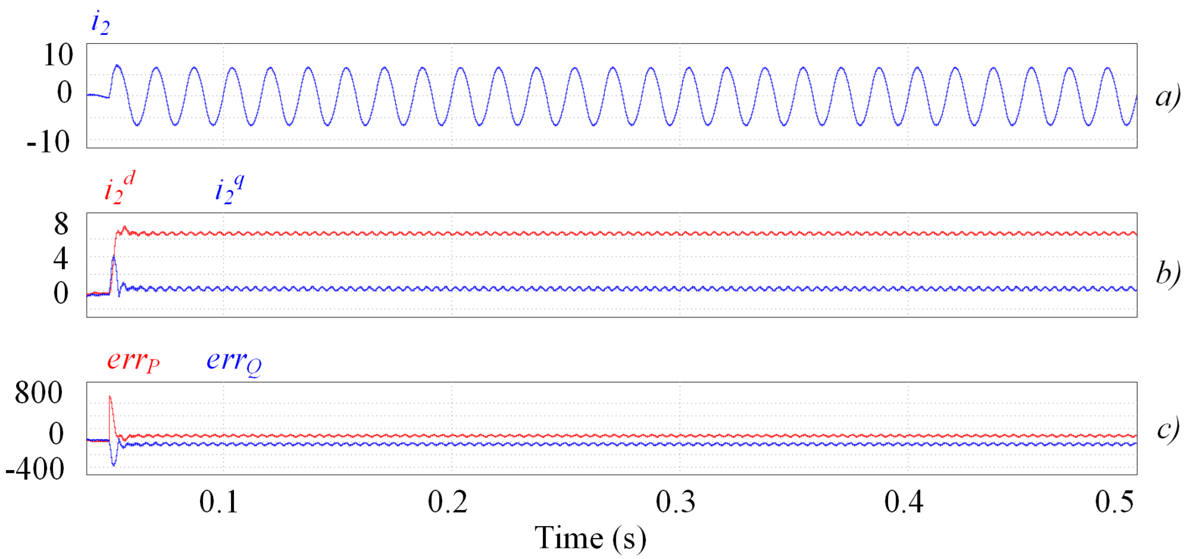

Figure 2.16. Transient response of the grid-feeding injecting 700 W to the grid with PBC strategy.

2.2.2. Performance of grid-feeding converter supplying active and reactive power to the PCC

This test assess the injection of active and reactive power capability of the grid-feeding converter with both control strategies. The Figure 2.17 depicts the transient response and the steady state conditions when the grid-feeding injects 700 W and 700 VAr to AC mains with DCC strategy and the Fig. 2.18 with PBC strategy; it is possible to observe PBC strategy is faster similar to the case when the grid-feeding injects only active power to the PCC.

The Table 2.8 contains the settling time values for both control strategies for this case.

Table 2.8. Settling time for the grid-feeding injecting active and reactive power.

Parameter	Value	Parameter	Value
t_{ssDCC}	459 ms	t_{ssPBC}	13 ms

2.2.3. Performance of Grid-feeding converter supplying active and consuming reactive power to the PCC

The injection capability of active power when the grid-feeding is consuming reactive power as inductive load is assessed as part of the extended functions, where the settling times of the transient response for both control strategies are contained in Table 2.9.

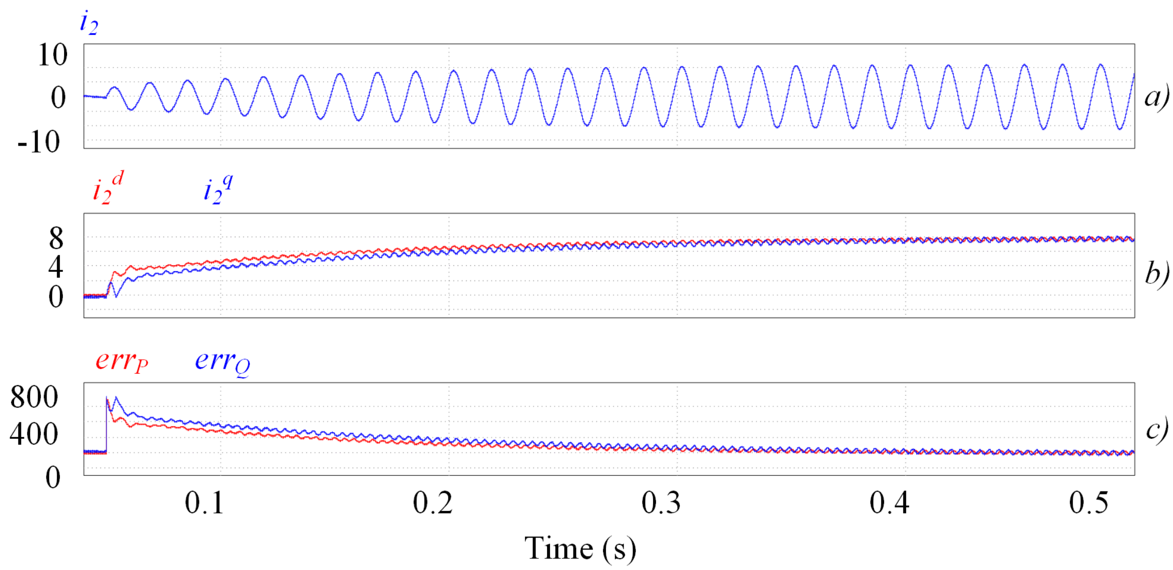

Figure 2.17. Transient response of the grid-feeding injecting 700 W and 700 VAr to the grid with DCC strategy.

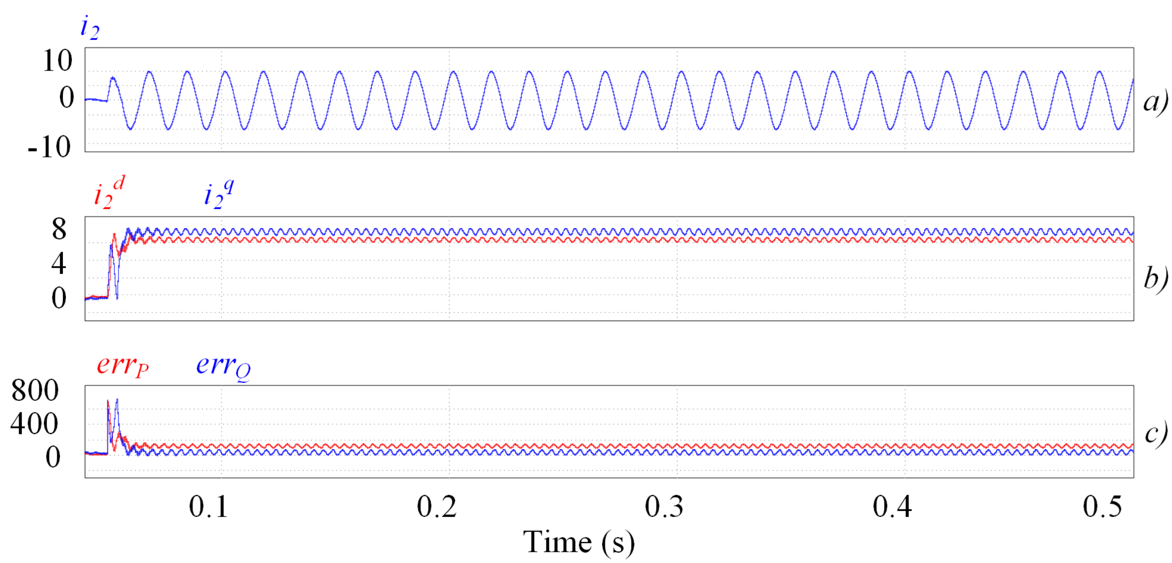

Figure 2.18. Transient response of the grid-feeding injecting 700 W and 700 VAr to the grid with PBC strategy.

Table 2.9. Settling time for the grid-feeding injecting active and reactive power.

Parameter	Value	Parameter	Value
t_{ssDCC}	490 ms	t_{ssPBC}	9.6 ms

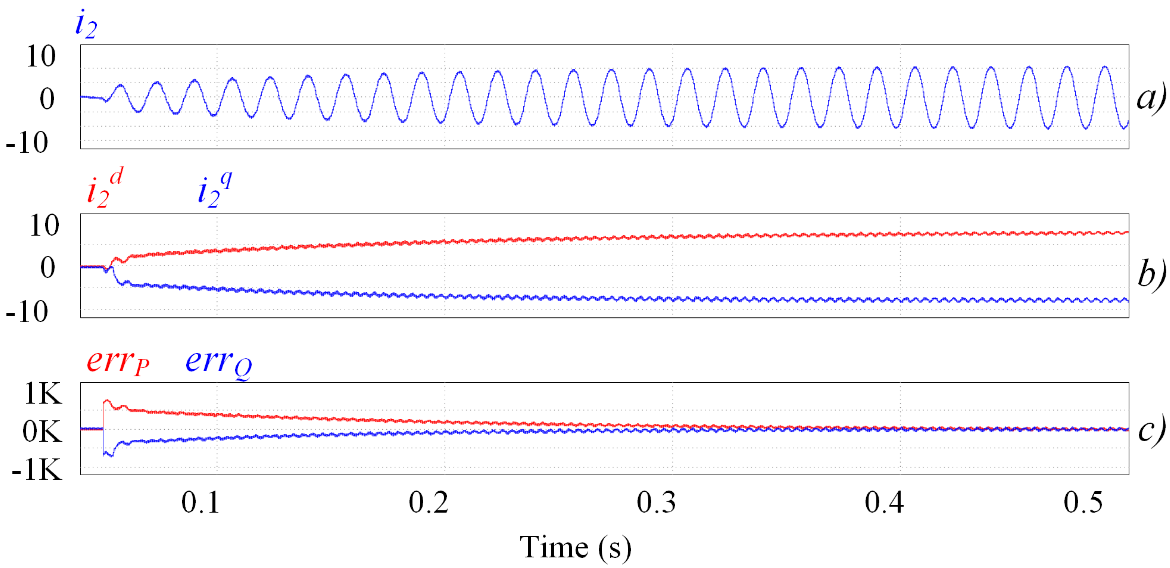

Figure 2.19. Transient response of the grid-feeding injecting 700 W and -700 VAr to the grid with DCC strategy.

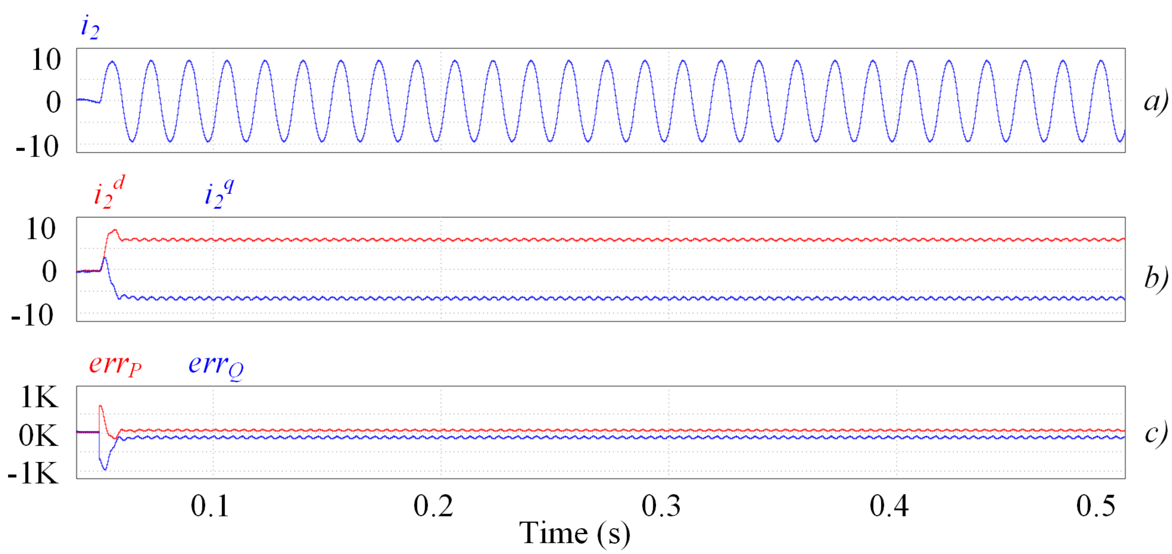

Figure 2.20. Transient response of the grid-feeding injecting 700 W and -700 VAr to the grid with PBC strategy.

2.2.4. Discussion

The tests previously carried out with DCC and PBC strategies shows correctly the active and reactive power regulation and injection capabilities for both control strategies. It is important to mention that PBC structure considered as a first approximation involves a steady state error which can affect the performance of the next control levels in the HCS structure, therefore it is another considered solution in the next sections. According to the tuning procedure it is possible to observe that there are not considerable overshoots during the transient response.

2.2.5. Performance of grid-forming converter regulating microgrid voltage $v_{\mu g}$

The grid-forming converter is controlled in closed loop to work as a voltage source with a desired amplitude and frequency and it is able to operate in islanding mode. To compare and validate the controller in simulation and experimentally, the test carried out takes into account the regulation of $v_{\mu g}$ which is implemented to the VSC_2 of the BTB converter, where the references $v^{d,q*}$ are related to the nominal value of the MG voltage and $0 \leq \theta_{\mu g} \leq 2\pi$ is a periodic signal.

Figure 2.21 and Table 2.10 contain the nominal parameters of the grid-forming structure to validate the control strategies.

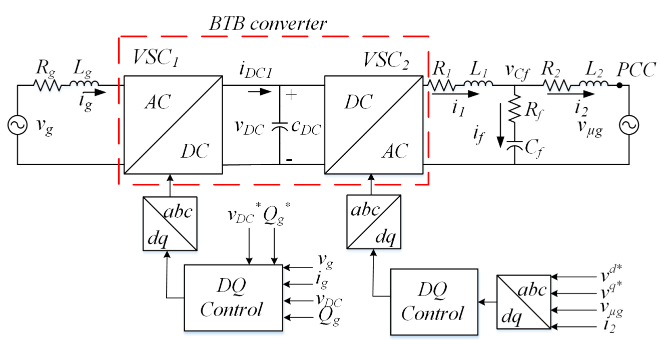

Figure 2.21. Schematic diagram of BTB converter working as grid-forming converter.

Table 2.10. Nominal MG System Parameters.

Parameter	Value	Parameter	Value
V_{DC}	250 V	f	60 Hz
V_{AC}	127 V_{rms}	f_{sw}	12.5 kHz
P	700 W	R_1	142 mΩ
Q	±700 VAr	R_2	1.11 mΩ
$V_{\mu g}$	127 V_{rms}	L_1	3.03 mH
C_f	6.88 μF	L_2	1.11 mH
R_g	142 mΩ	L_g	3.03 mH

Figure 2.22 shows the transient response of the grid-forming converter with DCC strategy implemented to achieve the references $v^d = 179$ and $v^q = 0$ which are equivalent

to $v_{\mu g} = 127\, V_{rms}$. It is also supplying power to a resistive load $R_L = 16.13\, \Omega$ consuming $P_L = 1000$ W. Although it is possible to observe that these tests have a slower response compared to the grid-feeding simulation results, owing to the low-bandwidth response made by the outer loops controllers after the suitable gains have been selected, this is desirable that this response be smooth avoiding high percentage overshoots when the MG voltage faces sudden disturbances, hence it is important to mention the controller is capable to achieve steady state conditions. It also allows to the grid-forming a suitable start-up to establish the voltage reference in the MG.

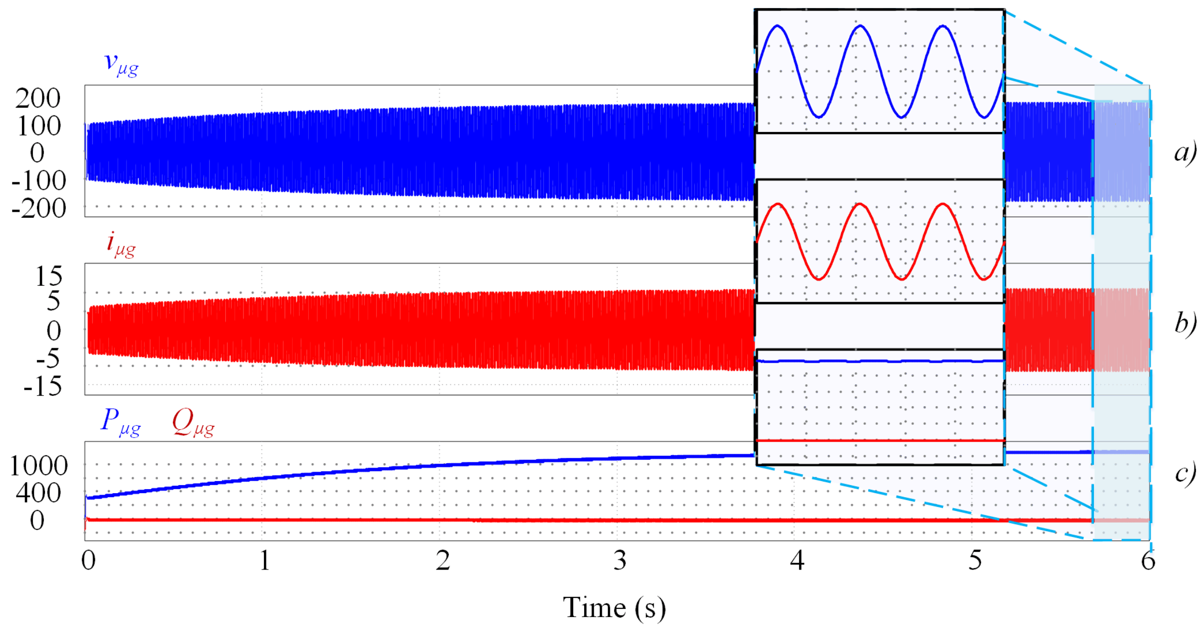

Figure 2.22. Grid-forming achieving steady state conditions to regulate the reference of $v_{\mu g}$ with DCC strategy.

2.3. Experimental results

The experimental validation of the control strategies is carried out with a SPFB converter working as grid-feeding converter connected to AC mains, as it is shown in the Figure 2.23, where the control strategy is implemented in a digital signal processor TMS320F28379D and for demonstration purposes the SPFB is supplied through a rectified and non-regulated DC bus v_{DC} and to connect it with AC mains an LCL filter with the parameters of the simulation is used. The capability of active and reactive power injection as well as their transient response are assessed with different scenarios where the total harmonic distortion of the current is also reported.

The signals measured are reported as follows: Ch1 is the AC mains voltage, Ch2 is the output current i_2, Ch3 is v_{DC} and the channel *Math* represents the active power calculation with Ch1 and Ch2. The settling time T_{ss} of each test is measured taking into account the transient response of i^d variable, when it achieves steady state conditions, and this signal is taken out from the DAC in the control platform TMS320F28379D.

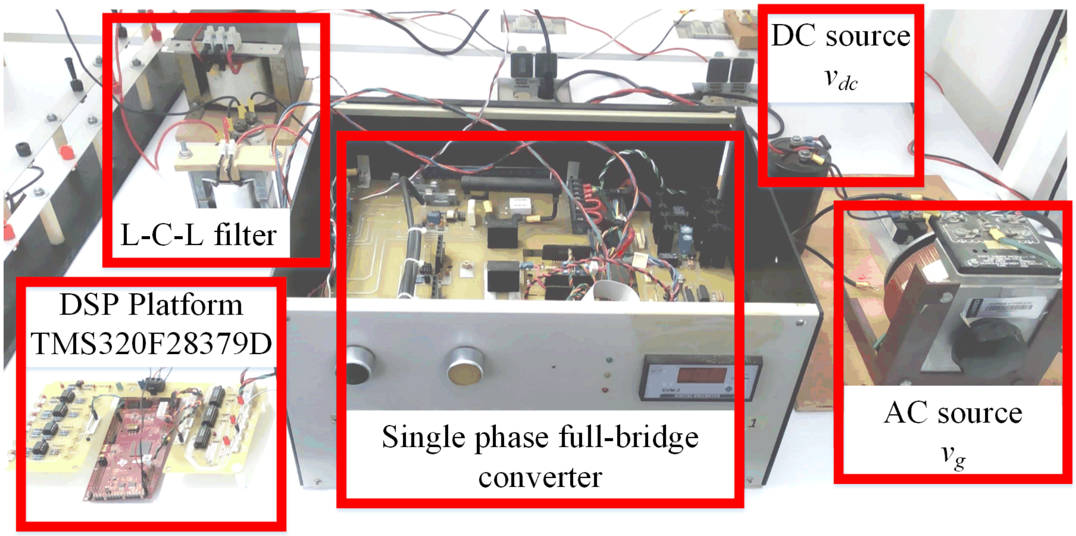

Figure 2.23. Experimental prototype of the Single-Phase Grid-feeding converter.

2.3.1. Grid-feeding converter injecting active power to AC mains

Table 2.11 contains the nominal values considered to inject active power at unity power factor.

Table 2.11. Nominal parameters.

P^*	Q^*	S	I_{rms}	V_g	V_{DC}
700 W	0 VAr	700 VA	5.38 A	130 V	250 V

The Figure 2.24 shows the transient response of the output current when there is a reference change in the active power P^* from 0 to 700 W with the DCC strategy as well as the Figure 2.25 shows the results obtained with PBC strategy. The settling time is measured taking as reference the signal of the current i^d from the DAC in the DSP platform in a second scope and its value is depicted in each Figure shown, where the settling time of DCC is 16 ms slower than PBC strategy. In both results the overshot percentage is negligible.

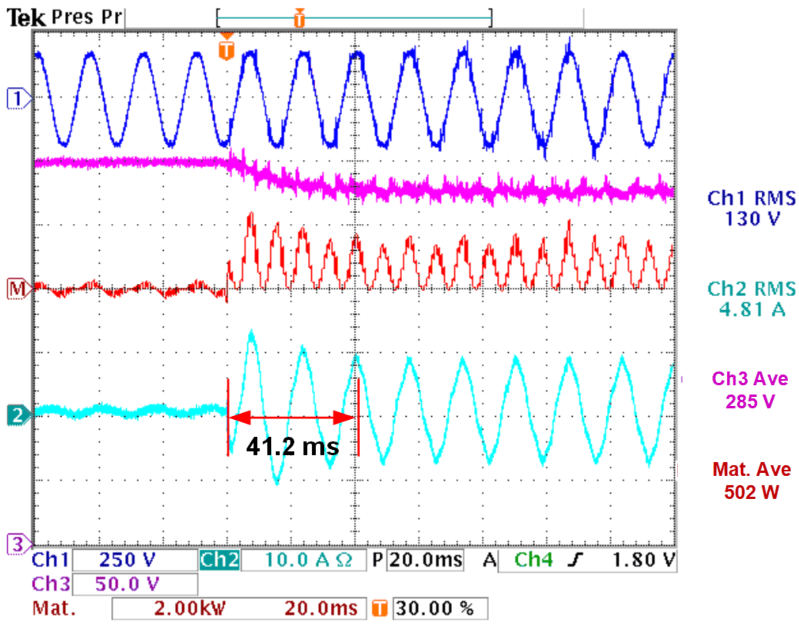

Figure 2.24. Experimental results of the Grid-feeding converter injecting active power with DCC.

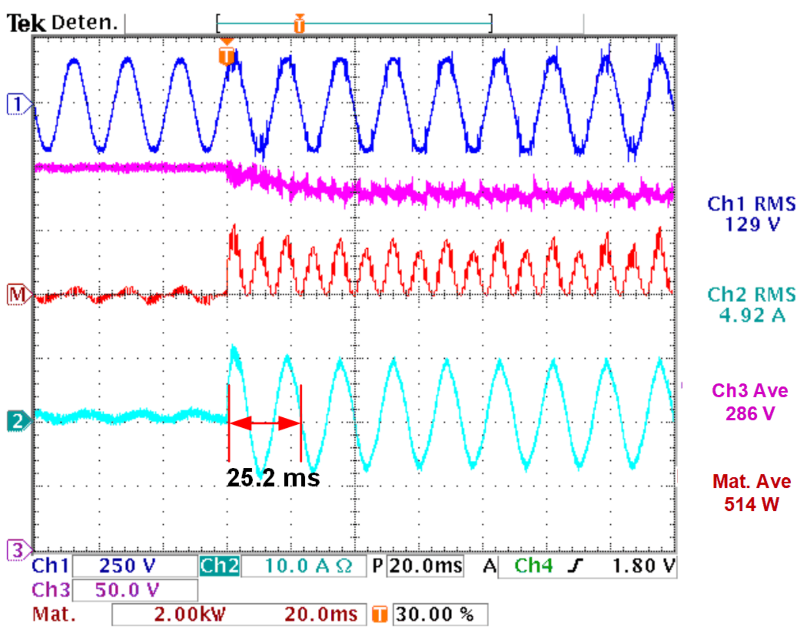

Figure 2.25. Experimental results of the Grid-feeding converter injecting active power with PBC.

2.3.2. Grid-feeding converter injecting active power to AC mains and consuming reactive power

The Table 2.12 contains the nominal values considered to inject active power and consuming reactive power with inductive load behavior.

Table 2.12. Nominal parameters.

P^*	Q^*	S	I_{rms}	V_g	V_{DC}
700 W	-700 VAr	990 VA	7.61 A	130 V	250 V

The Figure 2.26 shows the transient response of the output current when there is a reference change in the active power P^* from 0 to 700 W and from 0 to - 700 VAr in the reactive power Q^* with the DCC strategy, as well as the Figure 2.27 shows the results obtained with PBC strategy. It can be observed that in this case the settling time with DCC strategy is 10.8 ms slower than PBC strategy.

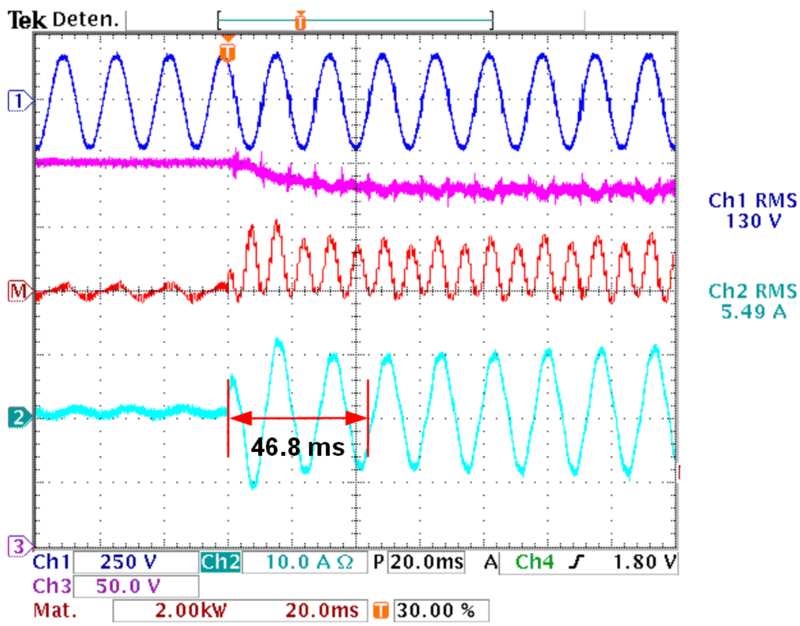

Figure 2.26. Experimental results of the Grid-feeding converter injecting active power and inductive load behavior with DCC.

2.3.3. Grid-feeding converter injecting active and reactive power to AC mains

The Table 2.13 contains the nominal values considered to inject active power and reactive power with capacitive load behavior.

Table 2.13. Nominal parameters.

P^*	Q^*	S	I_{rms}	V_g	V_{DC}
700 W	+700 VAr	990 VA	7.61 A	130 V	250 V

The Figure 2.28 shows the transient response of the output current when there is a reference change in the active power P^* from 0 to 700 W and from 0 to + 700 VAr in

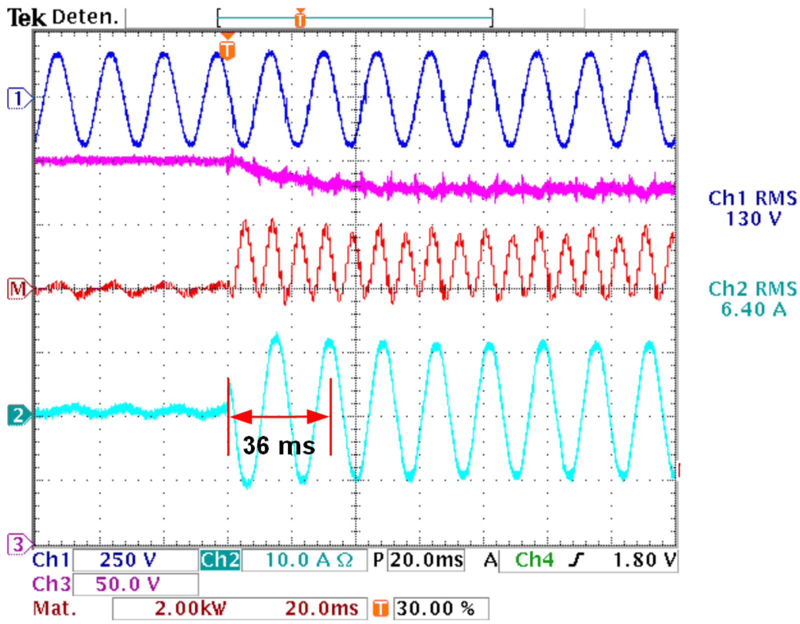

Figure 2.27. Experimental results of the Grid-feeding converter injecting active power and inductive load behavior with PBC.

the reactive power Q^* with the DCC strategy, as well as the Figure 2.29 shows the results obtained with PBC strategy. It can be observed that in this case the settling time with DCC strategy is 6.4 ms slower than PBC strategy.

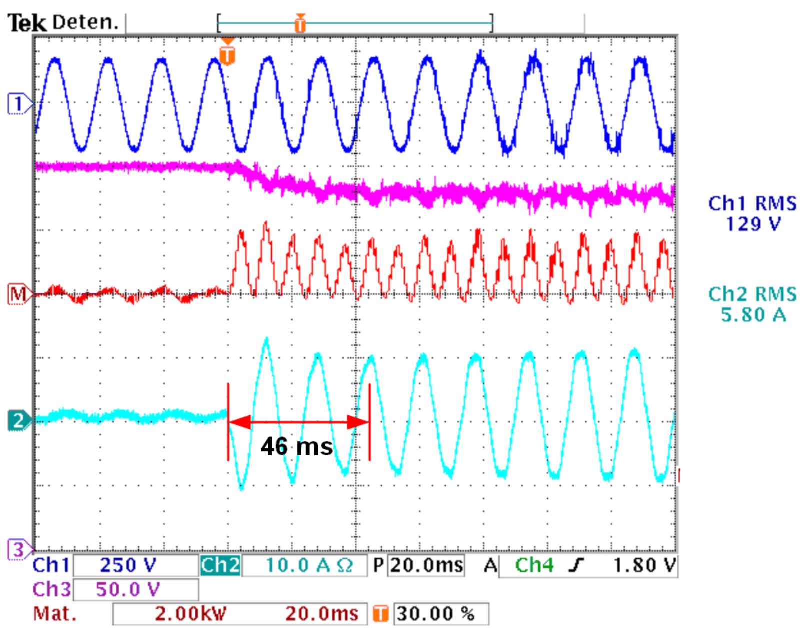

Figure 2.28. Experimental results of the Grid-feeding converter injecting active power and capacitive load behavior with DCC.

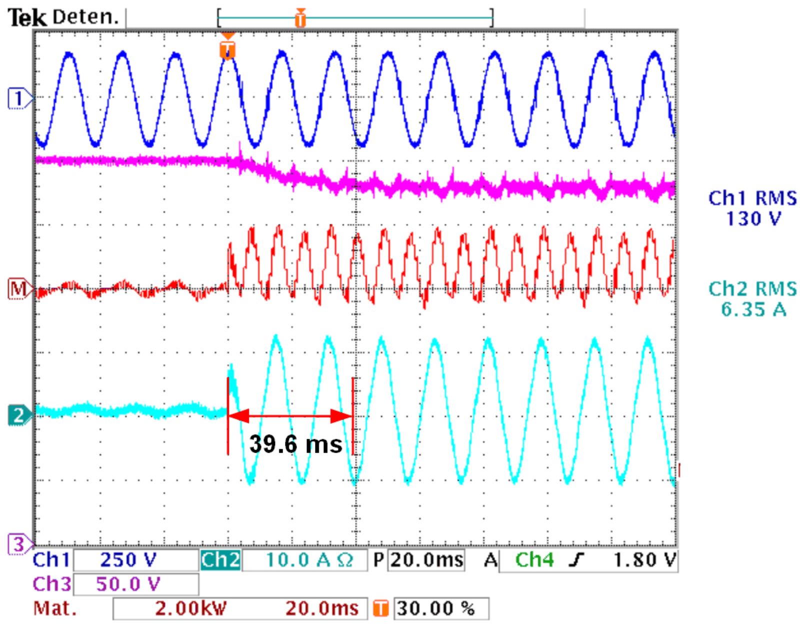

Figure 2.29. Experimental results of the Grid-feeding converter injecting active power and capacitive load behavior with PBC.

2.3.4. Power quality performance

The performance of the control strategies is also assessed with the Total Harmonic Distortion (THD) measurement of the output current in different scenarios of load consumption, where the values are contained in Table 2.14.

Table 2.14. THD measurements.

S (VA)	P (W)	Q (VAr)	I_{rms} (A)	V_g (V)	THD_I (%) DCC	THD_I (%) PBC
700	700	0	5.38	130	6.8	7.39
990	700	700	7.61	130	5.11	6.23
990	700	-700	7.61	130	6.43	5.59
300	300	0	2.3	130	16.1	15.78
424	300	300	3.26	130	11.77	14.56
424	300	-300	3.26	130	13.31	13.03
200	200	0	1.53	130	21.7	20.57
282	200	200	2.16	130	16.72	21.13
282	200	-200	2.16	130	19.28	17.88

It is possible to observe that in terms of THD_I, the results obtained are similar at nominal values in both control strategies, where the distortion increases as long as the power reference decreases due to the load demanded does not affect directly the harmonic components of the current. Another factor to this phenomenon is related to the current sensor performance when the current measurement is lower, due to the radiated and conducted noise impacts in the size of the signal measured.

2.3.5. Grid-forming converter regulating AC voltage of the microgrid

The Figure 2.30 depicts the transient response of the grid-forming when it is asked to regulate de voltage references $v^{d,q*}$ with a frequency $f_{\mu g} = 60\,Hz$ to establish an AC bus in the MG $v_{\mu g} = 127\,V_{rms}$. DCC strategy is used for this purpose and as it was previously mentioned, it is possible to observe the control strategy gives the capability to the grid-forming to correctly regulate the voltages references in a start-up scenario. Due to the above mentioned the large settling time is not a continuous operation when the MG is normally working.

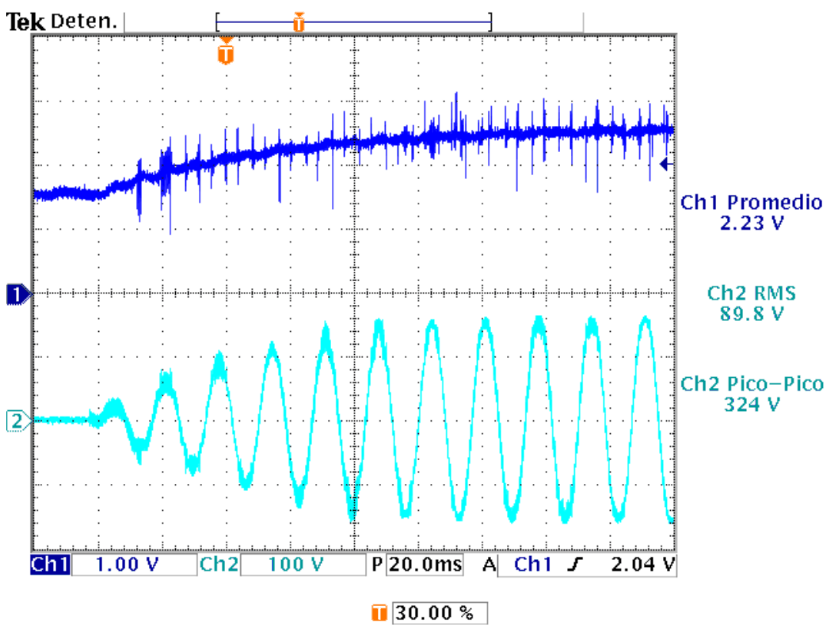

Figure 2.30. Transient response of the grid-forming with DCC strategy.

2.3.6. Discussion

The control strategies implemented at the primary level of the hierarchical control structure provided regulation of the necessary parameters accomplishing voltage and frequency regulation in case the converter performs grid-forming tasks or active and reactive power regulation in case the converter performs grid-feeding tasks, hence this control stage results capable to receive the references generated by the next control stage, and achieved the load requirements of the system.

Passivity-based controller applied to the grid-feeding structure obtained a suitable performance in the transient response, where mainly the settling time observed in simulation is considerably faster than decoupled current control in these particular conditions owing to the corresponding gains are selected for implementation purposes, where it is also observed experimentally that the settling time is 25% faster than DCC control. The total harmonic distortion of the current at rated load given by each control strategy at the primary level does not have a big difference between each other at the tested scenarios, hence the known drawbacks as parameter dependency of decoupled current control could be considered for the selection of the control strategy in contrast with passivity based controller.

The above tests are carried out to particularly consider the response of each control strategy in these conditions to be applied in both grid-feeding and grid-forming converters, taking into account the known advantages of PBC such as the global stability of the system and its robustness with parametric uncertainty [109, 110].

CHAPTER 3

ANALYSIS AND SYNTHESIS OF THE OPTIMAL MICROGRID OPERATION

The suitable operation of a MG system involves accomplishing certain restrictions while the problem of satisfying and supply the power required by the loads is solved, where optimization procedures improves the achievement of such results considering the given conditions. In general terms the main goal of taking decisions in the optimization either minimize the effort required or to maximize the desired benefit; hence the optimization is defined as the procedure to find the maximum or minimum value of the problem expressed in function of decision variables [111].

In terms of MG operation, the optimal solutions are given to improve the system performance in different aspects; some of the reported results optimized solve issues regarding to sizing elements or parameters of the system, where some research works report optimization of portfolio, allocation, and dispatch of RE-based DGU using Mixed Integer Linear Programming methods to avoid transformer overloads [112]. Others solutions improve controllers performance through suitable design, where multi-objective proposals with hybrid ESS and wind turbines are used to set control values and reducing operation cost [74], as well as several studies report Particle Swarm Optimization (PSO) technique which is used to obtain the values of droop coefficients in [113], improving system efficiency and power quality performance, maintaining voltage THD within constraints, as well as losses minimizing. Energy management and optimal dispatch is another solution, such as the concept of trading among MG with shared ESS has been proven as one method to improve the renewable energy consumption [75].

In this research work the optimal solutions algorithms are explored as an energy management method to improve the energy usage in order to attack interoperability issues, minimize losses, cost and non required interactions as high penetration issues, such as voltage and frequency variations, as well as growth system reliability through the controlled power delivery to the load and regulating the power exchanged with AC mains.

As it is previously mentioned, the third level in the HCS is mainly in charge of carrying out the optimal operation of the MG in grid-connected mode and islanded mode, as it is shown in Figure 3.1, in which is the focus of this chapter.

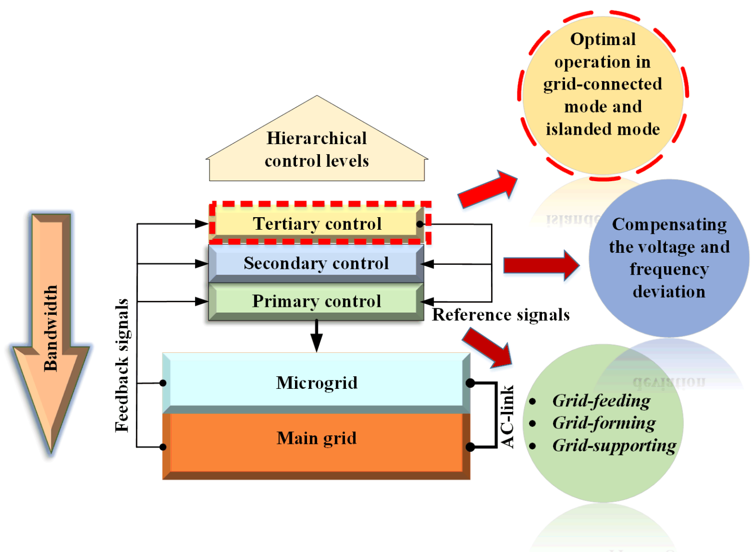

Figure 3.1. Hierarchical Control Structure.

3.1. Optimization of the economic operation problem

The formulation of energy management optimal problem considers a power sharing solution [114]; it is established an N-parallel connected grid-feedings as DGU system in radial array with the load as it is shown in Fig. 3.2. The electric load P_L is connected to the AC mains and the power delivered by each DGU is injected to supply the load.

The cost rate F_i in dollars per hour ($\$/h$) is defined by Eq.(3.1), and it is the input of the connected DGU, also it is in function of the capital cost K ($\$/h$) and the operating cost $h(P)$ as a function of the output production amount P_i (W), being this the electrical power generated, and both are related by the cost per unit of generated energy C_p ($\$/Wh$) [115, 116]. Although this representation is not directly related to PV plants, as

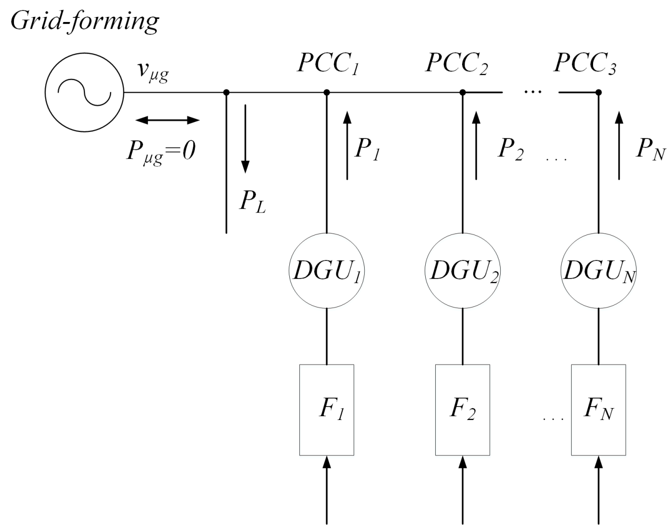

Figure 3.2. N DGUs injecting power to a single load P_L.

first approximation it meets the objective of giving a cost in function of the required power for each DGU connected to the MG, and as it is related to a real dispatch problem, the solution procedure can be adapted to other cost functions, furthermore the solution of the MG electrical system is carried out separately from the optimization problem and it considers PV panels as RES.

$$F_i(P_i) = K_i + h(P_i). \tag{3.1}$$

The sub-index i is the $i-th$ DGU; the power supplied to the MG by each DGU is measured at the PCC of each one. In this case the power losses are not considered. Due to the excess of power injected from the PV systems to AC mains involves high penetration levels, the MG scenario considers to deliver only the power demanded by the connected load.

The objective function of the optimization problem is the total generation cost of the system represented as:

$$F_T = F_1 + F_2 + ... + F_N = \sum_{i=1}^{N} F_i(P_i). \tag{3.2}$$

To satisfy the load demanded, the main constraint of this system is that the DGUs must inject only the active power enough to supply the electric load, that is:

$$\phi = P_L - \sum_{i=1}^{N} P_i = 0. \tag{3.3}$$

Therefore, the optimization problem is to minimize the objective function given by (3.2) and defined as:

$$Min\left(F_T = F_1 + F_2 + ... + F_N = \sum_{i=1}^{N} F_i(P_i)\right), \tag{3.4}$$

subject to:

$$\sum_{i=1}^{N} P_i = P_L. \tag{3.5}$$

3.2. Optimization by gradient method

The reduced Gradient Method is considered to incorporate the previous constraint to the optimization problem, where the power losses in the line impedance are neglected, and the following Lagrange Function is used [115, 116]:

$$\mathcal{L} = F_T + \lambda\phi, \tag{3.6}$$

where λ ($\$/Wh$) is known as Lagrange multiplier. To find an extreme value of Eq. (3.6), the necessary condition is achieved when it sets the first derivative of the Lagrange function with respect each independent variable equal to 0 and it is represented as follows:

$$\frac{\partial \mathcal{L}}{\partial P_i} = \frac{dF_i(P_i)}{dP_i} - \lambda = 0. \tag{3.7}$$

To apply the Eq.(3.7) criteria to the DGUs connected to the MG system as grid-feeding converters, Eq.(3.6) becomes:

$$\mathcal{L}(F_1, F_2, ..., F_N, \lambda) = \sum_{i=1}^{N} F_i(P_i) + \lambda(P_L - \sum_{i=1}^{N} P_i). \tag{3.8}$$

The cost rates of each DGU in the MG system are chosen as typically second-degree cost functions [116], given by:

$$F_1(P_1) = K_1 + C_1 P_1 + C_2 P_1^2, \tag{3.9}$$

$$F_2(P_2) = K_2 + C_3 P_2 + C_4 P_2^2, \tag{3.10}$$

$$F_N(P_N) = K_N + C_{2N-1} P_N + C_{2N} P_N^2, \tag{3.11}$$

where $P_{1,2,...,N}$ are the active power generated of each DGU.

Thus the set of equations derived from apply Eq.(3.7) to Eq.(3.8) is given by:

$$C_1 + C_2 P_1 - \lambda = 0, \tag{3.12}$$

$$C_3 + C_4 P_2 - \lambda = 0, \tag{3.13}$$

$$C_{2N-1} + C_{2N} P_N - \lambda = 0, \tag{3.14}$$

$$\tag{3.15}$$

and Eq.(3.3) results:

$$P_1 + P_2 + ... + P_N = P_L. \tag{3.16}$$

To find the active power references that are considered as inputs at the local controllers of the grid-feedings, the set of linear equations (3.12)-(3.16) with unknown variables ($P_{1,2,..,N}$ and λ) is solved through conventional methods.

The set of functions as first approximation for the cost rate of each DGU in the MG system defined in chapter 1, where N=3 DGUs and the equations are defined by:

$$F_1(P_1) = 561 + 7.92 P_1 + 0.001562 P_1^2 \, \$/h, \tag{3.17}$$

$$F_2(P_2) = 310 + 7.85 P_2 + 0.00194 P_2^2 \, \$/h, \tag{3.18}$$

$$F_3(P_3) = 78 + 7.97 P_3 + 0.00482 P_3^2 \, \$/h, \tag{3.19}$$

where P_i is the output active power of DGUs, and the coefficients are considered theoretically from academic equations with the purpose of establishing a common quadratic function between the generation cost and the amount of power generated, that reflects the increase of cost as long as the demanded load increase. Being that the capital cost K ($\$/h$) and the operating cost $h(P)$ as a function of P_i (W),and both are related by the cost per unit generated energy C_p ($\$/Wh$), as mentioned in Eq.(3.1) [115, 116]. It is important to mention that the coefficients are selected as example with the purpose of including the cost rate functions in the solution of the optimization problem, owing to the need of developing the procedure to carry out the optimal operation, where the particular case for the cost rate functions related to PV systems is not addressed.

By considering the DGUs in the MG system previously defined, where $N = 3$ and $i = \{1, 2, 3\}$, the first constraint is to accomplish the objective of satisfy the total power demanded by a connected load P_L to the MG with the output power of the DGUs at the minimum cost possible. This is taken from Eq. (3.16) and defined for $P_L = 850$ W as:

$$P_1 + P_2 + P_3 = 850 \, W. \tag{3.20}$$

The solution for obtaining the optimal values for (3.2) and constrains (3.3) is shown in Table 3.1, where Lagrange multiplier is part of the solution with $\lambda = 9.148\$/Wh$.

Table 3.1. Optimal Power Sharing solution.

Parameter	**Value**	**Parameter**	**Value**
P_1^*	393.2 W	P_2^*	334.6 W
P_3^*	122.2 W	F_T	8,194

3.3. Optimization by linear programming method

Linear Programming Method (LP) is well known by its ability to manage constraints, such as equality constraints and inequality constraints, owing to the Gradient Method requires for combining iterative procedures to find the value of the Lagrange multipliers λ that allows convergence to the optimal solution into the feasible region, which makes it complex to solve owing to the necessity to observe not allowed operating zones [116, 117]. LP is capable to solve linear problems or non-linear problems through linearization procedures. By considering the set of equations for the cost rate quadratic functions, to apply LP method it is necessary to linearize the system of equations using a linear equivalent representation, as shown in Figure 3.3 [116, 118].

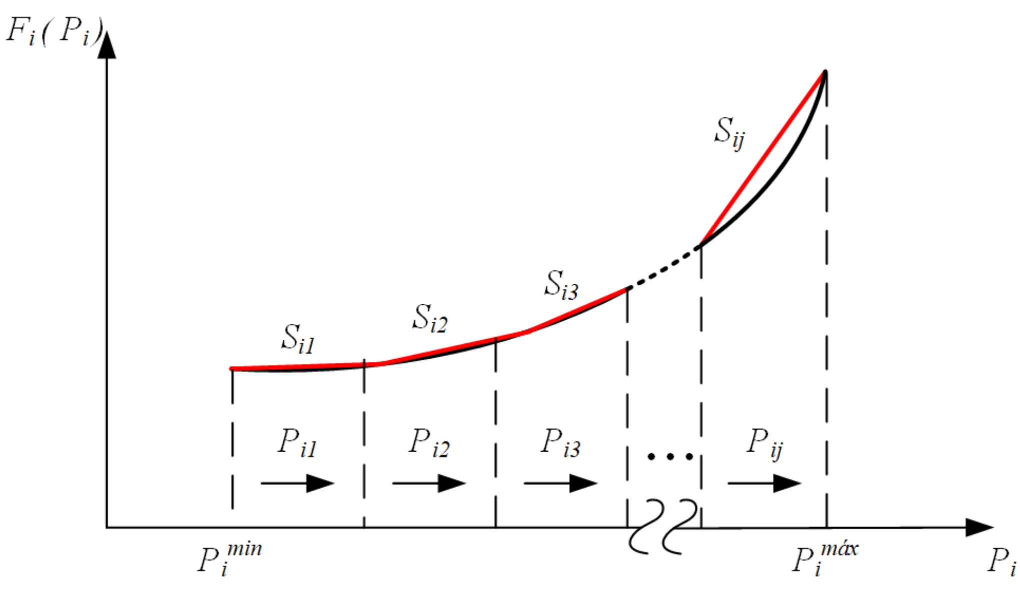

Figure 3.3. Non-linear function piecewise approximation.

The new added variables are related to a new slope S_{i1}, S_{i2} until S_{ij}, where $S_{i1} < S_{i2} < S_{i3} < S_{ij}$. Hence, each cost function obtains the form of equation (3.21).

$$F_i(P_i) = F_i(P_i^{min}) + S_{i1}P_{i1} + S_{i2}P_{i2} + S_{i3}P_{i3} + ... + S_{ij}P_{ij}, \tag{3.21}$$

where

$$0 \leq P_{ij} \leq P_{ij}^{max} \ for \ j = 1, 2, 3, ..., M, \tag{3.22}$$

and each slope is computed as

$$S_{ij} = \frac{F_i(P_{ij+1}) - F_i(P_{ij})}{(P_{ij+1}) - (P_{ij})}. \tag{3.23}$$

Therefore, the optimization by LP method for economic dispatch problem is defined as follows:

$$Min(\sum_{i=1}^{N}(F_i(P_i^{min}) + \sum_{j=1}^{M} S_{ij}P_{ij})), \tag{3.24}$$

subject to:

$$\sum_{i=1}^{N} P_i = P_L, \tag{3.25}$$

$$0 \leq P_{ij} \leq P_{ij}^{max} \ \ \forall i = 1, ..., N, \ and \ j = 1, ..., M, \tag{3.26}$$

and finally

$$P_i = P_i^{min} + \sum_{j=1}^{M} P_{ij} \, \forall i = 1...N. \tag{3.27}$$

To apply LP method in the MG system, the cost functions of the DGUs are the set of equations (3.28)-(3.30) used in Gradient Method, where $i \epsilon \{1, 2, 3\}$.

$$F_1(P_1) = 561 + 7.92P_1 + 0.001562P_1^2 \,\$/h, \tag{3.28}$$
$$F_2(P_2) = 310 + 7.85P_1 + 0.00194P_2^2 \,\$/h, \tag{3.29}$$
$$F_3(P_3) = 78 + 7.97P_1 + 0.00482P_3^2 \,\$/h. \tag{3.30}$$

In order to test different maximum active power availabilities of each DGU connected in the MG, the following active power limits for the grid-feedings are defined as restrictions of the optimization problem, where a minimum value is considered due to the need of maintaining the three grid-feedings operating, in which the cost rate functions are included in the optimization problem to contribute on the load satisfying.

$$\begin{aligned} 150 \leq \; & P_1 \leq 600, \\ 100 \leq \; & P_2 \leq 400, \\ 50 \leq \; & P_3 \leq 200. \end{aligned} \tag{3.31}$$

The optimization problem defined for LP method is:

$$Min\left(C^t x\right), \tag{3.32}$$

subject to

$$Ax \leq b, \tag{3.33}$$
$$x \geq 0, \tag{3.34}$$
$$x \,\epsilon\, R^n, \tag{3.35}$$

where x is an n-dimensional vector, C^t is the vector with the cost coefficients of the objective function, A is the matrix of constraints coefficients, b is the vector with the corresponding terms of the right side of the equations given by the constraints. By defining the optimization problem for the MG system previously established in chapter 1, with $N = 3$ DGUs, the set of segments used for the piecewise function is defined for $M = 3$

because there is no significant difference as the number of segments increases, according to [116]. Hence, from the set of equations (3.28)-(3.30) and by replacing the definition given by equation (3.21), the resulting cost function of the optimization problem is:

$$\begin{aligned} F_T(P) = 1.7841 + 8.468P_{11} + 8.7786P_{12} + 9.404P_{13}, \\ +1.1144 + 8.432P_{21} + 8.91733P_{22} + 9.304P_{23}, \\ +0.4885 + 8.694P_{31} + 9.176P_{32} + 9.656P_{33}. \end{aligned} \tag{3.36}$$

By considering the linear equivalent representation, where the vector x is as bellow.

$$x = \left[\begin{array}{ccccccccc} P_{11} & P_{12} & P_{13} & P_{21} & P_{22} & P_{23} & P_{31} & P_{32} & P_{33} \end{array} \right]^T. \tag{3.37}$$

Hence, the restrictions in the set of equations (3.31) become in the following equivalent set of restrictions:

$$P_{11} \leq 150;\ -P_{11} \leq 0;\ P_{12} \leq 150;\ -P_{12} \leq 0;\ P_{13} \leq 150;\ -P_{13} \leq 0, \tag{3.38}$$

$$P_{21} \leq 100;\ -P_{21} \leq 0;\ P_{22} \leq 100;\ -P_{22} \leq 0;\ P_{23} \leq 100;\ -P_{23} \leq 0, \tag{3.39}$$

$$P_{31} \leq 50;\ -P_{31} \leq 0;\ P_{32} \leq 50;\ -P_{32} \leq 0;\ P_{33} \leq 50;\ -P_{23} \leq 0. \tag{3.40}$$

By applying the equation (3.25) to equation (3.27), results in the following expression for the equality restriction in equation (3.20).

$$P_{11} + P_{12} + P_{13} + P_{21} + P_{22} + P_{23} + P_{31} + P_{32} + P_{33} = 550. \tag{3.41}$$

Matrix $A \epsilon R^{mxn}$ and vector $b \epsilon R^m$ are defined by equations (3.43), where result in $m = 19$ y $n = 9$; the last row of A and the last element of b correspond to the constraint of equation (3.41), and defining in terms of each value P_{ij} according to equations (3.38)-(3.40).

To assess the capability of the algorithm to solve the optimization problem with constraints of active power, the MATLAB-Simulink function *linprog* is used, which solves linear programming problems by finding the minimum for the defined equations (3.32)-(3.33) specified as follows [119].

$$\min_x f^T x \text{ such that } \begin{cases} A \cdot x \leq b, \\ Aeq \cdot x = beq, \\ lb \leq x \leq ub. \end{cases} \tag{3.42}$$

where A and b have been previously defined, lb and ub are the upper and lower boundaries of the restrictions, and Aeq and beq are given by empty matrices because there are only inequality constraints.

The solution is listed in the Table 3.2, where the optimal values are within the feasible region established by the constraints [116].

$$A = \begin{pmatrix} 1 & 0 & 0 & 0 & 0 & 0 & 0 & 0 & 0 \\ -1 & 0 & 0 & 0 & 0 & 0 & 0 & 0 & 0 \\ 0 & 1 & 0 & 0 & 0 & 0 & 0 & 0 & 0 \\ 0 & -1 & 0 & 0 & 0 & 0 & 0 & 0 & 0 \\ 0 & 0 & 1 & 0 & 0 & 0 & 0 & 0 & 0 \\ 0 & 0 & -1 & 0 & 0 & 0 & 0 & 0 & 0 \\ 0 & 0 & 0 & 1 & 0 & 0 & 0 & 0 & 0 \\ 0 & 0 & 0 & -1 & 0 & 0 & 0 & 0 & 0 \\ 0 & 0 & 0 & 0 & 1 & 0 & 0 & 0 & 0 \\ 0 & 0 & 0 & 0 & -1 & 0 & 0 & 0 & 0 \\ 0 & 0 & 0 & 0 & 0 & 1 & 0 & 0 & 0 \\ 0 & 0 & 0 & 0 & 0 & -1 & 0 & 0 & 0 \\ 0 & 0 & 0 & 0 & 0 & 0 & 1 & 0 & 0 \\ 0 & 0 & 0 & 0 & 0 & 0 & -1 & 0 & 0 \\ 0 & 0 & 0 & 0 & 0 & 0 & 0 & 1 & 0 \\ 0 & 0 & 0 & 0 & 0 & 0 & 0 & -1 & 0 \\ 0 & 0 & 0 & 0 & 0 & 0 & 0 & 0 & 1 \\ 0 & 0 & 0 & 0 & 0 & 0 & 0 & 0 & -1 \\ 1 & 1 & 1 & 1 & 1 & 1 & 1 & 1 & 1 \end{pmatrix} ; b = \begin{pmatrix} 150 \\ 0 \\ 150 \\ 0 \\ 150 \\ 0 \\ 100 \\ 0 \\ 100 \\ 0 \\ 100 \\ 0 \\ 50 \\ 0 \\ 50 \\ 0 \\ 50 \\ 0 \\ 550 \end{pmatrix}. \tag{3.43}$$

Table 3.2. Optimal solution for the three grid-feedings MG system.

Parameter	**Value**	**Parameter**	**Value**
P_1	450 W	P_2	250 W
P_3	150 W	F_T	8,217 \$/h

It can be observed that the solution obtained by using LP method corresponds to integer values due to the simplex method used in MATLAB, where the algorithm looks for the optimum value at the edges of the feasible region [116, 119].

3.4. Particle swarm optimization

Due to the optimal design problems mainly deal with a mix of discrete and continuous variables, as long as discontinuous and nonconvex spaces, genetic algorithms as PSO are within the methods with more flexible applications as multi-objective optimization, stochastic programming and combinatorial optimization problems, presenting a low computational cost and they are suitable to find the optimal solution with lower error percentage [120, 121]. The PSO method allows to improve the algorithm performance in terms of memory and velocity, due to the solution process involves iterations with simple operations, and as another outstanding advantage is the need of the final value of the objective function to apply the algorithm, hence it is not essential a specific type of cost function. Its solution method searches for optimal point within a set of candidate solutions with random locations in an n-dimensional space, as long as the limits and tolerance selected are achieved and the process converge to the optimum solution.

Table 3.3 lists the main advantages and weaknesses of using the PSO algorithm for obtaining the optimal solution applied to energy management optimization [61, 111, 121].

Table 3.3. PSO characteristics and applications.

Advantages
• Does not require function derivatives • Require only the function value and not system details • Handles mixed continuous and discrete variables problems • Low computational burden owing its basic mathematical operations • Multi-objective optimization • Combinatorial optimization problems • Accurate and fast convergence • Parameters relatively easy for tuning
Disadvantages
• Algorithm developed for a specific problem • Depending on the problem may be trapping into local optimal • Tends to wander and slow down as it approaches an optimum

3.4.1. PSO algorithm

The design of the solution method of the optimization problem is carried out through the basic rules and components of the PSO algorithm, where there are established definitions as follows [120, 122]:

Particle, $p_j(i)$

It is an m-dimensional vector representing the candidate solution and its optimal parameters, where the position of the jth particle in the ith iteration is described as $X_j(i) = [x_{j,1}(i), ..., x_{j,m}(i)]$.

Population, $pop(i)$

It is the set of particles in the ith iteration, described by $pop(i) = [X_1(i), ..., X_n(i)]$, where the swarm is the random moving particles that converge to the best position.

Particle velocity, $V_j(i)$

It represents the m-dimensional vector of the rate of change in the particles, $V_j(i) = [v_{j,1}(i), ..., v_{j,m}(i)]$.

Historical best value, $p_{best(i)}$

It contains the coordinates of jth particle in the current iteration with the highest value of the objective function, (denoted as *fitness* in genetic algorithms) $f(p_j(i))$ in all previous iterations.

Global best value, G_{best}

It contains the highest value of the objective function in all the previous iterations by any of the N_p particles at the i_{best} location.

Epoch

It represents the necessary or selected iterations of the algorithm to converge to $G_{best}(i_{best})$.

The Figure 3.4 shows the algorithm PSO flowchart, where the procedure to achieve the optimal solution is described as follows.

1. First a random population is selected according to the lowest and highest value of the active power available for each DGU, thus the velocity and position are also randomly selected.

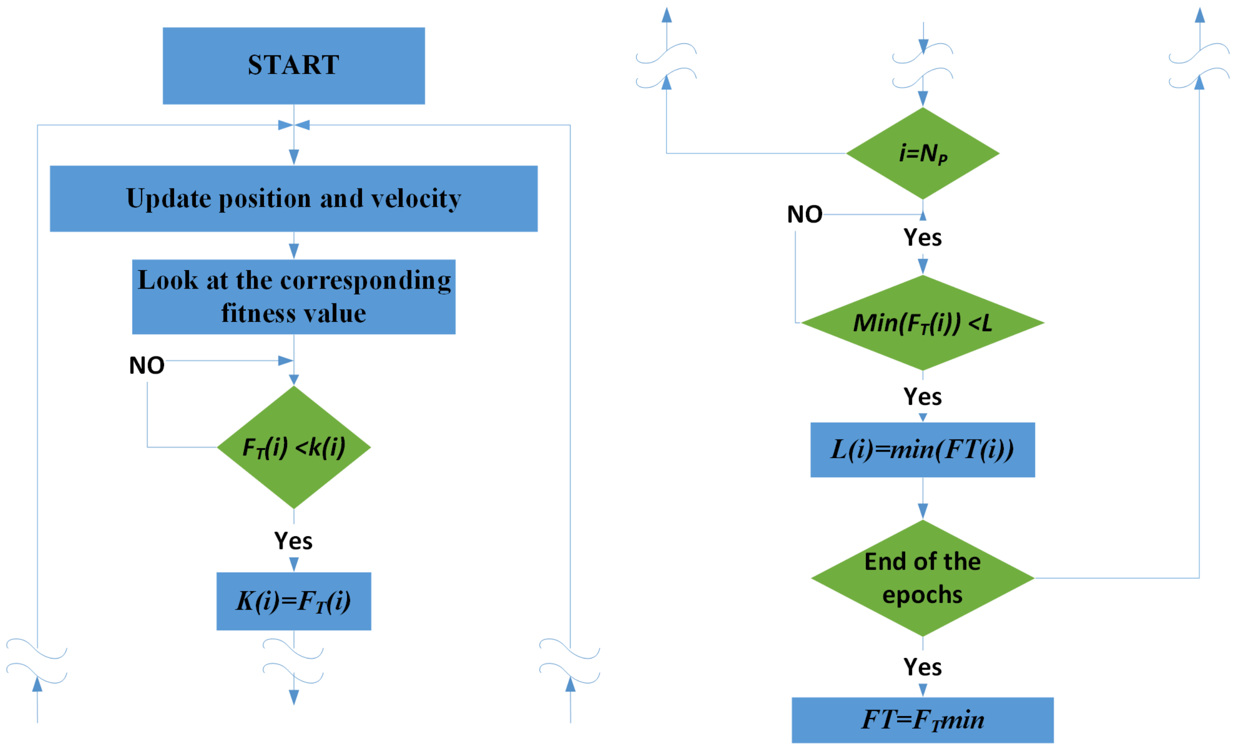

Figure 3.4. PSO algorithm flowchart.

2. Compute the corresponding fitness value F_T to each initial particle, where the constraints are added to the fitness function adding penalty for violating any constraint as it can be seen in equation (3.44) [120, 123]. For this purpose, k represents the DGU.

$$F_T(i) = \sum_{k=1}^{N} F_k(P_k(i)) + \Lambda_1(\sum_{k=1}^{N} P_k(i) - P_L)^2 + \Lambda_2 \sum_{k=1}^{N} (V_{Pk}(i) - V_{Plim})^2, \tag{3.44}$$

where $\Lambda_{1,2}$ are constants adjusted to change the contribution of the penalty terms, P_L is the load connected to satisfy in the MG, V_{Pk} is the corresponding peak nodal voltage of the $k-th$ DGU and V_{Plim} represents the permitted limit for the voltage deviation at the MG nodes.

3. Update the velocity according to the inertia $V_j(i-1)$ (previous velocity), cognitive factors (attraction to the historical best $p_{best(i)}$), social factors (attractions to the global best G_{best}). It is defined by:

$$V_j(i) = V_j(i-1) + c_1 r_1 [P_{best,j} - X_j(i-1)] + c_2 r_2 [G_{best} - X_j(i-1)]; \quad j = 1, 2, ..., N, \tag{3.45}$$

where c_1 and c_2 are the cognitive and social factors, and r_1, r_2 are randomly selected with $r_k \varepsilon\, [0, 1]$.

4. Update the position of the jth particle at the ith iteration. That is:

$$X_j(i) = X_j(i-1) + V_j; \quad j = 1, 2, ..., N. \tag{3.46}$$

5. Compute the fitness value at the new position $f\,(p_j(i))$.

6. Update the historical best having an established value as first reference as the minimum allowable value $K(i)$.

7. Update the global best having an established value as first reference as the minimum allowable value $L(i)$.

8. Finally return the global best of F_T according to the stopping criteria established. The Figure 3.5 shows a graphical description of the influence factors over the current particle that tends to achieve the global best and at the same time it tends to achieve the optimum [124].

Table 3.4 lists the PSO parameters to obtain the optimum point of operation for the MG system by using the cost functions considered before, where N_P and E_P are the number of particles and epochs considered respectively, and P_{max} is the maximum allowable value to each $k-th$ component of the particles, hence $P_{1,2,3}(i) \leq P_{max}$.

It is important to mention that the cognitive and social factor c_1 and c_2 can take a variety of values, although they are suggested to lie between $[0, 2]$, they represent the acceleration coefficients related to the best particles $p_{best(i)}$ influence and global best value G_{best} influence in the velocity updating [121,124,125]. In this case the selected value shown

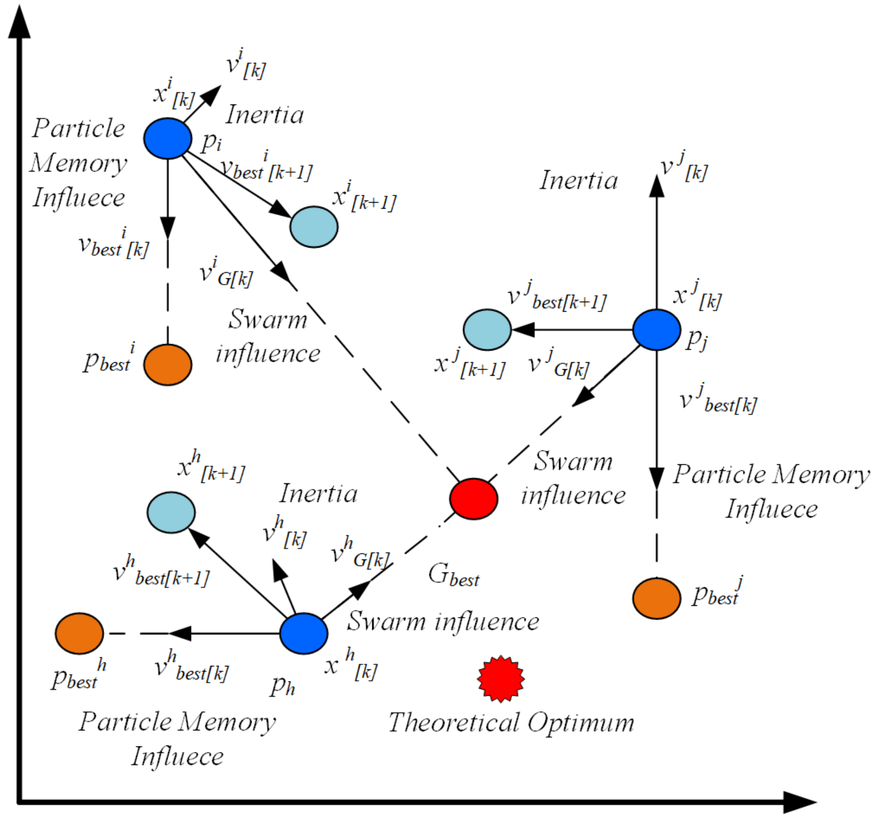

Figure 3.5. Particle Swarm Optimization.

Table 3.4. PSO solution with $P_i = P_{iref}$.

Parameter	**Value**	**Parameter**	**Value**
N_P	500	E_P	500
$c_{1,2}$	0.001	Λ_1	10
$r_{1,2}$	$rand(1)$	Λ_2	0,10*
P_L	850 W	P_{max}	1000 W

Note: *Λ_2 takes the value of 10 when voltage deviations are considered.

in Table 3.4 takes into account that the influence in the velocity is less than 1% of its value for a slow step of the particles updating, because it allows convergence and not to overstep to the last optimum value, avoiding wandering as it approaches the solution; r_1 and r_2 are randomly changing at each step of the algorithm solution.

To assess the capability of PSO to solve the optimization problem, it is considered the DGU as ideal systems $P_k = P^*$ and there is no voltage deviations taking $\Lambda_2 = 0$, where the corresponding MATLAB code is reported in Appendix C.

Figure 3.6 shows the initialization of the random population $N_P = 500$ with their corresponding limits.

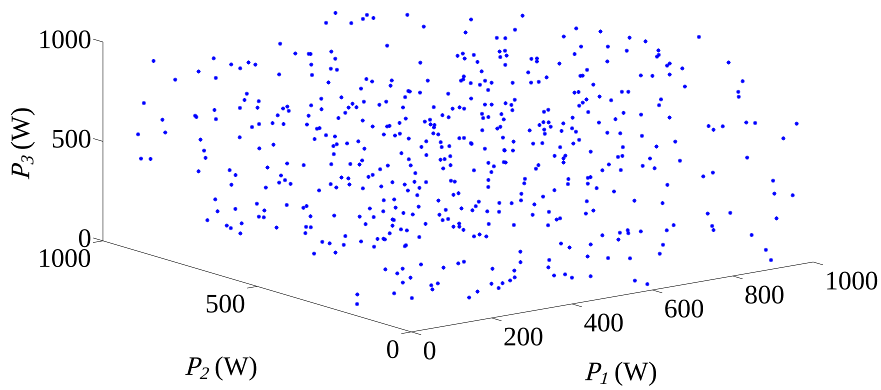

Figure 3.6. Particles population initialization.

Fig. 3.7 shows the particles position at the end of the epochs, where the optimal solution is $P_1 = 396$ W, $P_2 = 326$ W y $P_3 = 126$ W.

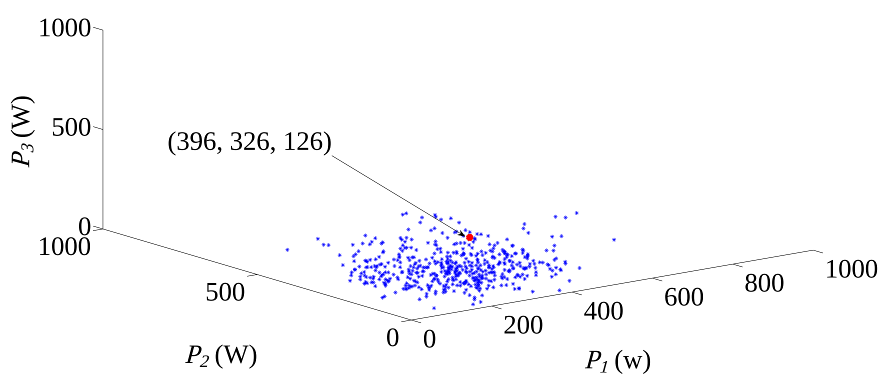

Figure 3.7. Final position of the particles with the global best as optimal point.

Fig. 3.8 shows the evolution of the fitness value through the algorithm iterations, and Table 3.5 lists the error percentages of the fitness value and the achieved value for the load constraint with the penalty factor included in the fitness function, where the reference values to compare the solution were obtained from the gradient method in Section 3.3.

The number of epochs N_P is defined according to the stop criteria, which establishes the parameters to consider for obtaining the optimal solution. In this case the number of

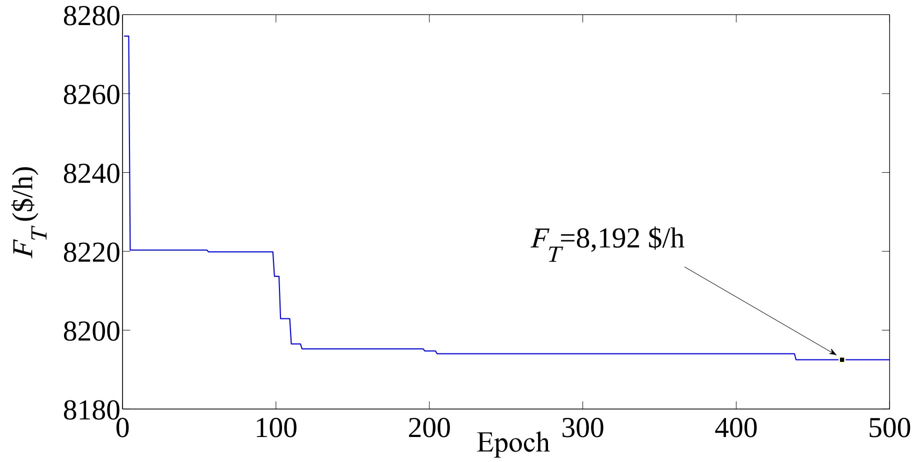

Figure 3.8. Fitness value evolution.

epochs that allows to approach the analytical solution given by the gradient method with suitable accuracy is $N_P = 500$, as shown in Table 3.5.

Table 3.5. PSO solution with $P_i = P_{iref}$.

Parameter	**Value**	**Parameter**	**Value**
N_P	500	E_P	500
err_{FT}	0.0184 %	err_L	0.0038 %
F_T	8,192 $/h	P_L	849.67 W
F_T(theoretical)	8,194 $/h	P_L(theoretical)	850 W

Table 3.6 shows an accuracy assessment for 10 tests of the PSO algorithm for this system, and it contains the percentage error of the fitness function and the load constraint for the DGUs, as well as Figure 3.9 depicts the evolution of the algorithm solution for each test.

Table 3.6. Accuracy assessment of PSO algorithm.

Test	$\%err_{FT}$	$\%err_L$
1	0.0184 %	0.0038 %
2	0.0190%	0.0614 %
3	0.0094%	0.0534 %
4	0.0124%	0.0326 %
5	0.0012%	0.0470 %
6	0.0009%	0.0541 %
7	0.0196%	0.0646 %
8	0.0153%	0.0577 %
9	0.0091%	0.0851 %
10	0.0093%	0.0882 %
Ave.	0.01156%	0.0548%

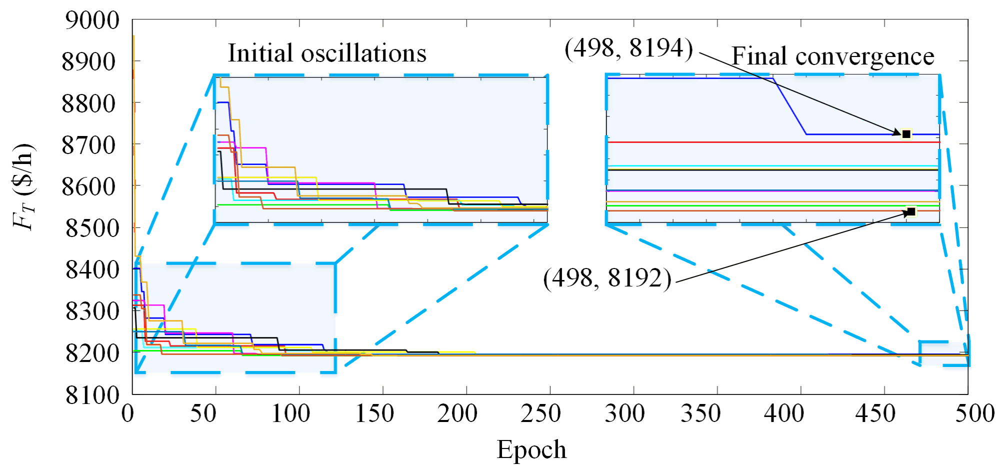

Figure 3.9. Accuracy assessment of PSO algorithm.

3.4.2. Discussion

It can be observed that the percentage error achieved by the PSO algorithm is less than 0.02% for the fitness function and less than 0.06% for the load supplied by the DGUs, which is suitable for including the MG system dynamics in the latter solution, and it also has a suitable handling of the constraints considered for linear and non-linear systems since it does not need information directly from the fitness function but its evaluated value at each location of the particles. There is also a compromise with the selection of the social and cognitive factor, as well as the penalty factor in order to achieve the final value without obtaining oscillating responses when these values are selected too large to make the particles have large movements along the search space, as it can be observed at the beginning of Fig. 3.9, where the randomly selected particles result in different initial state of the algorithm.

As for the implementation of the PSO algorithm in *Matlab*, the resulted execution time without considering the system dynamics is $t_{sim} = 3.059$ s, which is considered suitable for experimental applications owing to the control platform considered for this purpose is a dSPACE DS1103, where its real-time execution performed in preliminary tests results in $t_{ex} = 4.26667$ s.

CHAPTER 4

Simulation results for the microgrid system

These simulation results contemplate the dynamic performance of the entire MG system, mainly the capability of manage different scenarios of the HCS is addressed for supplying the amount of power necessary to satisfy the load connected, and maintain the parameters between suitable values. It is considered the HCS is implemented according to the control levels previously developed. Figure 4.1 shows the HCS applied in a centralized array, where among the advantages of this structure are the stability is not affected directly by the DGU impedance, the power sharing measurements can generate the reference from the calculation of the total load, and also compensates by itself the current error of each inverter in the MG. Among the disadvantages are the necessity of communications together with high bandwidth bus, as well as less system reliability in contrast with the distributed controller, and in some schemes there is no possibility of disabling a part of the system [52, 54, 126].

4.1. Optimal power sharing scenario

Power sharing issue in a MG is related with the effectiveness of control function to maintain regulated operation; for this purpose, in order to assess the dynamic and steady state performance of the HCS, the solution for the Optimal Power Sharing (OPS) problem is applied through co-simulation with the power stage of the MG (grid-feedings and grid-forming converters) implemented in PLECS and the control strategy is computed in Simulink.

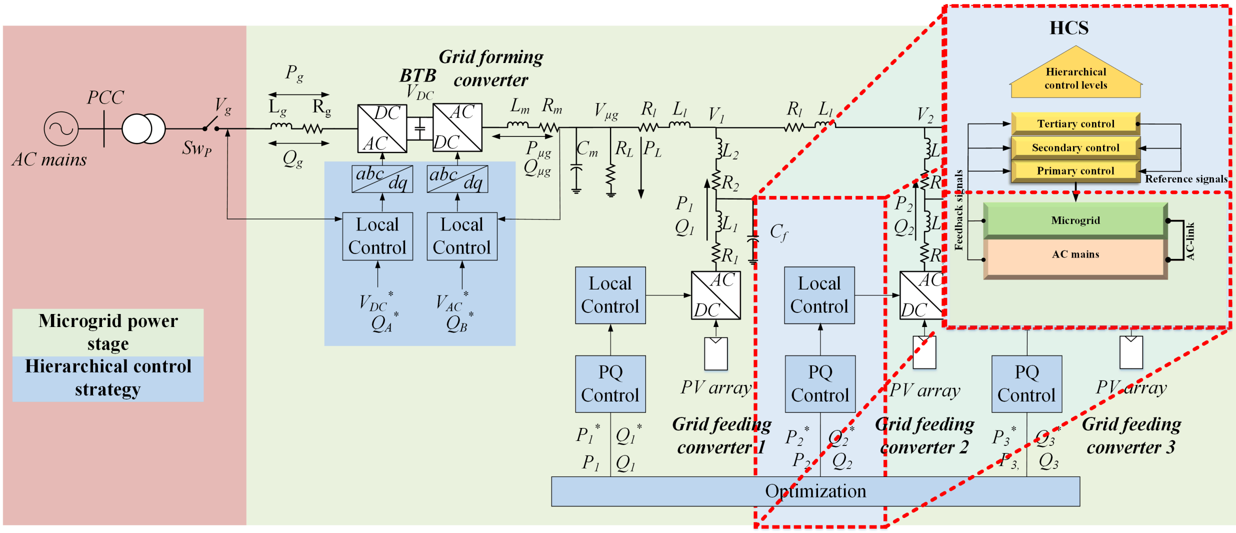

Figure 4.1. AC MG with three PV energy-based DGU in radial array and the HCS.

Figure 4.2 shows a MG system with four DGUs connected; the PQ control and the generation of the current references operate with the passivity based control (PBC) strategy of the Section 2.1.2 in the primary and secondary level, and the optimal solution is calculated in the upper control layer, where the DGUs working as the grid-feedings inject the active power according to their optimal references to supply the load connected $R_L = 10.4\,\Omega$ ($P_L = 1550$ W) and the inductive load $L_L = 171$ mH ($Q_L = 250$ VAr) is supplied according to the different scenarios.

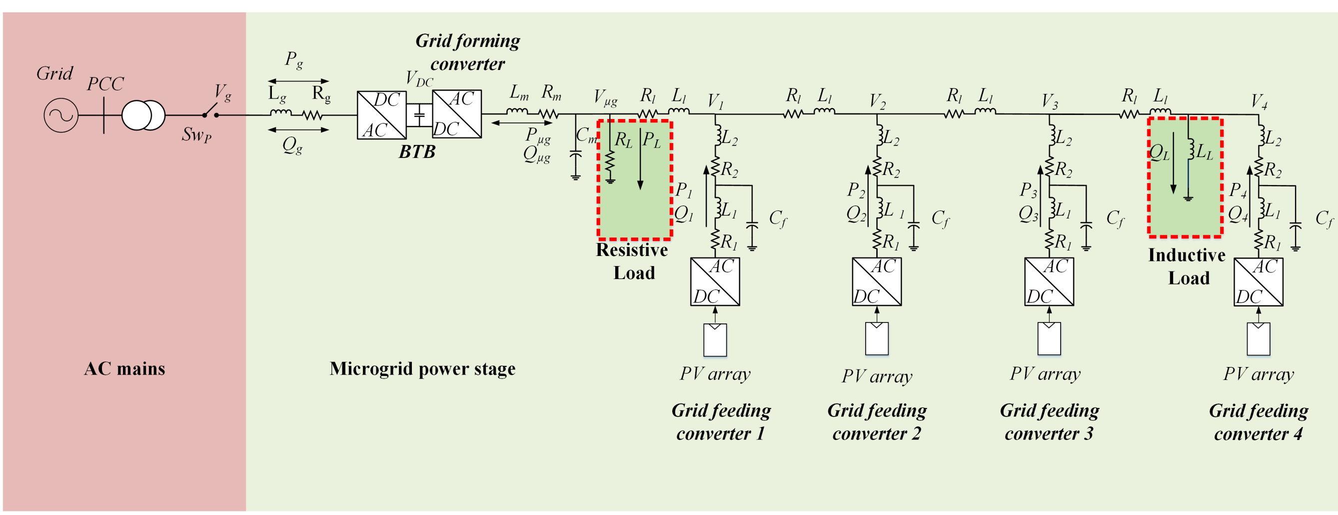

Figure 4.2. AC MG with three PV energy-based DGU with resistive and inductive loads.

4.2. Simulation results for the optimal power sharing scenario

Table 4.1 lists the optimal references of the solution for the optimization problem by considering four grid-feedings in the MG with the cost functions of the equations (4.1)-(4.4) as well as a connected load to satisfy $P_L = 1550\,W$. The purpose is to highlight the issue of nodal voltage deviations in the power lines when the load connected is receiving the active power from the grid-feedings facing different scenarios. In this case the value for the line impedance $\mathbf{Z}_L = 0.001 + j1.88\,m\Omega$ is preliminary selected.

Table 4.1. Optimal solution for a MG with four grid-feedings.

Parameter	**Value**	**Parameter**	**Value**
P_{2Ref}	395.4 W	P_{3Ref}	146.7 W
P_{1Ref}	468.7 W	P_{4Ref}	539.2 W
P_L	1550 W	Q_L	250 VAr

$$F_1(P_1) = 561 + 7.92P_1 + 0.001562P_1^2\,\$/h, \tag{4.1}$$

$$F_2(P_2) = 310 + 7.85P_2 + 0.00194P_2^2\,\$/h, \tag{4.2}$$

$$F_3(P_3) = 78 + 7.97P_3 + 0.00482P_3^2\,\$/h, \tag{4.3}$$

$$F_4(P_4) = 120 + 8.5P_4 + 0.00164P_4^2\,\$/h. \tag{4.4}$$

4.2.1. Microgrid performance with optimal operation and unity power factor

In this scenario it is considered the grid-feedings are delivering the same amount of active power $P_{1,2,3,4} = 387$ W to the load connected, as it can be observed in Figure 4.3 a). At the time $t = 0.55$ s the optimal references for the OPS scenario are sent to the local controllers of each DGU, and to operate at unity power factor at the PCC of each grid-feeding converter the reactive power references are $Q_{1,2,3,4} = 0$ VAr, as it can be observed in Figure 4.3 b).

Figure 4.4 shows the measured values for the peak voltage at the PCC of each DGU, which the voltage deviation among the grid-feedings is due to the line impedance and the

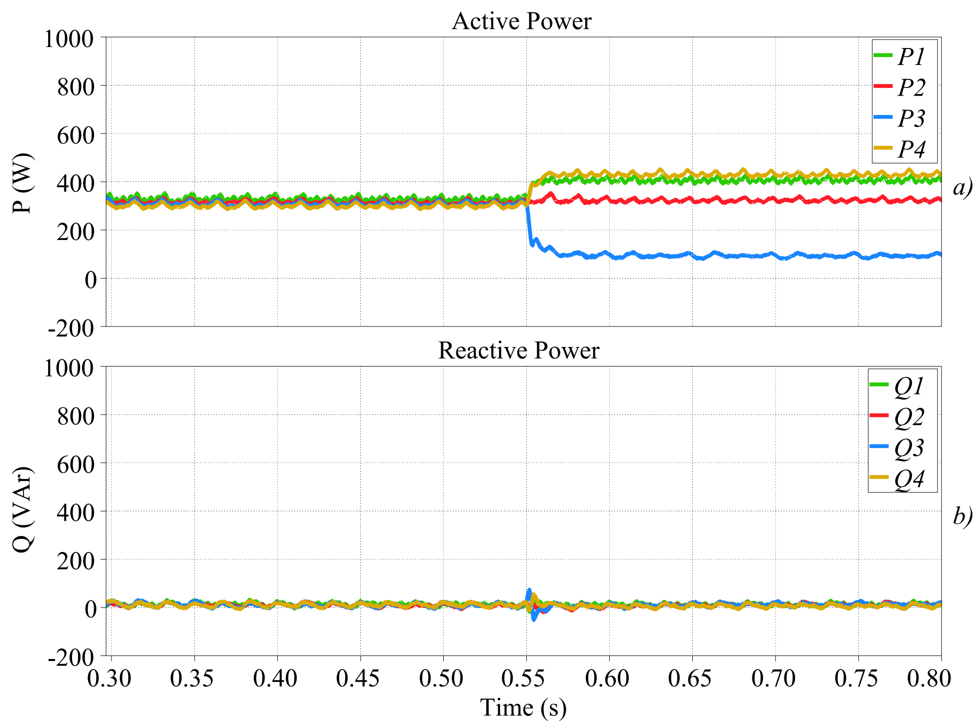

Figure 4.3. Transient response in the active and reactive power applying Optimal Power Sharing method.

corresponding current in this scenario, where the reactive power to satisfy $Q_L = 250$ VAr is supplied directly from AC mains through the grid-forming in the BTB converter.

It is important to mention that the transient response does not present larger overshoot percentage with the change of the power reference

4.2.2. Microgrid performance with optimal operation and reactive power compensation

The voltage deviation previously observed is caused by the line impedance and the circulating current among the DGUs in the MG to satisfy the power demanded by the resistive and inductive load connected. To decrease this deviation, the closest DGU to the inductive load is asked to inject the necessary reactive power to satisfy $Q_L = 250$ VAr and decrease the circulating current in the MG.

Figure 4.5 shows the transient response in the active and reactive power when at the time $t = 0.55$ s the grid-feeding 4 is asked to inject $Q_4^* = 250$ VAr, where it is possible to

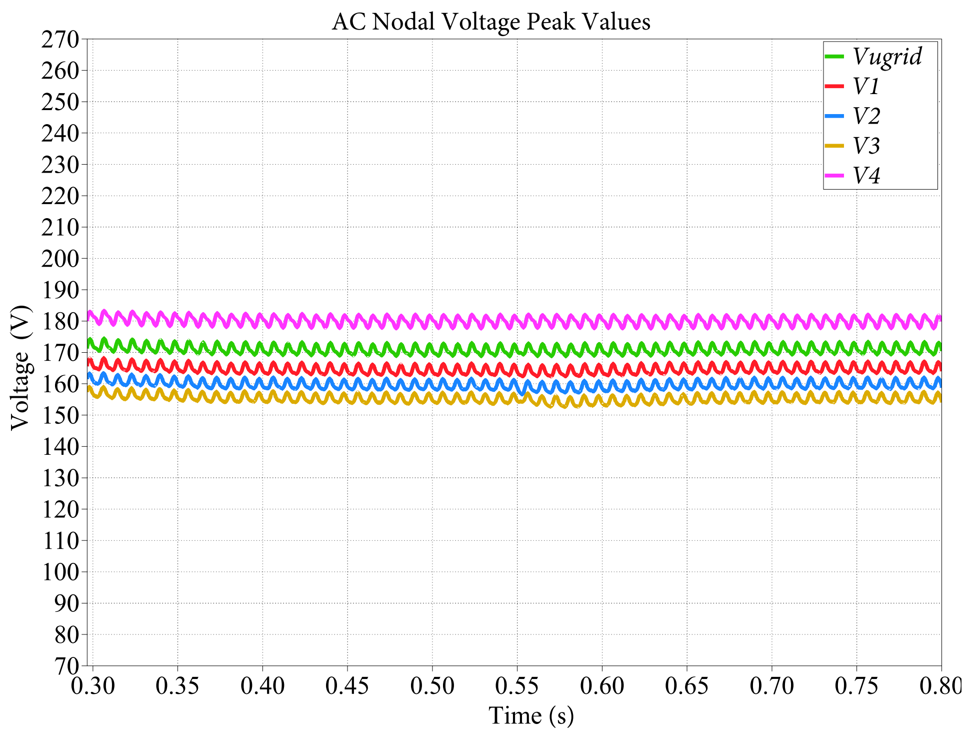

Figure 4.4. Transient response in the AC peak voltage values applying Optimal Power Sharing method.

observe the improvement in the tracking performance to inject the active power by each grid-feeding according to their optimal references owing to the local control depends on the voltage and current references at their PCC in the MG. Figure 4.5 b) shows grid-feeding 4 injecting the reactive power $Q_4 = Q_L$ where the rest of the DGUs are working at unity power factor.

Figure 4.6 shows the improvement in the voltage deviation where the reactive power is compensated by the nearest DGU, where the voltage reference in the MG is $V_{peak} = 180$ V which corresponds to $V_{\mu g} = 127$ V_{rms}.

Table 4.2 lists the nodal voltages where it is possible to observe the voltage deviation of the nodes 1-4 compared with the rated value of $V_{\mu g}$ without reactive power compensation is greater than the voltage deviation when the grid-feeding 4 converter near to the inductive load Q_L is injecting 250 VAr to the MG. Also, in the first case the main grid is supporting this reactive power increasing the losses in the system.

The previous cases demonstrate the capability of the MG system with HCS structure to

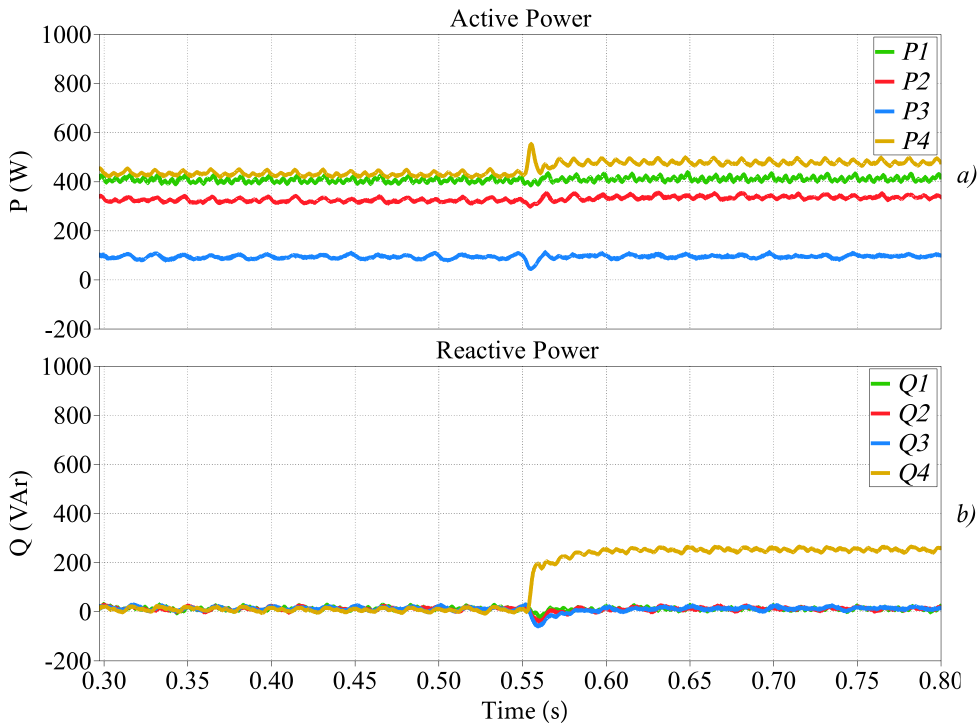

Figure 4.5. Transient response in the active and reactive power with reactive power compensation.

Table 4.2. RMS Nodal voltages values of the MG.

Power sharing without reactive power compensation			**Power sharing with reactive power compensation**		
Parameter	**Value**	**% Error**	**Parameter**	**Value**	**% Error**
$V_{\mu grid}$	127 V	− − −	$V_{\mu grid}$	127 V	− − −
V_1	122.53 V	3.51%	V_1	123.03 V	3.12%
V_2	118.11 V	7%	V_2	122.35 V	3.66%
V_3	114.49 V	7.48%	V_3	122.46 V	3.57%
V_4	111.26 V	12.39%	V_4	122.84 V	3.27%

maintain a suitable performance during its operation while the load connected is satisfied as well as the extended functions of PV inverters improve the capability to maintain the voltage levels near to the rated values.

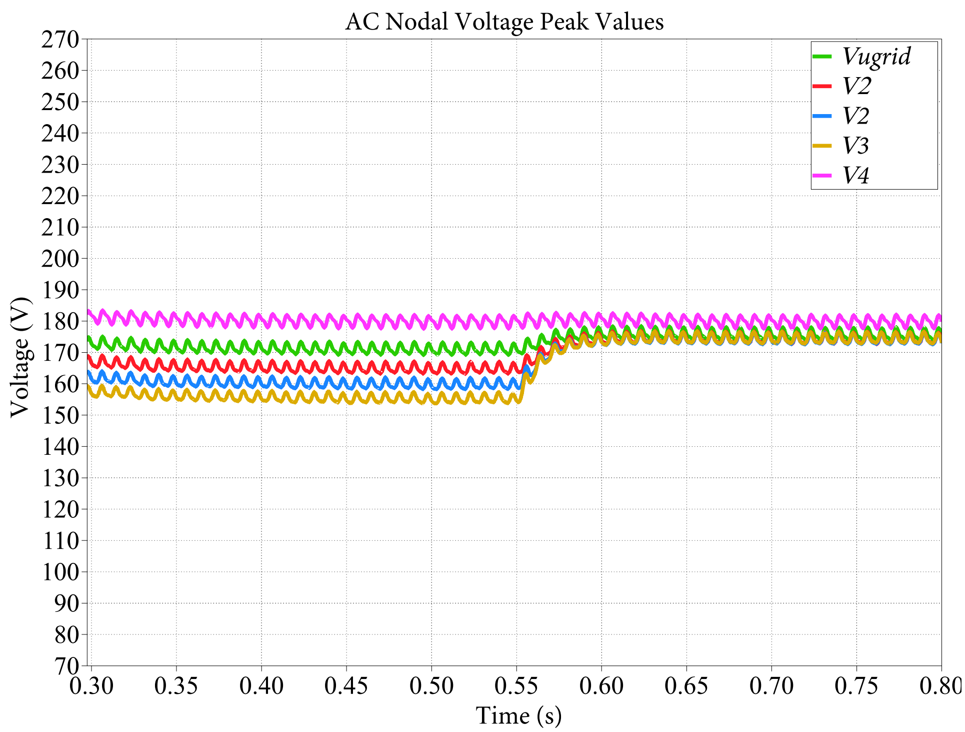

Figure 4.6. Transient response in the AC peak voltage values with reactive power compensation.

4.3. Simulation results for the microgrid dynamical performance and black-start scenario

The dynamical performance of the microgrid is assessed by considering the black-start capability of the MG and the optimal power sharing scenario, where the corresponding voltage deviations are caused by taking into account the line parameters previously designed for a proposed realistic line impedance. The parameters considered are listed in the Table B.1 of the Appendix B.

To avoid the inherent steady state error of the classical PBC strategy developed in Chapter 2, a PI-PBC cascade structure is considered, as it can be seen in Figure 4.7, the current references of the PBC strategy are generated from the output of the PI controller as a secondary control in the HCS structure. The tracking capabilities of the PI allow the improvement of the dynamic performance of the grid-feedings converter, where this structure has been proven in power filter applications [127]. The corresponding proportional and integral gains are $K_{Ppbc} = 0.95$ $K_{Ipbc} = 32.2$.

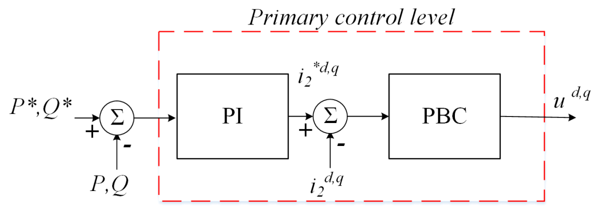

Figure 4.7. PI-PBC strategy.

4.3.1. Optimal power sharing scenario with PSO

The PSO algorithm developed for the MG system in Chapter 3 is included at the third level of the HCS with the system dynamics to compensate the voltage deviations, for this purpose the fitness function considers the penalty factor for the voltage deviation as the equation (4.5)

$$F_T(i) = \sum_{k=1}^{N} F_k(P_k(i)) + \Lambda_1(\sum_{k=1}^{N} P_k(i) - P_L)^2 + \Lambda_2 \sum_{k=1}^{N}(V_{Pk}(i) - V_{Plim})^2, \tag{4.5}$$

where in this case V_{Plim} considers the allowable limit of peak voltage for $\Delta V \leq 5\%$, k corresponds to the $k-th$ DGU, N is the number of DGUs, and i is the corresponding iteration of the PSO algorithm, as stated in Chapter 3. Hence the problem formulation is as bellow:

$$Min \left(\sum_{k=1}^{N} F_k(P_k(i)) + \Lambda_1(\sum_{k=1}^{N} P_k(i) - P_L)^2 + \Lambda_2 \sum_{k=1}^{N}(V_{Pk}(i) - V_{Plim})^2 \right). \tag{4.6}$$

subject to

$$\sum_{k=1}^{N} P_k = P_L = 850\,W, \tag{4.7}$$

$$170 \leq V_{Plim} \leq 190\,V. \tag{4.8}$$

Table 4.3 lists the parameters given for this analysis; it is possible to observe that the error percentages are less than 1%, as well as Figure 4.8 shows the evolution of the fitness function which allows convergence with suitable performance when the dynamics in the system is considered within the algorithm solution and there is penalty for the constraints in the problem.

Table 4.3. PSO solution with the system dynamics.

Parameter	**Value**	**Parameter**	**Value**
N_P	70	E_P	80
err_{FT}	0.98 %	err_L	0.43 %
F_T	8,274 \$/h	P_L	846.31 W
F_T(theoretical)	8,194 \$/h	P_L(theoretical)	850 W

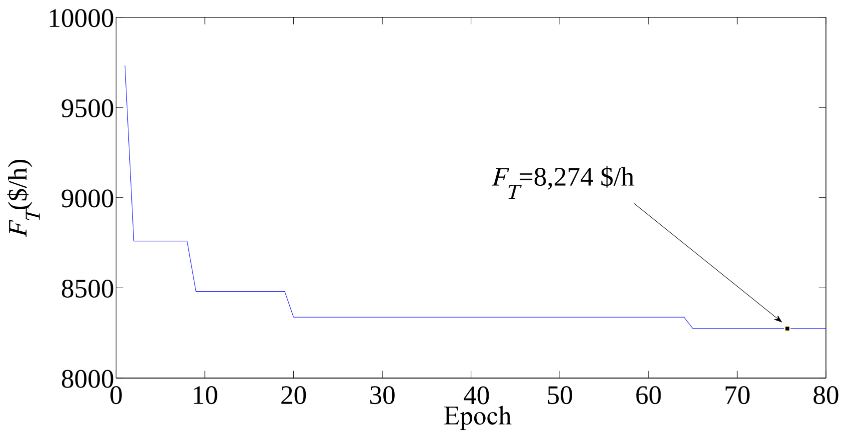

Figure 4.8. Fitness value evolution including the system dynamics.

The system performance is assessed and the DGUs are asked to inject the corresponding active power for the OPS scenario, owing to the steady state error has been improved with the consideration of the PI-PBC cascade structure in the control strategy, and the line impedance affects the performance of the optimization algorithm. Figure 4.9 shows the transient response of the active power regulation when the references change from $P^*_{1,2,3} = 283$ W to the optimal references at the time $t = 1.5$ s, where the added PI controller to the control strategy does not affect with large overshoot percentage, which is negligible.

Figure 4.10 shows the voltage deviation considering the connected load close to the third grid-feeding of the MG, which the largest deviation corresponds to the farthest node of the load v_1, and the Table 4.4 lists both cases, where the worst scenario corresponds to the case where the system regulates the optimal references which is less than 3%. This highlights the compromise of operating in minimum operation cost and maintaining no violated constraints in the solution.

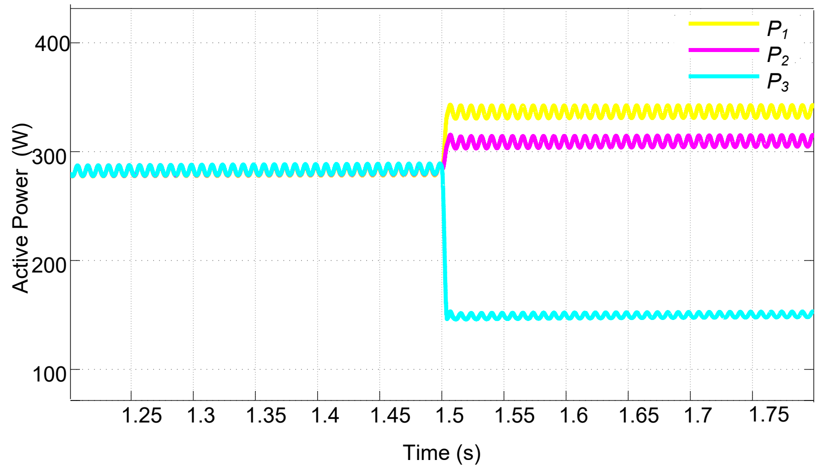

Figure 4.9. Active power transient when the load is connected in the right side of the system.

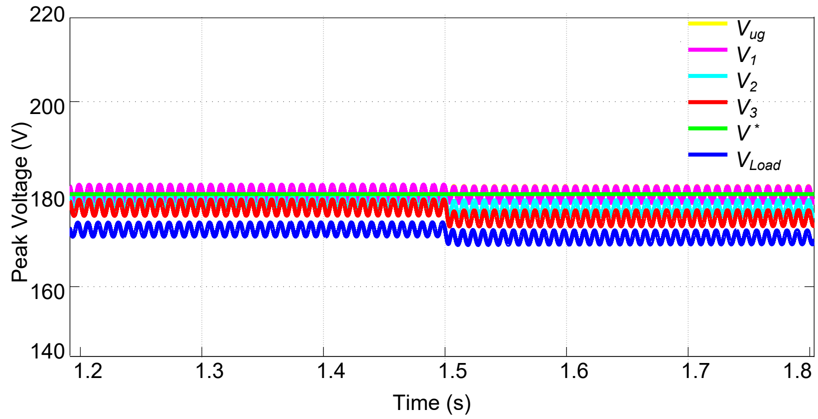

Figure 4.10. Voltage deviations with MG voltage as reference $V_{ug,peak} = 180\,V$.

Table 4.4. Voltage deviations with MG voltage as reference $V_{ug,peak} = 180\,V$.

Parameter	**Value** $(t < 1.5\,s)$	**Value** $(t \geqslant 1.5\,s)$
err_{V1}	0.016%	0.055%
err_{V2}	0.990%	1.700%
err_{V3}	1.590%	2.920%

Once the test in the worst scenario for the voltage deviation has been carried out, three different cases for the location of the load connected are assessed as it is shown in the Figure 4.11, which each case considers only one load connected P_{LA}, P_{LB} or P_{LC}.

After solving the three cases Table 4.5 lists the fitness and load constraint values, and as it can be observed the error percentages for both parameters result in $err < 1\%$.

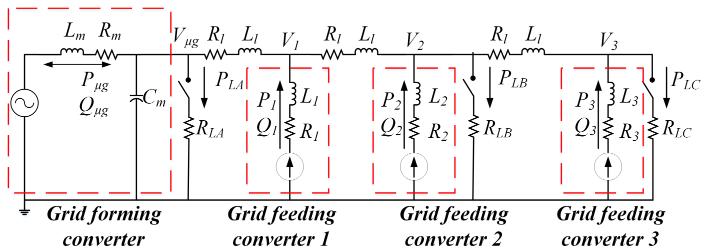

Figure 4.11. MG with three grid-feeding converters and multiple load scenarios.

Table 4.5. PSO solutions for different load positions.

Parameter	Value	Parameter	Value
F_T(theoretical)	8,194 $/h	P_L(theoretical)	850 W
F_{TA}	8,226 $/h	P_{LA}	850.06 W
F_{TB}	8,200 $/h	P_{LB}	848.70 W
F_{TC}	8,211 $/h	P_{LC}	850.11 W

4.3.2. Discussion

Although these scenarios consider a resistive load connected to the MG and the effect of including non-linear loads is not addressed, as first approach it is possible to solve the MG operation facing non-linear loads, by means of compensating the distortion power through the nearest grid-feeding converter to this load as a part of the ancillary services performed by power electronics converters, due to the need of reducing voltage deviations as it is observed in this scenario with different load locations [128, 129]. It is important to mention that in this scenario the reactive power considered to be injected by the grid-feedings is not included in the optimization algorithm, hence one the distortion power is compensated, the solution of the optimal power sharing is not affected.

4.3.3. Microgrid black-start dynamic performance

The black-start (BS) capability of the MG takes part of the additional and ancillary services in the electric power market, which through the black-start units (BSU) supply power after a system blackout, where the time for restoration as well as overshoot percentage during the transient response are critical parameters to avoid system damage [130, 131]. For this purpose BSU have to be previously defined to give support to the MG system, where RES-based DGUs have been proven and analyzed from the point of view of electrical power systems in the system restoration, but the detailed dynamic of this resources is neglected with the BS sequence definition [71, 132].

These simulation results assess the BS capability of PV energy based DGUs in the MG after a fault has been released and the start-up procedure is carried out, where PV systems have been proven as support in large-scale power systems [133]. The proposed black-start sequence considers the proper connection of each converter and DGU to restore the steady state operation of the entire system, through previously making the following assumptions:

- All the associated switches to DGUS and loads shown in Figure 4.12 are open.
- It is assumed the time of the day allows PV panels receive irradiance enough to give the grid-feedings the capability for supplying power to the MG.

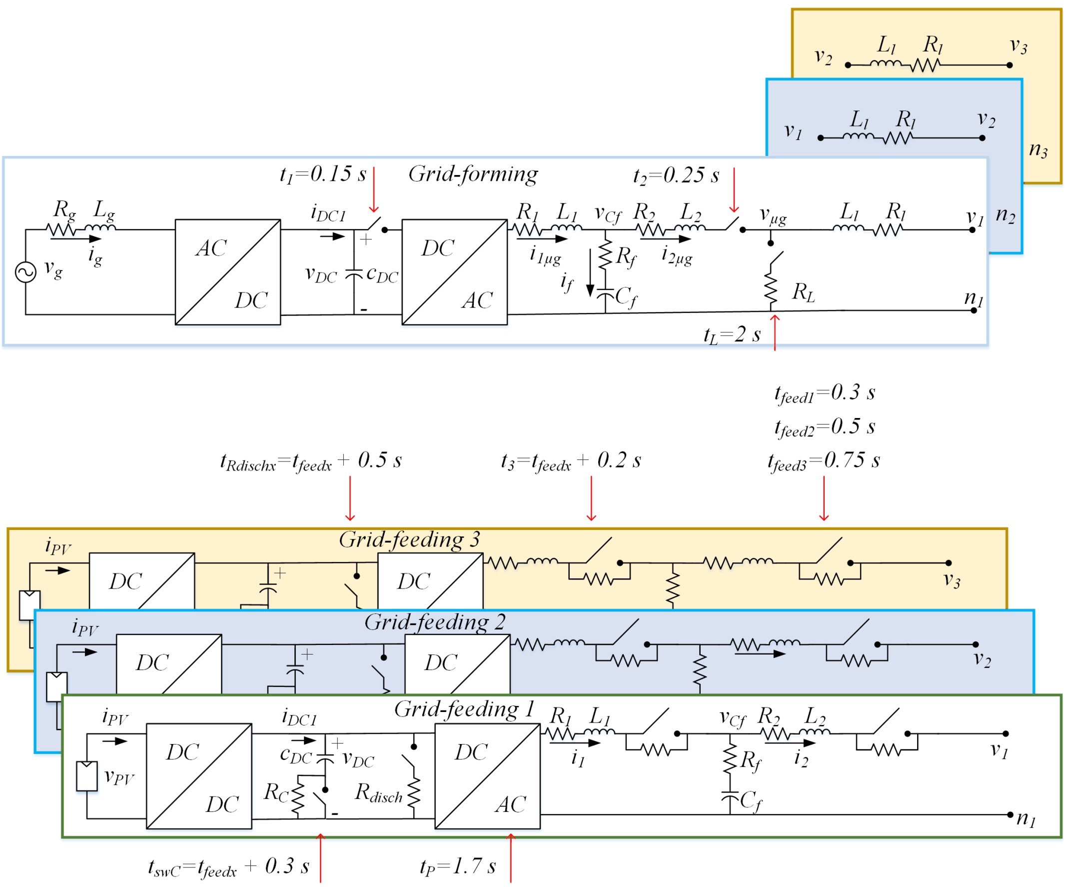

Figure 4.12. Switches location in black-start scenario.

After the above considerations the black-start sequence is as bellow:

1. The control system states are initialized to zero, avoiding large initial errors by empty measurements.

2. As the grid-feedings operate when there is a fixed AC bus voltage at the PCC, first the BTB converter must regulate its v_{DC} bus through VSC_1 to after that allow VSC_2 regulating $v_{\mu g}$.

3. After $v_{\mu g}$ has reached steady state conditions, the main MG switch t_2 and the grid-feeding switches t_{feedx} are closed with the indicated time shown in Figure 4.12 to charge the passive elements of the LCL filters in the MG giving smooth connection for the DGUs.

4. The corresponding switches related with the charge of the capacitors in the PV systems are closed only while the charge is in process in order to limit the inrush current, and after that they are opened, where t_{swC} disable R_C and R_{disch} is opened once the initial energy that circulates from the boost converter to the SPFB converter has been dissipated.

5. Once the inrush current has been dissipated, the power references change from 0 to $P^*_{1,2,3}$ at time t_P, and after that the resistive load R_L is connected to the MG at time t_2.

6. Finally, the PSO algorithm allows the MG system to have a minimum operating cost according to the optimization objectives, hence $P^*_{1,2,3} = P_{opt}$.

According to the above considerations, the following steps describe the BS sequence with specific times and the measured variables and parameters shown in the Figures.

• $0 < t < 0.15$ s: From 0 to 0.15 s v_{DC} in the BTB converter is regulated achieving steady-state conditions, as shown in Fig. 4.13 (a). The control signals in Fig. 4.13 (b),(d) and (e) show that only the DC bus control strategy is working, but the AC MG control and grid-feeding control are still not working.

• $t = 0.15$ s: After v_{DC}, achieves steady state conditions. VSC_2 of the BTB is asked to form $v_{\mu g}$ of the MG at $t_1 = 0.15$ s, this voltage signal tracks a reference measured from the AC mains voltage, therefore it has the same amplitude and frequency. Fig. 4.13 (c) shows the DQ MG voltage achieving steady-state conditions after the time when it is turned on, as well as the suitable performance as it is tracking the DQ signals of voltage.

• $t = 0.25$ s: Once the AC MG bus achieves steady-state conditions, the switch that links the grid-forming with grid-feeding nodes is closed at $t_2 = 0.25$ s. The switches connected

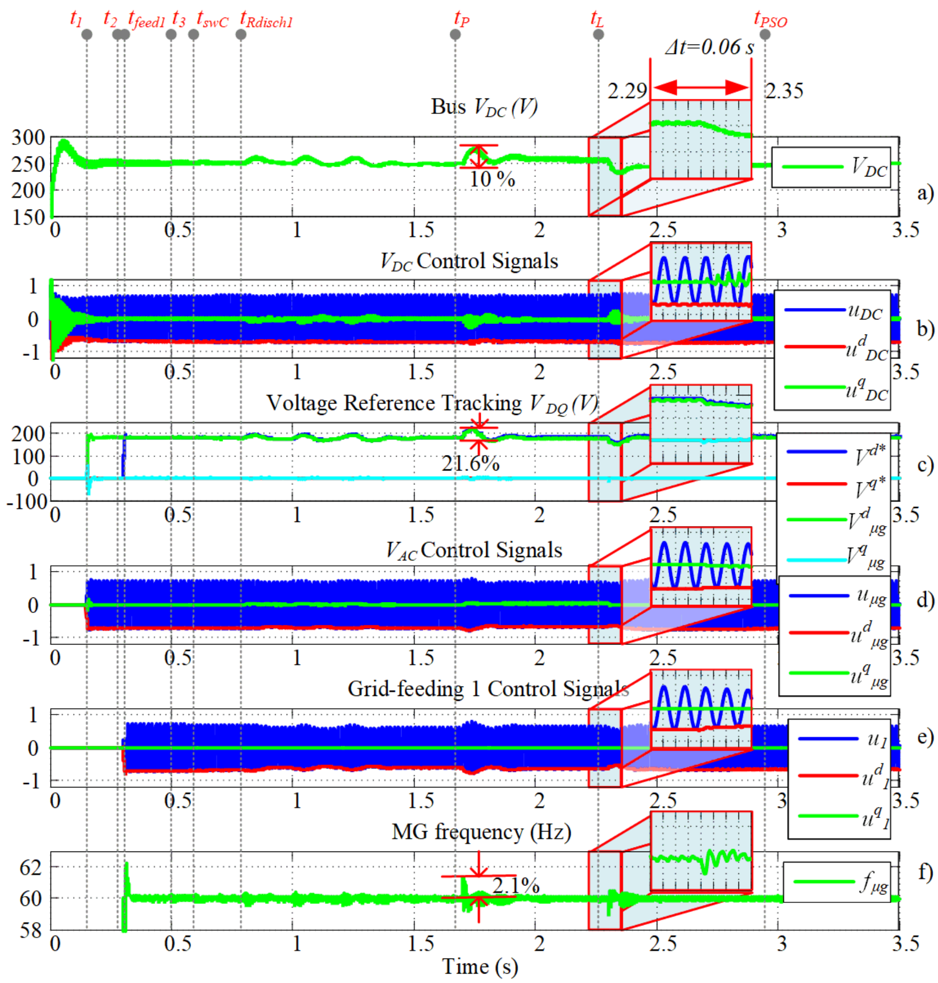

Figure 4.13. Control signals in black-start sequence.

in the LCL filter of each grid-feeding have a resistor in parallel operation to allow charging of the capacitor without large overshoots caused by the inrush current. Fig. 4.14 shows the active power measurements for the active power of the grid-feedings and their references $P^*_{1,2,3}$ as correspond and $v_{\mu g}$ is the MG voltage measured.

• $t = 0.3$ s: After the switch in t_2 is closed, the switches of the grid-feedings are closed t_{feedx} with $x\varepsilon\{1, 2, 3\}$, starting with the first converter with $t_{feed1} = 0.3$ s, where only the switch in series connection with L_2 is closed, for later to close the one in series with L_1 at a time 0.2 s later, (i.e. $t_3 = 0.5$ s). Figs. 4.14 shows the active power measurement of each grid-feeding, where it can be observed the active power of the first converter in Fig. 4.14 (a) presents a small overshoot when the second switch is closed in $t_3 = 0.5$ s; after that, a third switch is closed at $t_{swC} = 0.6$ s, it is in the capacitor of boost converter, to put in short circuit its series resistor R_C, where the maximum overshoot is about $P = 320$ W

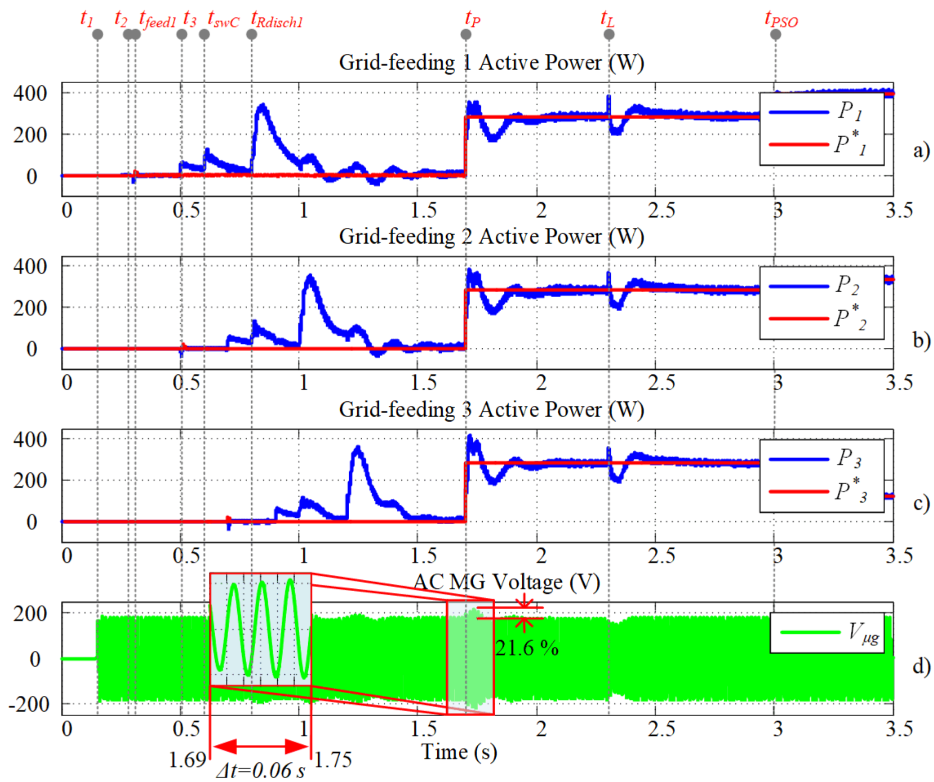

Figure 4.14. Active power and voltage measurements during black-tart sequence.

caused by the discharge of the boost converter capacitor, which can be supported by the system through R_{disch}, it also allows to dissipate the current given by the boost converter to the MG during the grid-feeding interconnection and its switch is open at $t_{Rdisch1} = 0.8$ s.

- $t = 1.7$ s: The three active power references are sent to the control strategy simultaneously at $t_P = 1.7$ s (see Figs. 4.14 and 4.15), and the grid-feedings response can be seen in Fig. 4.14 (a) to Fig. 4.14 (c), where the local control strategy allows the achievement of steady-state conditions at the power reference. The signal $P_{\mu g}$ of Fig. 4.15 shows how the AC mains receives the active power given by the grid-feedings.

- $t = 2.3$ s: The load considered in the optimization problem $P_L = 850$ W is connected to the MG. Fig. 4.15 shows that the system is capable of supplying power to the load without large overshoots to after that, at time $t_{PSO} = 3$ s the active power references are changed to the corresponding value with the PSO algorithm solution. It can be observed that the system is capable of operating in an optimal power-sharing scenario. Fig. 4.14 (d) shows the AC nodal voltage in the MG, where there are no large duration deviations during the transients according to the main MG operation standards.

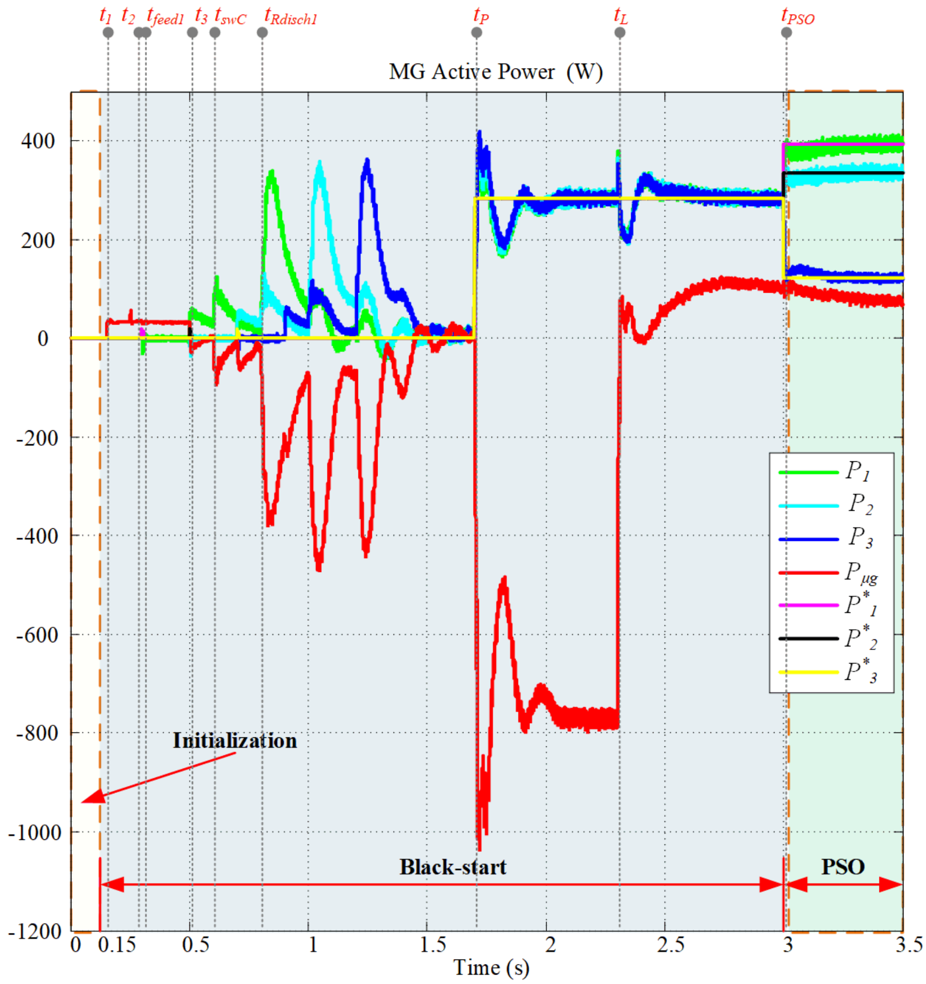

Figure 4.15. Active power measurements during *black-start* sequence.

As it can be seen in Figure 4.15, there is an active power value $P_{\mu g} < 50$ W when the switch in 0.25 s is closed, owing the passive elements of the system. Finally, it is important to mention that the system does not present large frequency deviation, as observed in the frequency measurement given by the PLL structure working in the control strategy, as shown in Fig. 4.13 (f). The largest overshoot is due to the initialization of the PLL variables in the control algorithm which is neglected.

4.3.4. Discussion

From the simulation results obtained, although the solution to the issue of reverse active power to AC mains is not highlighted explicitly, it is addressed when the main operation of the DGUs is limited to supply only the load connected to the MG and avoiding active power exchange with AC mains, as long as it is not a desired operation.

The analysis of the dynamical performance of the MG shows the proposed MG system and the control strategy with HCS achieves steady state conditions and the minimum operation cost, and it is also capable to obtain a suitable performance in voltage and current measurements during black-start scenario under the proposed start-up sequence.

Conclusions

The development of this thesis has contemplated the research work carried out regarding the energy management strategies in AC microgrids with photovoltaic systems as the main energy source. Power electronics converters play an important role in the implementation of the hierarchical control structure to address the main issues related to high penetration levels of this kind of systems into the AC mains, where it is possible to consider the requirements established in the standards, such as voltage and frequency regulation, non-unity power factor operation, and restoration capabilities, to provide the appropriate solution through optimization methods addressing economic operation.

According to the analysis and synthesis of the topics carried out through this document, the following conclusions are obtained:

- The microgrid system working with the proposed hierarchical control structure achieves steady-state conditions with suitable performance in the transient response and the minimum operation cost, where there are not considerable percentage overshoots with $PO_f = 2.1\%$, $PO_{Vdc} = 10\%$ and $PO_{V\mu g} = 21.6\%$, as well as the proper performance observed in the black-start scenario of the start-up procedure.
- High penetration of photovoltaic systems issues can be solved through the suitable selection of the control strategies, as well as the considered microgrid structure, where the main solutions observed in this research work are voltage and frequency regulation with the tracking capability of the considered control strategies, which allows to regulate voltage and frequency deviations when the optimization strategy sends the suitable references to the local control.
- From the simulation results obtained, although the solution to the issue of reverse active power to AC mains is not highlighted explicitly, it is addressed when the main operation of the DGUs is limited to supply only the load connected to the MG

and avoiding active power exchange with AC mains, as long as it is not a desired operation.

- Regarding the requirements considered in the concerned standards of photovoltaic systems operating in microgrids, the single-phase full-bridge inverter has the necessary features to perform the tasks which allow active and reactive power exchange at the point of common coupling, in contrast to the commonly used topologies that are thought to send all the available energy according to the irradiation conditions. Among such requirements are: non-unity power factor operation, voltage and frequency regulation as well as suitable THD_V and THD_I performance, and restoration support.

- The control strategies implemented at the primary level of the hierarchical control structure provided regulation of the necessary parameters accomplishing voltage and frequency regulation in case the converter performs grid-forming tasks or active and reactive power regulation in case the converter performs grid-feeding tasks, hence this control stage results capable to receive the references generated by the next control stage, and achieved the load requirements of the system.

Further conclusions

- Passivity-based controller applied to the grid-feeding structure obtained a suitable performance in the transient response, where mainly the settling time observed in simulation is considerably faster than decoupled current control, and it is observed experimentally the settling time is 25% faster than DCC control.

- The total harmonic distortion of the current at rated load given by each control strategy at the primary level does not have a big difference between them at the tested scenarios, hence the known drawbacks as parameter dependency of decoupled current control could be considered for the selection of the control strategy in contrast with passivity based controller.

- The mathematical model considered to describe the non-linear behavior of the photovoltaic panel is suitable to provide the response of the renewable energy source that supply the grid-feeding topology, where it is possible to observe the transient response features in the current, when it faces the black-start scenario, and in this sense take the necessary actions to reduce such effect to the microgrid through the corresponding switches sequence considered for this purpose.

- The use of the MPPT algorithm is used to obtain the reference of the maximum constraint for the available limit of active power for each photovoltaic array, thus this does not affect the dynamic of the system but the feasible region of the optimal solution.

- The extended functionalities of the grid-feeding converters in the microgrid to accomplish the new requirements of interconnected photovoltaic systems improve the power quality when supplying the load demanded, and compensating voltage and frequency deviation through active and reactive power regulation capabilities, as it can be seen in the optimal operation with reactive power compensation scenario of the Section 4, where the hierarchical control structure demonstrates achieving the MG operation requirements.

- Particle swarm optimization algorithm allows an accurate convergence to the optimal solution, and it handles the considered constraints appropriately to maintain the solution within the feasible region, where the average value of the percentage error given by the tests carried out is $\%err_{FT} = 0.01146\%$ when it approximates the reference value obtained analytically by gradient method, as well as $\%err_{L} = 0.05479\%$ for the load constraint. In contrast, LP method allows suitable accuracy with the drawback of linearizing the cost function lead to high computational burden due to the increase of rows and columns of the main matrix to be solved.

- As for the implementation of the PSO algorithm in *Matlab*, the resulted execution time without considering the system dynamics is $t_{sim} = 3.059$ s, which is considered suitable for experimental applications owing to the control platform considered for this purpose is a dSPACE DS1103, where its real-time execution performed in preliminary tests results in $t_{ex} = 4.26667$ s. Otherwise, including the system dynamics it is not suitable for real-time implementation under these conditions, and would be an area of opportunity in future work to explore this solution.

- The considered cost functions have a basic structure of the economic dispatch problem, where it is important to mention that particle swarm optimization algorithm needs the final value of the fitness functions, hence the generation cost can be established by different criteria and considerations according to the problem to be solved, and other factors can be added to the cost rate functions of each DGU; then the procedure to the optimal solution has been achieved and designed for the MG system, which is not affected directly by modifying such factors.

- The commitment to consider a variety of different constraints through penalty factors as a part of the objective function may be related with the violation of some limits, hence according to the proposed scenario it is possible to supply a part of the demanded load from the AC mains, in order to maintain such parameters within the required limits, pointing out the scenario where the voltage deviation is close to the limits in Section 4.

Contributions

The contributions for this work can be established as follows:

- The average mathematical model in the dq synchronous reference frame for the distributed generation unit considering photovoltaic panels as renewable energy sources as well as the Back-to-Back converter with LCL filter at the microgrid side, to analyze and design their corresponding control strategies, where the PV dynamics is considered unlike the results reported in other works.
- The experimental implementation and comparison of the control strategies in the primary level of the hierarchical control structure for the grid-forming and grid-feeding converters, to contribute with the development of the experimental control platform of the microgrid, where the BTB converter has not been fully explored as grid-forming capabilities in low voltage and small power scale systems.
- A proposed AC microgrid system in radial array to analyze the active and reactive power exchange with the AC mains as well as the effect of supply the load from a purely photovoltaic microgrid, where ESS are considered in other works.
- The proposed centralized energy management system through a hierarchical control structure to solve the optimal operation of the microgrid from the point of view of economical operation by considering the restriction of satisfying only the load connected to the MG, and also solving high penetration issues, instead of having overgeneration and power exchange to the AC mains as others researches have approached.
- The development of the particle swarm optimization algorithm adapted to the microgrid system proposed.

Open issues and future work

The following issues are considered to continue the development of research regarding the addressed topics in this work:

- To design and implement the necessary control structures to provide grid-supporting characteristics to the distributed generation units considered in the microgrid.
- Provide smart features as the capability to decide if the converter works as grid-forming or grid-feeding depending on the conditions at each scenario to obtain a more flexible system and expand the possibilities of issues faced.
- To explore hybrid optimization methods to define binary decision variables into the problem definition to choose which generation units are working at determined scenario of connected load and irradiation conditions.
- To define a multi-objective optimization scenario to establish the priority of the constraints to be accomplished according to different scenarios of available energy and demanded load, such as load, power losses and parameters constraints, as well as power exchange with the AC mains.
- To explore novel optimization methods and their flexibility to adapt the problem and the procedure to obtain the optimal solution.
- A deeper analysis and suitable design of the control strategies at the primary level can contribute with the improvement of the entire dynamical response of the hierarchical control structure, due to the benefits of PBC is not contemplated at the grid-forming local control of this system, being able of decreasing the percentage overshoots and settling time of the transient response when it works as a full controlled PBC MG system.
- Due to the analyzed scenarios in this work only consider resistive load, a variety of studies can be carried out considering different connected loads and locations, such as linear and non-linear loads as well as critical and noncritical loads.
- The cost function can be defined as time variable functions depending on the time horizon in which their change is considered to reflect it in the dynamic performance of the control strategies, where changing the cost or power generation conditions could lead an unexpected change of the power references generated by the optimization

stage, and influencing directly the response of the next control levels, and that is an opportunity area to extend the results obtained in more realistic conditions.

- To carry out the real time implementation of the entire hierarchical control structure is necessary take into account the time frame definition of each control level in order to obtain a suitable performance in its execution according to the changes considered for the renewable energy source available in each scenario, in this case the availability of the irradiation conditions.

Publications

The publications generated from this research work are listed bellow.

1. [134] A. Tobías, V. Cárdenas, F. Quiroz-Vázquez, J. González-Rivera and D. Martínez-Padrón, "Experimental Comparison of Control Strategies in a Single-Phase Grid-Feeding Converter for Microgrid Applications," 2020 17th International Conference on Electrical Engineering, Computing Science and Automatic Control (CCE), Mexico City, Mexico, 2020, pp. 1-6.

2. [135]A. Tobías, V. Cárdenas, J. González-Rivera, M. González-García, F. Quiroz-Vázquez and C. D. Garcia-Beltran, "Optimal Power Sharing Method in Photovoltaic Energy-Based Grid-Feeding Converters for Microgrid Applications," IECON 2021 – 47th Annual Conference of the IEEE Industrial Electronics Society, Toronto, ON, Canada, 2021, pp. 1-6.

3. [136] A. Tobías, V. Cárdenas, C. D. Garcia-Beltran, H. Miranda and R. Álvarez-Salas, "Optimal Power Sharing and Black Start Procedure in Photovoltaic Energy-Based Microgrids," in IEEE Access, vol. 11, pp. 74614-74626, 2023.

4. [137] D.S. Martínez-Padrón, V. Cárdenas, R. Álvarez-Salas, A. Tobias and A. Rivera. ”Comparative Performance Evaluation of PLL Algorithms dSPACE Based for Grid-Connected Single-Phase Converters.” Congreso Nacional de Control Automático 2019, October 23-25, 2019, Puebla, México, Oct 2016.

Appendix A

Line impedance parameters in microgrids

The MG performance is directly affected by the impedance line parameters due to its behavior at different frequency values and harmonics interactions; hence as it is mentioned in the problem formulation, the line parameters are taken into account in order to include its dynamics in the mathematical model, and how it affects the performance of the entire system operation and in this sense avoid instability issues by means of a suitable design of the control strategy [77, 93].

To obtain results closer to real cases, the line impedance considered corresponds to a lumped parameters model of the Eq. (A.1), for a short line with 600 m long sections AWG 6, where resistive and inductive parameters are computed and for a single-phase circuit the conductance is neglected [96, 97]. The Table A.1 contains the corresponding parameters for the conductor of the line.

$$Z_l = R_l + j\omega_\mu L_l. \tag{A.1}$$

To compute R_l and L_l the characteristic impedance Z_c is given by Eq.(A.2); it is a real number if losses are completely neglected [94, 95].

$$Z_C \approx \sqrt{R_{DC}^2 + |Z_{HF}|^2}. \tag{A.2}$$

The high-frequency impedance Z_{HF} is defined by the Eq.(A.3), where γ is the propagation constant and its is part of the imaginary component in Z_{HF}, ρ_c is the conductor conductivity.

$$Z_{HF} = \frac{\gamma}{2\pi r \sigma_c} = 154.722 + j154.722\,\frac{\mu\Omega}{m}, \qquad \text{(A.3)}$$

hence $Z_C = 1.27013 + j0.01884474\ \frac{m\Omega}{m}$.

It is also needed to compute the self inductance per phase defined by Eq.(A.4), taking into account $h = 6\ m$.

$$L_{ii} = \frac{\mu_0}{2\pi} ln \frac{2h_i}{r_i} = 1.5958477\,\frac{\mu H}{m}, \qquad \text{(A.4)}$$

where h_i is the height (m) and r_i the geometric mean radius. Therefore the line impedance Z_l results:

The impedance Z_l is obtained by the following expression.

$$Z_l = Z_C + j\omega_\mu L_{ii} = 1.2701398 + j0.620467919984\,\frac{m\Omega}{m}.$$

Table A.1. Parameters of the conductor.

Parameter	Value	Parameter	Value
Direct current resistance R_{CD}	$1.27x10^{-3}\ \Omega/m$	Permittivity ϵ	$\frac{1x10^{-9}}{36\pi}\ \frac{C^2}{Nm^2}$
Ground conductivity σ_t	$1/100\ S/m$	Permeability μ	$4\pi x10^{-7}\ N/A^2$
Conductor radius r	$4.11x10^{-3}\ m$	Conductor conductivity σ_c	$\frac{1}{R_{CD}\pi r^2}$

The computed values are contained in Table A.2.

Table A.2. MG line impedance parameters.

Parameter	**Value**	**Parameter**	**Value**
AWG	6	l	600 m
R_l	762 $m\Omega$	X_L	372 $m\Omega$
L_l	987 μH	Conductor Area	26818 $cmil$

Appendix

B

MG system definition and parameters

The Figure B.1 depicts the MG system to study and the Hierarchical Control Structure (HCS) proposed in this work

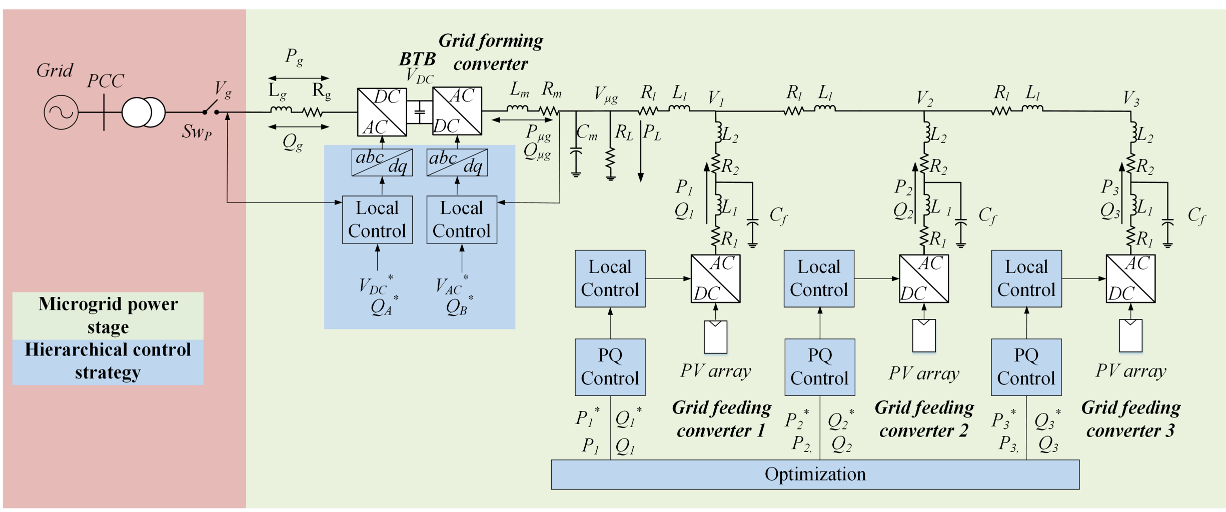

Figure B.1. AC MG with three PV energy-based grid-feeding converters in radial array.

Table B.1 contains the nominal parameters considered in the MG.

Table B.1. Nominal MG System Parameters.

Parameter	**Value**	**Parameter**	**Value**
$\mathrm{V_{DC}}$	250 V	f	60 Hz
$\mathrm{V_{AC}}$	127 V_{rms}	f_{sw}	12.5 kHz
P	700 W	R_1	142 mΩ
Q	$\pm$700 VAr	R_2	1.11 mΩ
C_m	7.55 μF	L_1	3.03 mH
R_m	267 mΩ	L_2	1.11 mH
R_g	142 mΩ	L_g	3.03 mH
C_f	6.88 μF	$\mathbf{Z}_l$	762 +j372 mΩ
L_m	3.38 mH	$V_{\mu g}$	127 V_{rms}
ma	0.7	θ	0 rad

Appendix C

MATLAB code for PSO algorithm

Particle Swarm Optimization without considering dynamics of the MG system

```
%PSO algorithm
    np=500 %Particles
    ep=500%Epochs
    PLD=850;%Load conected (W)
%Social and cognitive factors
       c1=0.001; c2=0.001;
      r1=rand(1); r2=rand(1);
%Population randomly selected
for i=1:np
    P1(i)=1000*rand(1);
    P2(i)=1000*rand(1);
    P3(i)=1000*rand(1);
end

lambda2=10;
%============ Active power constraints ====================
pmax1=1000; pmin1=0;
pmax2=1000;pmin2=0;
pmax3=1000;pmin3=0;

%============ Maximum value of fitness function ============
P1in=pmax1;P2in=pmax2;P3in=pmax3;
Ftin=561+7.92.*P1in+0.001562*P1in^2+...
+310+7.85.*P2in+0.00194*P2in^2+...
+78+7.97.*P3in+0.00482*P3in^2+(P1in+P2in+P3in-PLD)^2*lambda2;
k=2*Ftin*ones(1,np);%local fitness
L=2*Ftin;%global fitness
% ===================First global selection ====================
for i=1:np
    Pref1=P1(i);Pref2=P2(i);Pref3=P3(i);
    P1o(i)=P1(i); P2o(i)=P2(i); P3o(i)=P3(i);

   f1(i)=561+7.92.*P1o(i)+0.001562*P1o(i).^2;
   f2(i)=310+7.85.*P2o(i)+0.00194*P2o(i).^2;
   f3(i)=78+7.97.*P3o(i)+0.00482*P3o(i).^2;
%Economic cost of the system
    FTcosto(i)=f1(i)+f2(i)+f3(i);
%Fitness function with penalty factor for the load constraint
    FT(i)=f1(i)+f2(i)+f3(i)+lambda2*(P1o(i)+P2o(i)+P3o(i)-PLD).^2;

%Selection of the minimum local value for initialization
      if FT(i)<k(i)
          k(i)=FT(i);
          Pp1=P1o(i); Pp2=P2o(i); Pp3=P3o(i);
         P1best(i)=Pp1; P2best(i)=Pp2; P3best(i)=Pp3;
     end
end
```

```
%Selection of the minimum global
    [L,In] =min(FT);
        PL=[P1o(In) P2o(In) P3o(In)];
%============ Velocities Initialization
    ======================
for i=1:np
    vel1(i)=10*rand(1);  vel2(i)=10*rand(1);  vel3(i)=10*rand(1);
end
%Fitness calculation
   for epoc=1:ep %Epochs loop
      for i=1:np%Particles loop
      vel1(i)=vel1(i)+c1*r1*(P1best(i)-P1(i))+c2*r2*(PL(1)-P1(i));
      vel2(i)=vel2(i)+c1*r1*(P2best(i)-P2(i))+c2*r2*(PL(2)-P2(i));
      vel3(i)=vel3(i)+c1*r1*(P3best(i)-P3(i))+c2*r2*(PL(3)-P3(i));
%============== Updating position
    ================================
      P1(i)=P1(i)+vel1(i);
      P2(i)=P2(i)+vel2(i);
      P3(i)=P3(i)+vel3(i);
%============== Active power saturation values and
%              change of direction for the particles===========

       if (P1(i)<=pmin1)
          P1(i)=pmin1;
          vel1(i)=-0.1*vel1(i);
      elseif (P1(i)>=pmax1)
          P1(i)=pmax1;
          vel1(i)=-c1*vel1(i);
        else
          P1(i)=P1(i);
      end
      if (P2(i)<=pmin2);
         P2(i)=pmin2;
         vel2(i)=-0.1*vel2(i);
      elseif (P2(i)>=pmax2)
         P2(i)=pmax2;
            vel2(i)=-c1*vel2(i);
      else
         P2(i)=P2(i);
      end
      if (P3(i)<=pmin3)
         P3(i)=pmin3;
         vel3(i)=-c1*vel3(i);
      elseif (P3(i)>=pmax3)
         P3(i)=pmax3;
         vel3(i)=-c1*vel3(i);
      else
         P3(i)=P3(i);
      end
   Pref1=P1(i);Pref2=P2(i);Pref3=P3(i);
   P1o(i)=P1(i); P2o(i)=P2(i); P3o(i)=P3(i);

   f1(i)=561+7.92.*P1o(i)+0.001562*P1o(i).^2;
   f2(i)=310+7.85.*P2o(i)+0.00194*P2o(i).^2;
   f3(i)=78+7.97.*P3o(i)+0.00482*P3o(i).^2;
   FTcosto(i)=f1(i)+f2(i)+f3(i);
    %Fitness function with penalty factor for the load constraint
   FT(i)=f1(i)+f2(i)+f3(i) +lambda2*(P1o(i)+P2o(i)+P3o(i)-PLD).^2;

%Selection of the minimum local value
    for initialization
      if FT(i)<k(i)
        k(i)=FT(i);
        Pp1=P1o(i);
        Pp2=P2o(i);
        Pp3=P3o(i);
        P1best(i)=Pp1;
        P2best(i)=Pp2;
           P3best(i)=Pp3;
      end
         end
%Minimum global selection
      if min(FT)<L
         [L,In] =min(FT);
         PL=[P1(In) P2(In) P3(In)];
      end
PLe(:,epoc)=PL';
LLe(epoc)=L;
         end
%Ploting the final fitness value for each epoch
PLsuma=sum(PL);
title('fitness');
plot(LLe);
fprintf('%Error');
Cost_Error=vpa((LLe(end)-8194)/8194*100);
Load_Error=vpa(100*(PLsuma-PLD)/PLD);
disp('%');
```

Particle Swarm Optimization considering dynamics of the MG system in the solution

```
open('3_DGU_MG_system.slx');
%PSO algorithm
np=70 %Particles
ep=80%Epochs
PLD=850;%Load conected (W)
%Penalty factors
lambda1=10;%Load constraint
lambda2=10;%Nodal voltage constraint
%Social and cognitive factors
c1=0.001; c2=0.001;
r1=rand(1); r2=rand(1);
%Population randomly selected
for i=1:np
P1(i)=1000*rand(1);
P2(i)=1000*rand(1);
P3(i)=1000*rand(1);
end
%=== Active power constraints =====
pmax1=600; pmin1=150;
pmax2=400;pmin2=100;
pmax3=200;pmin3=50;
%== Maximum value of fitness function
    ====
P1in=pmax1;P2in=pmax2;P3in=pmax3;
Ftin=561+7.92.*P1in+0.001562*P1in^2+...
+310+7.85.*P2in+0.00194*P2in^2+...
+78+7.97.*P3in+0.00482*P3in^2+...
+(P1in+P2in+P3in-PLD)^2*lambda2;
k=2*Ftin*ones(1,np);%local fitness
L=2*Ftin;%global fitness
% =====First global selection ==========
    for i=1:np
        Pref1=P1(i);Pref2=P2(i);Pref3=P3(i
            );
%========MG system simulation===========
        sim('3_DGU_MG_system.slx.slx')

%=====Output power of each DGU====
            t=simout.Time;
            theta=simout.Data;
             P1o(i)=theta(end,1);
              P2o(i)=theta(end,2);
             P3o(i)=theta(end,3);
%====Output voltage of each DGU====
           V1(i)=theta(end,4);
           V2(i)=theta(end,5);
           V3(i)=theta(end,6);
%=== Cost generation functions of DGUs
    =====
        f1(i)=561+7.92.*P1o(i)+0.001562*
            P1o(i).^2;
        f2(i)=310+7.85.*P2o(i)+0.00194*
            P2o(i).^2;
        f3(i)=78+7.97.*P3o(i)+0.00482*
            P3o(i).^2;
%Economic cost of the system
FTcosto(i)=f1(i)+f2(i)+f3(i);
%Fitness function with penalty factor
    for the load constraint
FT(i)=f1(i)+f2(i)+f3(i)+lambda2*(P1o(i)
    +P2o(i)+P3o(i)-PLD).^2;,...
+lambda1*(V1(i)-180).^2+lambda1*(V2(i)
    -180).^2;,...
+lambda1*(V3(i)-180).^2;
%Selection of the minimum local value
%for initialization
if FT(i)<k(i)
k(i)=FT(i);
Pp1=P1o(i);
Pp2=P2o(i);
Pp3=P3o(i);
P1best(i)=Pp1;
P2best(i)=Pp2;
P3best(i)=Pp3;
   end
end
%Selection of the minimum global
[L,In] =min(FT);
PL=[P1o(In) P2o(In) P3o(In)];
%==== Velocities Initialization =====
for i=1:np
vel1(i)=10*rand(1);
vel2(i)=10*rand(1);
vel3(i)=10*rand(1);
end

%Fitness calculation
for epoc=1:ep
for i=1:np
vel1(i)=vel1(i)+c1*r1*(P1best(i)-P1(i))
    +c2*r2*(PL(1)-P1(i));
vel2(i)=vel2(i)+c1*r1*(P2best(i)-P2(i))
    +c2*r2*(PL(2)-P2(i));
vel3(i)=vel3(i)+c1*r1*(P3best(i)-P3(i))
    +c2*r2*(PL(3)-P3(i));
```

```
%Updating position
P1(i)=P1(i)+vel1(i);
P2(i)=P2(i)+vel2(i);
P3(i)=P3(i)+vel3(i);
%============== Active power saturation values and
%               change of direction for the particles==========
 if (P1(i)<=pmin1)
P1(i)=pmin1;
 vel1(i)=-0.1*vel1(i);
 elseif (P1(i)>=pmax1)
P1(i)=pmax1;
 vel1(i)=-c1*vel1(i);
 else
P1(i)=P1(i);
end
 if (P2(i)<=pmin2);
P2(i)=pmin2;
 vel2(i)=-0.1*vel2(i);
 elseif (P2(i)>=pmax2)
P2(i)=pmax2;
 vel2(i)=-c1*vel2(i);
 else
P2(i)=P2(i);
end
 if (P3(i)<=pmin3)
P3(i)=pmin3;
 vel3(i)=-c1*vel3(i);
 elseif (P3(i)>=pmax3)
P3(i)=pmax3;
 vel3(i)=-c1*vel3(i);
 else
P3(i)=P3(i);
end


 Pref1=P1(i);Pref2=P2(i);Pref3=P3(i);
%=======MG system simulation==========
sim('3_DGU_MG_system.slx.slx')
t=simout.Time;
theta=simout.Data;
P1o(i)=theta(end,1);
P2o(i)=theta(end,2);
P3o(i)=theta(end,3);

V1(i)=theta(end,4);
V2(i)=theta(end,5);
V3(i)=theta(end,6);
f1(i)=561+7.92.*P1o(i)+0.001562*P1o(i).^2;
f2(i)=310+7.85.*P2o(i)+0.00194*P2o(i).^2;
f3(i)=78+7.97.*P3o(i)+0.00482*P3o(i).^2;
FTcosto(i)=f1(i)+f2(i)+f3(i);
FT(i)=f1(i)+f2(i)+f3(i) +lambda2*(P1o(i)+P2o(i)+P3o(i)-PLD).^2;,...
+lambda1*(V1(i)-180).^2+lambda1*(V2(i)-180).^2;,...
+lambda1*(V3(i)-180).^2;


 if FT(i)<k(i)
k(i)=FT(i);
Pp1=P1o(i);
Pp2=P2o(i);
Pp3=P3o(i);
 P1best(i)=Pp1;
 P2best(i)=Pp2;
 P3best(i)=Pp3;

end

end
%Minimum global selection

 if min(FT)<L
[L,In] =min(FT);
PL=[P1(In) P2(In) P3(In)];
end
PLe(:,epoc)=PL';
LLe(epoc)=L;

end
PLsuma=sum(PL);
 figure(3);
 title('fitness');
 plot(LLe);
 fprintf('%Error')
 Error_costo=vpa((LLe(end)-8194)/8194*100)
 Error_carga_watts=vpa(100*(PLsuma-PLD)/PLD)
 disp('%')
```

References

[1] EPA United States Environmental Protection Agency. Sources of greenhouse gas emissions. *https://www.epa.gov/ghgemissions/sources-greenhouse-gas-emissions#electricity*, 2023.

[2] International Energy Agency (IEA). Trends in pv applications 2021. *https://iea-pvps.org/trends_reports/trends-in-pv-applications-2021/#:~:text=Highlights%20include%3A,to%20legal%20and%20regulatory%20constraints.*, 2023.

[3] International Renewable Energy Agency (IRENA). Renewable energy statistics 2022. *https://www.irena.org/Publications/2022/Jul/Renewable-Energy-Statistics-2022.*

[4] Martin Braun, Thomas Stetz, Roland Bründlinger, Christoph Mayr, Kazuhiko Ogimoto, Hiroyuki Hatta, Hiromu Kobayashi, Ben Kroposki, Barry Mather, Michael Coddington, Kevin Lynn, Giorgio Graditi, Achim Woyte, and Iain MacGill. Is the distribution grid ready to accept large-scale photovoltaic deployment?: State of the art, progress, and future prospects. *Progress in Photovoltaics: Research and Applications, Wiley*, 20(6):681–697, 2012.

[5] International Energy Agency (IEA). Photovoltaic power system program annual report 2022. *https://iea-pvps.org/wp-content/uploads/2023/04/PVPS_Annual_Report_2022_v7-1.pdf*, 2023.

[6] International Renewable Energy Agency (IRENA). Remap 2030, renewable energy prospects mexico. *https://www.irena.org/-/media/Files/IRENA/Agency/Publication/2015/IRENA_REmap_Mexico_report_2015.pdf.*

[7] IEEE standard for interconnection and interoperability of distributed energy resources with associated electric power systems interfaces. *IEEE Std 1547-2018 (Revision of IEEE Std 1547-2003)*, pages 1–138, April 2018.

[8] IEEE recommended practice for utility interface of photovoltaic (pv) systems. *IEEE Std 929-2000*, 2000.

[9] IEEE standard for harmonic control in electric power systems. *IEEE Std 519-2022 (Revision of IEEE Std 519-2014)*, pages 1–31, 2022.

[10] Edition 3 Standard 1741. Inverters, converters, controllers and interconnection system equipment for use with distributed energy resources. *https://www.shopulstandards.com/ProductDetail.aspx?productId=UL1741*, 2021.

[11] Smart Inverter Working Group Recommendations. Rule 21, recommendations for updating the technical requirements for inverters in distributed energy resources. *https://www.energy.ca.gov/*, Jan 2014.

[12] Manasseh Obi and Robert Bass. Trends and challenges of grid-connected photovoltaic systems –a review. *Renewable and Sustainable Energy Reviews*, 58:1082 – 1094, 2016.

[13] Jay Jhonson. Roadmap for advanced converter deployment in Mexico. *Sandia National Laboratories*, Sep 2018.

[14] C. Siriwattanasit, A. Sangswang, and S. Naetiladdanon. Performance comparison between heric and z-source single-phase transformerless inverters. In *2017 International Electrical Engineering Congress (IEECON)*, pages 1–4, March 2017.

[15] Anuradha M. Annaswamy and Massoud Amin. Ieee vision for smart grid controls: 2030 and beyond. *IEEE Vision for Smart Grid Controls: 2030 and Beyond*, pages 1–168, 2013.

[16] Shahab Bahrami and Ali Mohammadi. Smart microgrids: From design to laboratory-scale implementation. *Springer Nature Switzerland AG 2019*, pages IX,141, Jan 2019.

[17] Mohammad Farhadi-Kangarlu and Farid Mohammadi. Performance comparison of single-phase transformerless grid-connected pv inverters. In *2018 9th Annual Power Electronics, Drives Systems and Technologies Conference (PEDSTC)*, pages 71–76, 2018.

[18] H. Jedtberg, A. Pigazo, M. Liserre, and G. Buticchi. Analysis of the robustness of transformerless pv inverter topologies to the choice of power devices. *IEEE Transactions on Power Electronics*, 32(7):5248–5257, July 2017.

[19] R. Teodorescu, M. Liserre, and P. Rodriguez. *Grid Converters for Photovoltaic and Wind Power Systems*. Wiley - IEEE. Wiley, 2011.

[20] Mohammad Farhadi Kangarlu, Ebrahim Babaei, and Frede Blaabjerg. An lcl-filtered single-phase multilevel inverter for grid integration of pv systems. *Journal of Operation and Automation in Power Engineering*, 4(1):54–65, 2016.

[21] Office of Energy Efficiency and Renewable Energy. Confronting the duck curve: How to address over-generation of solar energy. *https://www.energy.gov/*, 2019.

[22] R. Torabi, A. Gomes, and F. Morgado-Dias. The duck curve characteristic and storage requirements for greening the island of porto santo. In *2018 Energy and Sustainability for Small Developing Economies (ES2DE)*, pages 1–7, July 2018.

[23] P. P. Zarina, S. Mishra, and P. C. Sekhar. Deriving inertial response from a non-inertial pv system for frequency regulation. In *2012 IEEE International Conference on Power Electronics, Drives and Energy Systems (PEDES)*, pages 1–5, Dec 2012.

[24] A. Safayet, P. Fajri, and I. Husain. Reactive power management for overvoltage prevention at high pv penetration in a low-voltage distribution system. *IEEE Transactions on Industry Applications*, 53(6):5786–5794, Nov 2017.

[25] Y. Wang, P. Zhang, W. Li, W. Xiao, and A. Abdollahi. Online overvoltage prevention control of photovoltaic generators in microgrids. *IEEE Transactions on Smart Grid*, 3(4):2071–2078, Dec 2012.

[26] M. H. J. Bollen, R. Das, S. Djokic, P. Ciufo, J. Meyer, S. K. Ronnberg, and F. Zavodam. Power quality concerns in implementing smart distribution-grid applications. *IEEE Transactions on Smart Grid*, 8(1):391–399, Jan 2017.

[27] Miguel Ramírez, Rafael Castellanos, Guillermo Calderón, and Om Malik. Placement and sizing of battery energy storage for primary frequency control in an isolated section of the mexican power system. *Electric Power Systems Research*, 160:142 – 150, 2018.

[28] J. Johnson, R. Ablinger, R. Bruendlinger, B. Fox, and J. Flicker. Interconnection standard grid-support function evaluations using an automated hardware-in-the-loop testbed. *IEEE Journal of Photovoltaics*, 8(2):565–571, March 2018.

[29] W. A. Omran, M. Kazerani, and M. M. A. Salama. Investigation of methods for reduction of power fluctuations generated from large grid-connected photovoltaic systems. *IEEE Transactions on Energy Conversion*, 26(1):318–327, March 2011.

[30] A. Bedawy, N. Yorino, and K. Mahmoud. Optimal decentralized voltage control in unbalanced distribution networks with high pv penetration. In *2017 Nineteenth International Middle East Power Systems Conference (MEPCON)*, pages 1373–1377, Dec 2017.

[31] Temitayo O. Olowu, Aditya Sundararajan, Masood Moghaddami, and Arif I. Sarwat. Future challenges and mitigation methods for high photovoltaic penetration: A survey. *Energies*, 11(7), 2018.

[32] M. J. Reno, R. J. Broderick, and S. Grijalva. Smart inverter capabilities for mitigating over-voltage on distribution systems with high penetrations of pv. In *2013 IEEE 39th Photovoltaic Specialists Conference (PVSC)*, pages 3153–3158, June 2013.

[33] S. Nowak, M. S. Metcalfe, W. Eberle, and L. Wang. Comparison of voltage control methods in distribution systems using q-v based pi and droop controls of solar inverters. In *2017 IEEE Power Energy Society General Meeting*, pages 1–5, July 2017.

[34] A. Singhal, V. Ajjarapu, J. C. Fuller, and J. Hansen. Real-time local volt/var control under external disturbances with high pv penetration. *IEEE Transactions on Smart Grid*, pages 1–1, 2018.

[35] Nicu Bizon Naser Mahdavi Tabatabaei, Ersan Kabalci. Microgrid architectures, control and protection methods. page 781, 2019.

[36] A. Elmitwally and Mohamed Rashed. Flexible operation strategy for an isolated pv-diesel microgrid without energy storage. *IEEE Transactions on Energy Conversion*, 26(1):235–244, 2011.

[37] M.F. Roslan, M.A. Hannan, Pin Jern Ker, and M.N. Uddin. Microgrid control methods toward achieving sustainable energy management. *Applied Energy*, 240:583 – 607, 2019.

[38] Lubna Mariam, Malabika Basu, and Michael F. Conlon. Microgrid: Architecture, policy and future trends. *Renewable and Sustainable Energy Reviews*, 64:477–489, 2016.

[39] Diress Tilahun Antalem and Avik Bhattacharya. Decentralized control for grid-interactive hybrid dc/ac ring microgrid under input source fluctuations. In

2020 IEEE International Conference on Computing, Power and Communication Technologies (GUCON), pages 383–388, 2020.

[40] Joan Rocabert, Alvaro Luna, Frede Blaabjerg, and Pedro Rodríguez. Control of power converters in ac microgrids. *IEEE Transactions on Power Electronics*, 27(11):4734–4749, 2012.

[41] Asma Alfergani, Khalid Ateea Alfaitori, Ashraf Khalil, and Nagi Buaossa. Control strategies in ac microgrid: A brief review. In *2018 9th International Renewable Energy Congress (IREC)*, pages 1–6, 2018.

[42] Keat Teong Lee, Lubna Mariam, Malabika Basu, and Michael F Conlon. A review of existing microgrid architectures. *Hindawi Publishing Corporation, Journal of Engineering*, pages 2314–4904, 2013.

[43] M. Hua, H. Hu, Y. Xing, and J. M. Guerrero. Multilayer control for inverters in parallel operation without intercommunications. *IEEE Transactions on Power Electronics*, 27(8):3651–3663, Aug 2012.

[44] Yonghao Gui, Baoze Wei, Mingshen Li, Josep M. Guerrero, and Juan C. Vasquez. Passivity-based coordinated control for islanded ac microgrid. *Applied Energy*, 229:551 – 561, 2018.

[45] Bahador Fani, Farshad Zandi, and Alireza Karami-Horestani. An enhanced decentralized reactive power sharing strategy for inverter-based microgrid. *International Journal of Electrical Power and Energy Systems*, 98:531 – 542, 2018.

[46] Y. Han, H. Li, L. Xu, X. Zhao, and J. M. Guerrero. Analysis of washout filter-based power sharing strategy an equivalent secondary controller for islanded microgrid without lbc lines. *IEEE Transactions on Smart Grid*, 9(5):4061–4076, Sep. 2018.

[47] H. Moussa, A. Shahin, J. Martin, B. Nahid-Mobarakeh, S. Pierfederici, and N. Moubayed. Harmonic power sharing with voltage distortion compensation of droop controlled islanded microgrids. *IEEE Transactions on Smart Grid*, 9(5):5335–5347, Sep. 2018.

[48] X. Meng, J. Liu, and Z. Liu. A generalized droop control for grid-supporting inverter based on comparison between traditional droop control and virtual synchronous generator control. *IEEE Transactions on Power Electronics*, 34(6):5416–5438, June 2019.

[49] M. Gao, M. Chen, C. Wang, and Z. Qian. An accurate power-sharing control method based on circulating-current power phasor model in voltage-source inverter parallel-operation system. *IEEE Transactions on Power Electronics*, 33(5):4458–4476, May 2018.

[50] J. He and Y. W. Li. An enhanced microgrid load demand sharing strategy. *IEEE Transactions on Power Electronics*, 27(9):3984–3995, Sep. 2012.

[51] F. Gonzalez-Espin, G. Garcera, I. Patrao, and E. Figueres. An adaptive control system for three-phase photovoltaic inverters working in a polluted and variable frequency electric grid. *IEEE Transactions on Power Electronics*, 27(10):4248–4261, Oct 2012.

[52] J. He, Y. W. Li, J. M. Guerrero, F. Blaabjerg, and J. C. Vasquez. An islanding microgrid power sharing approach using enhanced virtual impedance control scheme. *IEEE Transactions on Power Electronics*, 28(11):5272–5282, Nov 2013.

[53] Q. Shafiee, J. M. Guerrero, and J. C. Vasquez. Distributed secondary control for islanded microgrids-a novel approach. *IEEE Transactions on Power Electronics*, 29(2):1018–1031, Feb 2014.

[54] H. Moussa, A. Shahin, J. Martin, S. Pierfederici, and N. Moubayed. Optimal angle droop for power sharing enhancement with stability improvement in islanded microgrids. *IEEE Transactions on Smart Grid*, 9(5):5014–5026, Sep. 2018.

[55] T. Dragicevic, R. Heydari, and F. Blaabjerg. Super-high bandwidth secondary control of ac microgrids. In *2018 IEEE Applied Power Electronics Conference and Exposition (APEC)*, pages 3036–3042, March 2018.

[56] B. Wei, Y. Gui, S. Trujillo, J. M. Guerrero, and J. C. Vásquez. Distributed average integral secondary control for modular ups systems-based microgrids. *IEEE Transactions on Power Electronics*, 34(7):6922–6936, July 2019.

[57] C. Wang, B. Liang, and J. He. An enhanced power regulation and seamless operation mode transfer control through cooperative dual-interfacing converters. *IEEE Transactions on Smart Grid*, 9(6):5576–5587, Nov 2018.

[58] L. Huang, H. Xin, Z. Wang, L. Zhang, K. Wu, and J. Hu. Transient stability analysis and control design of droop-controlled voltage source converters considering current limitation. *IEEE Transactions on Smart Grid*, 10(1):578–591, Jan 2019.

[59] R. Wai, Q. Zhang, and Y. Wang. A novel voltage stabilization and power sharing control method based on virtual complex impedance for an off-grid microgrid. *IEEE Transactions on Power Electronics*, 34(2):1863–1880, Feb 2019.

[60] M. Castilla, A. Camacho, J. Miret, M. Velasco, and P. Marti. Local secondary control for inverter-based islanded microgrids with accurate active power sharing under high-load conditions. *IEEE Transactions on Industrial Electronics*, 66(4):2529–2539, April 2019.

[61] Alejandro C. Pérez-Flores, Jesús D. Mina Antonio, Víctor Hugo Olivares-Peregrino, Humberto R. Jiménez-Grajales, Abraham Claudio-Sánchez, and Gerardo Vicente Guerrero Ramírez. Microgrid energy management with asynchronous decentralized particle swarm optimization. *IEEE Access*, 9:69588–69600, 2021.

[62] Yuhua Du, Hao Tu, Xiaonan Lu, Jianhui Wang, and Srdjan Lukic. Black-start and service restoration in resilient distribution systems with dynamic microgrids. *IEEE Journal of Emerging and Selected Topics in Power Electronics*, 10(4):3975–3986, 2022.

[63] A. Bidram and A. Davoudi. Hierarchical structure of microgrids control system. *IEEE Transactions on Smart Grid*, 3(4):1963–1976, Dec 2012.

[64] Microgrid dynamics and control. *John Wiley & Sons, Ltd*, 2017.

[65] Ali Mohammadi Shahab Bahrami. Smart microgrids: From design to laboratory-scale implementation. *Springer Cham*, 2019.

[66] J.P.S. (Ed.). (2015) Catalão. Smart and sustainable power systems: Operations, planning, and economics of insular electricity grids (1st ed.). *2015 by Taylor & Francis Group, LLC, CRC Press.*, 2015.

[67] Adriel M. Rizzato Lede, Marcelo G. Molina, Maximiliano Martinez, and Pedro E. Mercado. Microgrid architectures for distributed generation: A brief review. In *2017 IEEE PES Innovative Smart Grid Technologies Conference - Latin America (ISGT Latin America)*, pages 1–6, 2017.

[68] Hyeong-Jun Yoo, Thai-Thanh Nguyen, and Hak-Man Kim. Multi-frequency control in a stand-alone multi-microgrid system using a back-to-back converter. *Energies*, 10(6), 2017.

[69] Mobin Naderi, Yousef Khayat, Qobad Shafiee, Tomislav Dragicevic, Hassan Bevrani, and Frede Blaabjerg. Interconnected autonomous ac microgrids via back-to-back converters—part i: Small-signal modeling. *IEEE Transactions on Power Electronics*, 35(5):4728–4740, 2020.

[70] Ritwik Majumder, Arindam Ghosh, Gerard Ledwich, and Firuz Zare. Power management and power flow control with back-to-back converters in a utility connected microgrid. *IEEE Transactions on Power Systems*, 25(2):821–834, 2010.

[71] Patrícia Poloni, Breno Carneiro Pinheiro, Marcelo Henrique Manzke Brandt, Vanderlei Ferreira, Nádia Carolina Ribeiro, Natali Nunes dos Reis da Silva, Thiago José Lippo de França, Rogério Meneghetti, and Maycon Georgio Vendrame. Comparison between black start and islanding process for the establishment of a rural microgrid with biogas generator. In *2020 IEEE PES Transmission & Distribution Conference and Exhibition - Latin America (T&D LA)*, pages 1–6, 2020.

[72] Janeth Alcalá, Víctor Cárdenas, Alejandro Aganza, Jorge Gudiño-Lau, and Saida Charre. The performance of the btb-vsc for active power balancing, reactive power compensation and current harmonic filtering in the interconnected systems. *Energies*, 13(4), 2020.

[73] Janeth Alcalá, Víctor Cárdenas, Emanuel Rosas, and Ciro Núñez. Control system design for bi-directional power transfer in single-phase back-to-back converter based on the linear operating region. In *2010 Twenty-Fifth Annual IEEE Applied Power Electronics Conference and Exposition (APEC)*, pages 1651–1658, 2010.

[74] Tohid Rahimi, Lei Ding, Mostafa Kheshti, Rasoul Faraji, Josep M. Guerrero, and Gibran David Agundis Tinajero. Inertia response coordination strategy of wind generators and hybrid energy storage and operation cost-based multi-objective optimizing of frequency control parameters. *IEEE Access*, 9:74684–74702, 2021.

[75] Siming Cao, Hanlin Zhang, Kai Cao, Meng Chen, Yi Wu, and Suyang Zhou. Day-ahead economic optimal dispatch of microgrid cluster considering shared energy storage system and p2p transaction. *Frontiers in Energy Research*, 9, 2021.

[76] S. X. Chen, H. B. Gooi, and M. Q. Wang. Sizing of energy storage for microgrids. *IEEE Transactions on Smart Grid*, 3(1):142–151, 2012.

[77] Moudud Ahmed, Lasantha Meegahapola, Arash Vahidnia, and Manoj Datta. Stability and control aspects of microgrid architectures–a comprehensive review. *IEEE Access*, 8:144730–144766, 2020.

[78] Dmitry Baimel, Juri Belikov, Josep M. Guerrero, and Yoash Levron. Dynamic modeling of networks, microgrids, and renewable sources in the dq0 reference frame: A survey. *IEEE Access*, 5:21323–21335, 2017.

[79] Xia Miao and Marija D. Ilić. Modeling and distributed control of microgrids: A negative feedback approach. In *2019 IEEE 58th Conference on Decision and Control (CDC)*, pages 1937–1944, 2019.

[80] Fernando I. Quiroz-Vázquez, V. Cárdenas, J. González-Rivera, Alejandro Aganza-Torres, and Fortino Mendoza-Mondragón. Inversor fotovoltaico monofásico interconectado a la red con soporte de potencia reactiva (*Single-Phase Grid Connected Photovoltaic Inverter with Reactive Power Support*). *Congreso Nacional de Control Automático 2019*, pages 55–60, 2019.

[81] Remus Narcis Beres, Xiongfei Wang, Marco Liserre, Frede Blaabjerg, and Claus Leth Bak. A review of passive power filters for three-phase grid-connected voltage-source converters. *IEEE Journal of Emerging and Selected Topics in Power Electronics*, 4(1):54–69, 2016.

[82] Alper Nabi Akpolat, Yongheng Yang, Frede Blaabjerg, Erkan Dursun, and Ahmet Emin Kuzucuoğlu. Modeling photovoltaic string in plecs under partial shading. In *2019 International Conference on Power Generation Systems and Renewable Energy Technologies (PGSRET)*, pages 1–6, 2019.

[83] Leonardo Callegaro, Mihai Ciobotaru, and Vassilios G. Agelidis. Implementation of 3d lookup tables in plecs for modeling photovoltaic modules. In *2016 Australasian Universities Power Engineering Conference (AUPEC)*, pages 1–6, 2016.

[84] John Schönberger. Modeling a photovoltaic string using plecs®. *Plexim GmbH.*

[85] ERDM Solar. ERDM-SOLAR , ERDM250 P/6 series polycrystalline pv panel datasheet. *https://www.erdm.solar/products*, 2013.

[86] Ioan Viorel Banu, Răzvan Beniugă, and Marcel Istrate. Comparative analysis of the perturb-and-observe and incremental conductance mppt methods. In *2013 8TH INTERNATIONAL SYMPOSIUM ON ADVANCED TOPICS IN ELECTRICAL ENGINEERING (ATEE)*, pages 1–4, 2013.

[87] Deepak Verma, Savita Nema, A.M. Shandilya, and Soubhagya K. Dash. Maximum power point tracking (mppt) techniques: Recapitulation in solar photovoltaic systems. *Renewable and Sustainable Energy Reviews*, 54:1018–1034, 2016.

[88] Antoneta Iuliana Bratcu Seddik Bacha, Iulian Munteanu. Power electronic converters modeling and control. pages XXIII,454, 2013.

[89] Fan Peng, Guohua Zhou, Nengmou Xu, and Siya Gao. Zero leakage current single-phase quasi-single-stage transformerless pv inverter with unipolar spwm. *IEEE Transactions on Power Electronics*, 37(11):13755–13766, 2022.

[90] Thomas A. Lipo D. Grahame Holmes. Pulse width modulation for power converters: Principles and practice. page 744, 2003.

[91] M. Gonzalez, V. Cardenas, and F. Pazos. Dq transformation development for single-phase systems to compensate harmonic distortion and reactive power. In *9th IEEE International Power Electronics Congress, 2004. CIEP 2004*, pages 177–182, 2004.

[92] Muhammad Waqas, Toqeer Ahmed, Rajvikram Madurai Elavarasan, Asad Waqar, Kenneth Leong, Rishi Pugazhendhi, Narottam Das, and Muhammad Waqas Jeelani. Dq transformation based control of single-phase grid-tied inverter. In *2021 31st Australasian Universities Power Engineering Conference (AUPEC)*, pages 1–6, 2021.

[93] Marwa Ben Said-Romdhane, Mohamed Wissem Naouar, Ilhem Slama Belkhodja, and Eric Monmasson. An improved lcl filter design in order to ensure stability without damping and despite large grid impedance variations. *Energies*, 10(3), 2017.

[94] A.R. Bergen and V. Vittal. *Power Systems Analysis*. Prentice Hall, 2000.

[95] Prabha Kundur. *Power System Stability and Control*. McGraw Hill; 1st edition (January 22, 1994), 1994.

[96] Henry Bastidas Mora. Fundamentos teóricos para el cálculo de los parámetros técnicos de las líneas eléctricas aéreas de baja tensión para su uso en telecomunicaciones. *Ingeniería e Investigación*, 29:107 – 111, 08 2009.

[97] J.J. Grainger and W.D. Stevenson. *Power System Analysis*. Electrical engineering series. McGraw-Hill, 1994.

[98] J. M. Guerrero, J. C. Vasquez, J. Matas, L. G. de Vicuna, and M. Castilla. Hierarchical control of droop-controlled ac and dc microgrids—a general approach toward standardization. *IEEE Transactions on Industrial Electronics*, 58(1):158–172, 2011.

[99] Gustavo Pérez-Ladrón, Víctor Cárdenas, Nancy Visairo, and Felipe Pazos. Passivity-based control technique for ups inverters. In *2007 European Control Conference (ECC)*, pages 5734–5739, 2007.

[100] X. Lu, X. Yu, J. Lai, Y. Wang, and J. M. Guerrero. A novel distributed secondary coordination control approach for islanded microgrids. *IEEE Transactions on Smart Grid*, 9(4):2726–2740, July 2018.

[101] Q. Li, C. Peng, M. Wang, M. Chen, J. M. Guerrero, and D. Abbott. Distributed secondary control and management of islanded microgrids via dynamic weights. *IEEE Transactions on Smart Grid*, 10(2):2196–2207, March 2019.

[102] M. Zarif and M. Monfared. Step-by-step design and tuning of voc control loops for grid connected rectifiers. *International Journal of Electrical Power & Energy Systems*, 64:708 – 713, 2015.

[103] Saumitra Barman, Soumya Samanta, Jyoti Prakash Mishra, Prasanta Roy, and Binoy Krishna Roy. Design and implementation of an ida-pbc for a grid connected inverter used in a photovoltaic system. *IFAC-PapersOnLine*, 51(1):680 – 685, 2018. 5th IFAC Conference on Advances in Control and Optimization of Dynamical Systems ACODS 2018.

[104] J. Hu, L. Shang, Y. He, and Z. Q. Zhu. Direct active and reactive power regulation of grid-connected dc/ac converters using sliding mode control approach. *IEEE Transactions on Power Electronics*, 26(1):210–222, 2011.

[105] M A Awal, Hui Yu, Hao Tu, Srdjan M. Lukic, and Iqbal Husain. Hierarchical control for virtual oscillator based grid-connected and islanded microgrids. *IEEE Transactions on Power Electronics*, 35(1):988–1001, 2020.

[106] P. Arboleya, D. Diaz, J.M. Guerrero, P. Garcia, F. Briz, C. Gonzalez-Moran, and J. Gomez Aleixandre. An improved control scheme based in droop characteristic for microgrid converters. *Electric Power Systems Research*, 80(10):1215–1221, 2010.

[107] R. Ortega and E. Garcia-Canseco. Interconnection and damping assignment passivity-based control: towards a constructive procedure - part i. In *2004 43rd IEEE Conference on Decision and Control (CDC) (IEEE Cat. No.04CH37601)*, volume 4, pages 3412–3417 Vol.4, 2004.

[108] Gilbert Bergna-Diaz, Daniele Zonetti, Santiago Sanchez, Romeo Ortega, and Elisabetta Tedeschi. Pi passivity-based control and performance analysis of mmc

multiterminal hvdc systems. *IEEE Journal of Emerging and Selected Topics in Power Electronics*, 7(4):2453–2466, 2019.

[109] Zbigniew Rymarski, Krzysztof Bernacki, Łukasz Dyga, and Pooya Davari. Passivity-based control design methodology for ups systems. *Energies*, 12(22), 2019.

[110] Mario González, Víctor Cárdenas, and Gerardo Espinosa. Advantages of the passivity based control in dynamic voltage restorers for power quality improvement. *Simulation Modelling Practice and Theory*, 47:221–235, 2014.

[111] Singiresu S. Rao. *Engineering Optimization: Theory and Practice Pasta dura – 12 noviembre 2019*. Wiley; Edición 5th ed. (12 noviembre 2019), 2019.

[112] Laura Novoa, Robert Flores, and Jack Brouwer. Optimal renewable generation and battery storage sizing and siting considering local transformer limits. *Applied Energy*, 256:113926, 2019.

[113] Preetha Sreekumar and Omar Al Trad. Optimisation of harmonic droop coefficient to minimize power losses in an islanded microgrid. In *2019 Advances in Science and Engineering Technology International Conferences (ASET)*, pages 1–5, 2019.

[114] H. Zhang, S. Kim, Q. Sun, and J. Zhou. Distributed adaptive virtual impedance control for accurate reactive power sharing based on consensus control in microgrids. *IEEE Transactions on Smart Grid*, 8(4):1749–1761, July 2017.

[115] Noel Augustine, Sindhu Suresh, Prajakta Moghe, and Kashif Sheikh. Economic dispatch for a microgrid considering renewable energy cost functions. In *2012 IEEE PES Innovative Smart Grid Technologies (ISGT)*, pages 1–7, 2012.

[116] Gerald B. Sheblé Allen J. Wood, Bruce F. Wollenberg. Power generation, operation, and control, 3rd edition. *Wiley*, page 656, 2013.

[117] Jianqiang Hu, Michael Z. Q. Chen, Jinde Cao, and Josep M. Guerrero. Coordinated active power dispatch for a microgrid via distributed lambda iteration. *IEEE Journal on Emerging and Selected Topics in Circuits and Systems*, 7(2):250–261, 2017.

[118] Masoud Javadi and Turaj Amraee. Economic dispatch: A mixed-integer linear model for thermal generating units. In *2018 IEEE International Conference on Environment and Electrical Engineering and 2018 IEEE Industrial and Commercial Power Systems Europe (EEEIC / I&CPS Europe)*, pages 1–5, 2018.

[119] MathWorks® Help Center. Reference page for linprog. *https://la.mathworks.com/help/optim/ug/linprog.html?lang=en*.

[120] Singiresu S Rao. Engineering optimization theory and practice. *John Wiley & Sons, Inc., Oct 2019*, 2019.

[121] M.A. El-Shorbagy and Aboul Ella Hassanien. Particle swarm optimization from theory to applications. *Int. J. Rough Sets Data Anal.*, 5(2):1–24, apr 2018.

[122] M.A. Abido. Optimal power flow using particle swarm optimization. *International Journal of Electrical Power & Energy Systems*, 24(7):563–571, 2002.

[123] E. Sortomme and M. A. El-Sharkawi. Optimal power flow for a system of microgrids with controllable loads and battery storage. In *2009 IEEE/PES Power Systems Conference and Exposition*, pages 1–5, 2009.

[124] Xin Zhang, Dexuan Zou, and Xin Shen. A novel simple particle swarm optimization algorithm for global optimization. *Mathematics*, 6(12):287, Nov 2018.

[125] Fernando M. de Oliveira, Sérgio A. Oliveira da Silva, Fábio R. Durand, Leonardo P. Sampaio, Vinícius D. Bacon, and Leonardo B.G. Campanhol. Grid-tied photovoltaic system based on pso mppt technique with active power line conditioning. *IET Power Electronics*, 9(6):1180–1191, 2016.

[126] H. Han, X. Hou, J. Yang, J. Wu, M. Su, and J. M. Guerrero. Review of power sharing control strategies for islanding operation of ac microgrids. *IEEE Transactions on Smart Grid*, 7(1):200–215, Jan 2016.

[127] R. Teran, J. Perez, and J. Beristain. Pi-pbc cascade control tuning for active power filter application. *IEEE Latin America Transactions*, 18(04):781–790, 2020.

[128] Lucas Santana Xavier, Allan Fagner Cupertino, Heverton Augusto Pereira, and Victor Flores Mendes. Partial harmonic current compensation for multifunctional photovoltaic inverters. *IEEE Transactions on Power Electronics*, 34(12):11868–11879, 2019.

[129] Heverton A. Pereira, Guilherme L.E. da Mata, Lucas S. Xavier, and Allan F. Cupertino. Flexible harmonic current compensation strategy applied in single and three-phase photovoltaic inverters. *International Journal of Electrical Power & Energy Systems*, 104:358–369, 2019.

[130] B. Kavya Santhoshi, K. Mohana Sundaram, Sanjeevikumar Padmanaban, Jens Bo Holm-Nielsen, and Prabhakaran K. K. Critical review of pv grid-tied inverters. *Energies*, 12(10):1921, May 2019.

[131] Daniela Pagnani, Frede Blaabjerg, Claus Leth Bak, Filipe Miguel Faria da Silva, Łukasz H. Kocewiak, and Jesper Hjerrild. Offshore wind farm black start service integration: Review and outlook of ongoing research. *Energies*, 13(23):6286, Nov 2020.

[132] Yuxuan Zhao, Zhenzhi Lin, Yi Ding, Yilu Liu, Lei Sun, and Yong Yan. A model predictive control based generator start-up optimization strategy for restoration with microgrids as black-start resources. *IEEE Transactions on Power Systems*, 33(6):7189–7203, 2018.

[133] Darlei Feldmann and Ricardo Vasques de Oliveira. Operational and control approach for pv power plants to provide inertial response and primary frequency control support to power system black-start. *International Journal of Electrical Power & Energy Systems*, 127:106645, 2021.

[134] Agustín Tobías, Víctor Cárdenas, Fernando Quiroz-Vázquez, Juan González-Rivera, and Daniel Martínez-Padrón. Experimental comparison of control strategies in a single-phase grid-feeding converter for microgrid applications. In *2020 17th International Conference on Electrical Engineering, Computing Science and Automatic Control (CCE)*, pages 1–6, 2020.

[135] Agustín Tobías, Víctor Cárdenas, Juan González-Rivera, Mario González-García, Fernando Quiroz-Vázquez, and Carlos D. Garcia-Beltran. Optimal power sharing method in photovoltaic energy-based grid-feeding converters for microgrid applications. In *IECON 2021 – 47th Annual Conference of the IEEE Industrial Electronics Society*, pages 1–6, 2021.

[136] Agustín Tobías, Víctor Cárdenas, Carlos D. Garcia-Beltran, Homero Miranda, and Ricardo Álvarez Salas. Optimal power sharing and black start procedure in photovoltaic energy-based microgrids. *IEEE Access*, 11:74614–74626, 2023.

[137] D.S. Martínez-Padrón, V. Cárdenas, R. Álvarez-Salas, A. Tobias, and A. Rivera. Comparative performance evaluation of pll algorithms dspace based for grid-connected single-phase converters. *Congreso Nacional de Control Automático 2019, Puebla, México, Oct 2019*, pages 169–175, 2019.